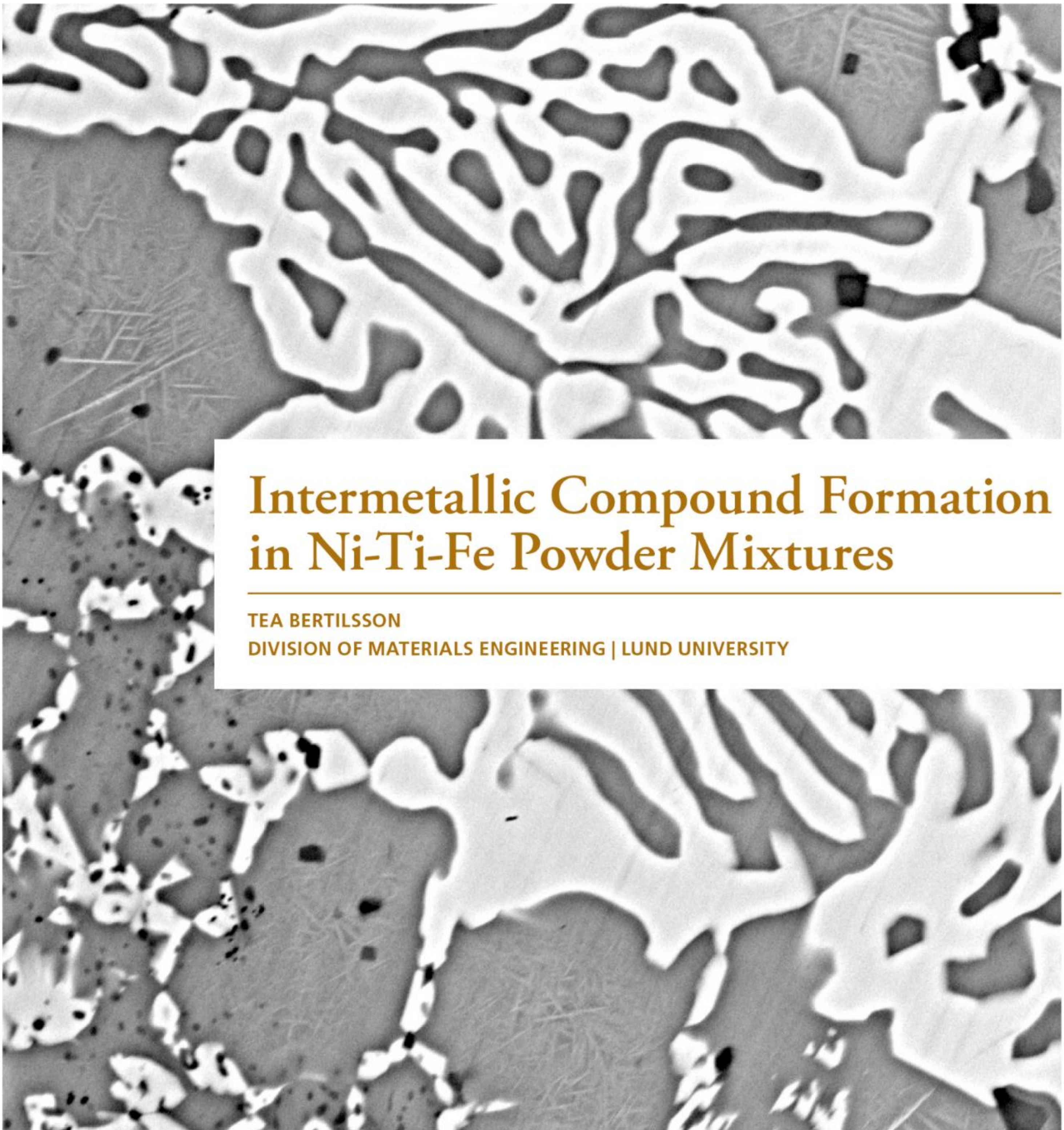

Intermetallic Compound Formation in Ni-Ti-Fe Powder Mixtures

TEA BERTILSSON
DIVISION OF MATERIALS ENGINEERING | LUND UNIVERSITY

MASTER’S THESIS

DIVISION OF MATERIALS ENGINEERING
August 2018

Intermetallic Compound Formation in Ni-Ti-Fe Powder Mixtures

Author: **Tea Bertilsson**

Supervisor: Dr Hossein Sina, LUND UNIVERSITY

Examiner: Prof. Srinivasan Iyengar, LUND UNIVERSITY

Cover: Micrograph of a Ni-Ti-Fe sample containing 10 at.% Fe, heated to 1110 °C.

MSc Thesis

ISRN LUTFD2/TFMT--18/5058--SE

Department of Mechanical Engineering

Lund University

Box 118

SE-221 00 LUND

Sweden

Printed in Sweden by Media-Tryck, Lund University
Lund 2018

Populärvetenskaplig sammanfattning

Bildning av kemiska föreningar i nickel-titan-järn pulver

Tea Bertilsson

Smarta material är enormt användbara. Så länge deras egenskaper kan anpassas för den specifika tillämpningen. Utav nickel och titan kan man tillverka nitinol, en minnesmetall. Dess egenskaper kan justeras genom att man även tillsätter järn. Problemet är att kunskapen om hur järnet påverkar systemet är begränsad.

Då en blandning av olika grundämnen värms upp till tillräckligt höga temperaturer kan olika kemiska föreningar mellan dessa grundämnen bildas. Beroende på både den relativa mängden av varje grundämne, och temperaturen, är olika föreningar mer stabila än andra.

Detta gäller för den pulverblanding bestående av lika delar nickel (Ni) och titan (Ti) som var startpunkten för detta projekt. I denna blandning kan flera föreningar bildas. Vid temperaturer upp till cirka 940 °C bildas $NiTi_2$, NiTi och Ni_3Ti genom diffusion. Vid 946 °C sker en kraftig reaktion mellan det återstående fria titanet och $NiTi_2$ som leder till en bildning av mer NiTi. Vid 1111 °C startar ytterligare en reaktion, den här gången mellan NiTi och Ni_3Ti. Genom att tillsätta järn (Fe) till pulverblandningen kan man påverka de två reaktionerna.

I detta projekt tillsattes upp till 20 % järn till lika delar nickel och titan. Ju högre järnhalten var destå svagare blev den första reaktionen mellan det fria titanet och $NiTi_2$. Dessutom separerades smältningen av $NiTi_2$ från den första reaktionen. Den andra reaktionen växte istället i styrka då järnhalten ökades. Av stort intresse var det samband som framträdde mellan temperaturerna för den första reaktionen och för smältningen av $NiTi_2$. Dessa temperaturer ökade linjärt med järnhalten. Den första reaktionen, som i provet utan järn inträffade vid 946 °C, skedde i provet med 20 % järn vid 999 °C. En ökning med mer än 50 °C!

Det visade sig att järnet inte bildade några separata föreningar med nickel eller titan. Istället kunde järnet ersätta nicklet i $NiTi_2$ och i NiTi. Därför minskade den första reaktionen i styrka eftersom det blev mindre titan över då både järn och nickel kunde bilda föreningar med det. På liknande sätt är det även orsaken till att den andra reaktionen växte i styrka eftersom det då fanns extra nickel över till att bilda mer Ni_3Ti.

För den intresserade finns mer information att tillgå i *Intermetallic Compound Formation in Ni-Ti-Fe Powder Mixtures*.

Popular Science Summary

Formation of compounds in nickel-titanium-iron powders

Tea Bertilsson

Smart materials are hugely useful. If their properties can be adjusted for the specific application. The shape memory metal nitinol can be created out of nickel and titanium. Its properties can be altered by also adding iron. The problem is that the knowledge of how iron affects the system is limited.

When a mixture of different elements are heated to sufficiently high temperatures, different chemical compounds can form. Depending on both the relative amount of each element, and the temperature, different compounds are more stable than others.

This applies to the powder mixtures of equal amount of nickel (Ni) and titanium (Ti) that was the starting point for this project. In this mixture several compounds can form. At temperatures up to about 940 °C $NiTi_2$, NiTi and Ni_3Ti were formed through diffusion. At 946 °C a strong reaction between the remaining titanium and $NiTi_2$ takes place, it leads to the formation of more NiTi. At 1111 °C one more reaction starts, this time between NiTi and Ni_3Ti. By adding iron (Fe) to the powder mixture you can affect the two reactions.

In this project up to 20 % iron was added to equal amounts of nickel and titanium. The higher the iron content, the weaker the first reaction between the free titanium and $NiTi_2$ became. Also, the melting of $NiTi_2$ was separated from the first reaction. The second reaction on the other hand grew in strength as the iron content was increased. Of great interest was the connection that emerged between the temperatures for the first reaction and for the melting of $NiTi_2$. These temperatures increased linearly with the iron content. The first reaction, which in the sample without any iron happened at 946 °C, occurred in the sample with 20 % iron at 999 °C. An increase of over 50 °C!

It was made clear that the iron did not form any compounds with nickel or titanium. Instead the iron could replace the nickel in $NiTi_2$ and in NiTi. Therefore the first reaction decreased in strength since there was less titanium left over when both iron and nickel could form compounds with it. In a similar way it is also the reason as to why the second reaction increased in strength since there was extra nickel left over to form more Ni_3Ti.

For the interested, more information is available in *Intermetallic Compound Formation in Ni-Ti-Fe Powder Mixtures*.

Abstrakt

Ni-Ti systemet har en stor mängd tillämpningar, inom områden så spridda som biomedicin och robotteknik. Detta beror till stor del på den intermetalliska föreningen NiTi, vilken är en minnesmetall. Utöver denna egenskap är den intermetalliska föreningen dessutom biokompatibel, har bra mekaniska egenskaper och god resistans mot korrosion. Studier på NiTi har visat att temperaturerna kopplade till dess egenskaper som minnesmetall är mycket känsliga för den exakta sammansättningen hos den icke stökiometriska NiTi fasen. En metod för att kontrollera denna känslighet är att tillsätta järn till systemet. Det ternära Ni-Ti-Fe systemet har främst undersökts för låga järnhalter, eftersom fokuset har legat på NiTi som minnesmetall och hur dessa egenskaper kan förbättras. Effekten av järn på de andra intermetalliska föreningarna som finns i Ni-Ti systemet och den möjliga bildningen av intermetalliska föreningar som innehåller järn har inte undersökts till någon vidare utsträckning.

I detta projekt har fasutvecklingen i det ternära Ni-Ti-Fe systemet undersökts. Elementära pulverblandningar av nickel, titan och järn förbereddes genom att tillsätta 0-20 at.% Fe till lika delar nickel och titan. Pulverna kompakterades till diskar och sintrades. Differentiell svepkalorimetri användes för att studera sintringsprocessen, prov av alla sammansättningar värmdes till 1200 °C och kyldes sedan tillbaka ner till rumstemperatur. Två sammansättningar, innehållande 6 at.% och 10 at.% Fe, valdes för vidare studier av fasutvecklingen, och proven av dessa två sammansättningar värmdes till flera temperaturer under 1200 °C.

Provens mikrostruktur studerades med svepelektronmikroskopi. Energi dispersionsspektroskopi användes i samband med mikroskopin för att studera fördelningen av nickel, titan och järn i proven. Röntgendiffraktion användes för att identifiera vilka faser som fanns i varje prov.

Järn visades ha en effect på bildningen av intermetalliska föreningar i proven genom att agera som en substituent för nickel i $(Fe,Ni)Ti_2$ och (Fe,Ni)Ti. Därigenom möjliggjordes bildningen av en ökad mängd nickelrika föreningar, då järnhalten ökades. Dessa föreningar var Ni_3Ti och den metastabila Ni_4Ti_3. Starttemperaturerna för två exoterma toppar på DSC kurvorna uppvisade linjärt beroende på järnhalten i proven. Temperaturerna som är associerade med $\beta\text{-Ti} + (Fe,Ni)Ti_2 \rightarrow L$ och $(Fe,Ni)Ti_2 \rightarrow (Fe,Ni)Ti + L$ reaktionerna föreslås bero på förhållandet mellan järn och nickel i $(Fe,Ni)Ti_2$.

Nyckelord: Fasutveckling, Ni-Ti-Fe systemet, intermetaller, pulvermetallurgi, reaktiv sintring, DSC, SEM, EDS, XRD.

Abstract

The Ni-Ti system has a broad range of applications, in areas as diverse as biomedicine and robotics. This is in large due to the NiTi intermetallic compound, which exhibits the shape memory effect. In addition to this property, the intermetallic compound is also biocompatible, has good mechanical properties and good corrosion resistance. Studies on NiTi has shown that the temperatures at which the shape memory effect occurs are highly sensitive to the exact composition of the non-stoichiometric NiTi. One method of controlling this sensitivity is to add iron as a third element to the system. The ternary Ni-Ti-Fe system has mainly been investigated for low iron contents, as the focus has been on the NiTi shape memory effect, and how to improve it. The effect of iron on the other intermetallic compounds present in the Ni-Ti system and the possible formation of intermetallic compounds containing iron has not been widely investigated.

In this project the phase evolution in the ternary Ni-Ti-Fe system has been investigated. Elemental powder mixtures of nickel, titanium and iron were prepared by adding 0-20 at.% Fe to equiatomic Ni-Ti. The powders were compacted into discs and sintered. Differential scanning calorimetry was used to study the sintering process, samples of all compositions were heated to 1200 °C and then cooled back down to room temperature. Two compositions, containing 6 at.% and 10 at.% Fe, were chosen for further study of the phase evolution, and samples of these two compositions were heated to several temperatures below 1200 °C.

The microstructure of the samples were studied using scanning electron microscopy. Energy-dispersive spectroscopy was used in conjunction with the microscopy to study the distribution of the nickel, titanium and iron in the samples. X-ray diffraction was used to identify the phases present in each sample.

Iron was shown to affect the intermetallic compound formation in the samples by acting as a substitute for nickel in $(Fe,Ni)Ti_2$ and (Fe,Ni)Ti. Therefore, allowing for an increased amount of Ni-rich compounds to form in the samples with higher iron content. These compounds were Ni_3Ti and the metastable Ni_4Ti_3. The onset temperatures for two exothermic peaks in the DSC curves showed linear dependence on the iron content in the samples. The temperatures associated with the $\beta\text{-Ti} + (Fe,Ni)Ti_2 \rightarrow L$ and $(Fe,Ni)Ti_2 \rightarrow (Fe,Ni)Ti + L$ reactions are proposed to depend on the ratio of iron to nickel in $(Fe,Ni)Ti_2$.

Keywords: Phase Evolution, Ni-Ti-Fe System, Intermetallics, Powder Metallurgy, Reactive Sintering, DSC, SEM, EDS, XRD.

Acknowledgements

This project was carried out between February and August 2018, at the division of Materials Engineering at LTH, Lund University.

I would like to thank my supervisor Hossein Sina for his enthusiastic involvement in the project. He has always been willing to discuss matters both big and small related to the project. I would also like to thank my examiner Srinivasan Iyengar who helped develop my interest in materials technology with his inspiring lectures and discussions on the subject. I am also very grateful to Victor Almblad who conducted experiments alongside me, helped me solve issues that occurred as the project progressed, and with whom I spent countless hours discussing the resulting data.

I would also like to extend my gratitude to Mikael Hörndahl, Svante Bouvin, Laura Folkers, Axel Bjerke and Filip Lenrick, who all assisted me at various points during the project.

My heartfelt appreciation goes to my family, Thorbjörn Bertilsson, Marie Jönsson and Hampus Bertilson, who all, in their own ways, helped me focus on other things besides this project and made sure I stayed sane. They were also always willing to listen to me talk about the project, both the broad concepts and in, I am sure, excruciating detail.

Glossary with Abbreviations

Age hardening
A hardening heat treatment technique used to precipitate a new phase from a supersaturated solid solution kept at a certain temperature.

Allotrope
The stable crystalline form of an element at a given temperature.

Alloy
A metallic substance that is composed of two or more elements.

Atomic percent at.%
A concentration measure (expressed as %) of the number of atoms of an element relative to the total number of atoms in the alloy.

Backscattered electron BSE
An electron with an energy level of 50 eV or more, emitted from a material by a focused electron beam.

Body centred cubic bcc
A crystal structure with a cubic unit cell where atoms are positioned at the corner and body-centered positions.

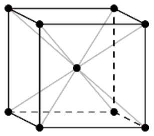

Compaction
Application of pressure to densify and shape powder in a die.

Crystal structure
The ordered arrangement of atoms, ions or molecules in a crystalline material where the smallest repeating unit is called a unit cell.

Differential scanning calorimetry DSC
A thermal analysis technique that measures the heat flow into or from a substance, compared to a reference while heating or cooling at a constant rate.

Diffraction
The spreading of waves, such as electromagnetic radiation, around obstacles.

Diffusion
The mass transport by atomic motion driven by concentration (chemical potential) gradient in a material. In crystals the diffusion occurs by either interstitial or substitutional (self-diffusion) mechanisms.

Endothermic
A process or reaction that absorbs heat upon occurring.

Energy-dispersive spectroscopy EDS
A quantitative technique that measures the chemical composition by detecting emitted x-rays, which are generated in the sample by a focused electron beam.

Equiatomic
A composition of an alloy containing equal number of atoms of two or more elements.

Eutectic reaction
A reaction in which a liquid phase transforms isothermally and reversibly upon cooling into two distinct solid phases.

Eutectoid reaction
A reaction in which a solid phase transforms isothermally and reversibly upon cooling into two other solid phases.

Exothermic
A process or reaction that releases heat upon occurring.

Face centred cubic fcc
A crystal structure with a cubic unit cell where the atoms are positioned at the corner and face-centered positions. Stacking of close-packed planes in the sequence ABCABCABC….

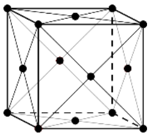

Ferromagnetic
A material that behaves as a permanent magnet due to parallel alignment of neighbouring magnetic moments.

Hexagonal close packed hcp
A crystal structure with a hexagonal unit cell that is created by stacking of close-packed planes of atoms in the sequence ABABAB….

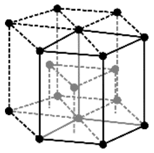

Hysteresis
The irreversible behaviour of a material that is dependent on a process, such as deformation.

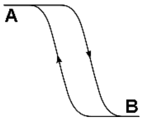

Intermetallic compound
A solid state material with an ordered structure and defined stoichiometry, made from two or more metallic elements.

Isothermal
A reaction or process that occurs at a constant temperature.

Metastable
A stable state of a system or matter that is not the state of least energy.

Miscibility gap
A region in a phase diagram which corresponds to two or more phases.

Paramagnetic
A material that is weakly attracted by an externally applied magnetic field.

Phase evolution
Occurrence of various phases in a system, which is usually associated with formation of thermodynamically stable phases.

Powder
Discrete particles of a solid substance, characterised by their small size, usually less than 1 mm.

Powder metallurgy	PM	A collective term for the knowledge and technique through which metal powders are fabricated and utilised to produce massive material and shaped components.
Precipitates		Small and ideally homogeneous and uniform particles formed within a supersaturated solid solution phase.
Scanning electron microscopy	SEM	A microscopy technique that uses a focused beam of electrons that scans the surface of a specimen in order to generate an image through detecting the reflected or emitted electrons from the surface.
Secondary electron	SE	An electron that leaves the sample electron shells with an energy that is lower than 50 eV.
Shape memory alloy	SMA	An alloy that exhibits both the shape memory effect and superelasticity.
Shape memory effect	SME	The ability of a material to reversibly recover its original shape after deformation if heated.
Sintering		A thermal process that increases the strength of a powder mass by inter-particle bonding through diffusion and related atomic level events.
Solid solution		A homogeneous crystalline phase composed of two or more chemical elements.
Stoichiometric compound		A chemical compound of two or more elements which exactly the same ratio specified by its chemical formula.
Superelasticity		The ability of a material to maintain its shape and dimension to a high extent without permanently deforming under an applied stress.
Thermomechanical treatment		A processing technique through which a mechanical deformation, combined with a heat treatment process, is applied to a material.
X-ray diffraction	XRD	An analytical technique used to identify a crystalline material by directing an incident beam of x-rays onto a specimen where the angles and intensities of the diffracted beams are measured.

List of Figures

List of Tables

Contents

1. Introduction

1.1. Background

The ternary Ni-Ti-Fe system is comprised of three binary systems: Ni-Ti, Ni-Fe and Ti-Fe. The features of the three binary phase diagrams are described, along with the shape memory effect (SME) present in the NiTi intermetallic compound. The ability to tailor the SME by adding iron as a third element to the Ni-Ti system is discussed, as is the available information regarding the ternary Ni-Ti-Fe system and isothermal sections of its phase diagram.

1.1.1. Nickel-Titanium System

The binary Ni-Ti phase diagram in Figure 1 shows the three intermetallic compounds in the system: Ni_3Ti, NiTi, and $NiTi_2$. Pure nickel has the fcc (face centred cubic) crystal structure and melts at 1455 °C. It can dissolve up to 13.7 at.% Ti at 1300 °C, this temperature is also the eutectic point of the mixture between γ-Ni and Ni_3Ti. The Ni_3Ti and NiTi intermetallic compounds are non-stoichiometric and stable up to their melting points at 1380 °C and 1311 °C, respectively. They form a mixture that has a eutectic point at 1120 °C. The $NiTi_2$ compound is stoichiometric, and only stable up to 984 °C. It forms a mixture with α-Ti at low temperatures up to 767 °C, and from there a mixture with β-Ti up to 942 °C, at this temperature the mixture has a eutectic point. Titanium has two allotropes, α-Ti (hexagonal close packed, hcp) and β-Ti (body centred cubic, bcc), the first exists at low temperatures and up to 882 °C. From there titanium exists in the form of β-Ti until it melts at 1670 °C. α-Ti does not dissolve any substantial amount of Ni, but β-Ti can dissolve up to 10 at.% Ni at 942 °C [1-3].

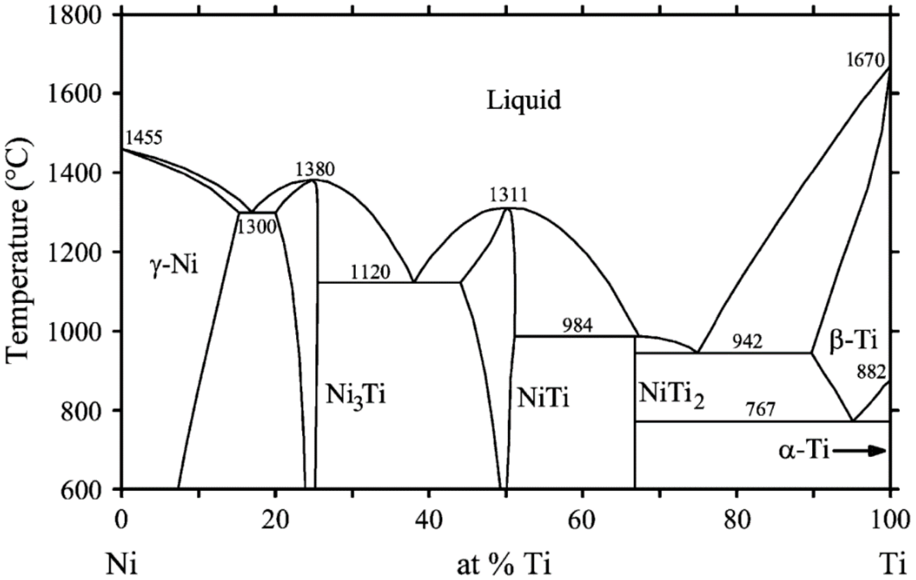

Figure 1. Binary Ni-Ti phase diagram [1].

NiTi Shape Memory Alloy

The intermetallic compound NiTi is a shape memory alloy (SMA), which is defined by two properties: the shape memory effect (SME) and superelasticity. The shape memory effect is the ability of the material to, after being deformed at a low temperature, recover its original shape through heat treatment. A material with superelasticity can deform due to an applied stress, and then recover its original shape when the stress is removed [4-6]. The SME differs from superelasticity in that the deformation is not reversed when the stress is removed, and the material needs to be heated to recover its original shape.

The shape memory effect and superelasticity are based on the martensitic transformation, which is a diffusionless phase transformation [4]. For the SME in NiTi the transformation is between two crystal structures, the cubic, austenite phase denoted B2 and the monoclinic, martensite phase called B19′. The martensitic transformation can occur in one or two steps, either B2 → B19′, or B2 → R → B19′, see Figure 2. The intermediate martensitic R-phase has a trigonal crystal structure [4, 7]. The two step transformation via the R-phase occurs in relation to stress fields surrounding precipitates and dislocations [7]. These can be introduced into the material through ageing, thermomechanical treatment, alloying with a third element or if the NiTi is rich in nickel. These factors also affect the transformation temperatures for the SME [4, 8, 9]. If the material contains more than 50.5 at.% Ni then the composition lies outside of the NiTi phase region, see Figure 1. This leads to the formation of precipitates of the metastable phase Ni_4Ti_3. Addition of alloying elements can also cause precipitates to form [3, 4].

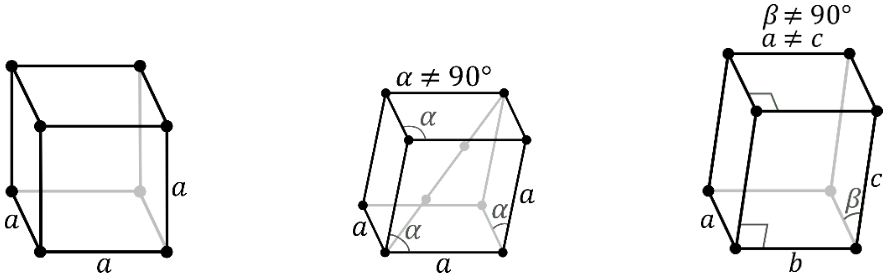

Figure 2. The cubic crystal structure of the B2-phase (left) [10], the trigonal crystal structure of the R-phase (middle) [11], and the monoclinic crystal structure of the B19′-phase (right) [12].

Of the crystal structures involved in the NiTi SME the B2 phase is stable at higher temperatures while the martensitic B19′-phase is stable at low temperatures [4, 5]. The SME depends on three variables: temperature, strain and external stress. A change in one or two of these can induce a large change in the other variables [4]. The transformation from B2 to B19′ starts at the martensite start temperature (M_s) and ends at the martensite finish temperature (M_f). The reverse transformation occurs between the austenite start temperature (A_s) and the austenite finish temperature (A_f). For NiTi the possible SME temperature interval ranges from below 0 °C up to 120 °C, depending on composition and thermomechanical treatment [4, 13]. As can be seen in Figure 3 the M_s and A_f, at which the material is mostly in its high temperature B2-phase, do not necessarily match. The same is true for the M_f and A_s, at which the material is mostly in its low temperature B19′-phase. This temperature difference is the hysteresis for the SMA, defined as $(A_f - M_s)$ [5].

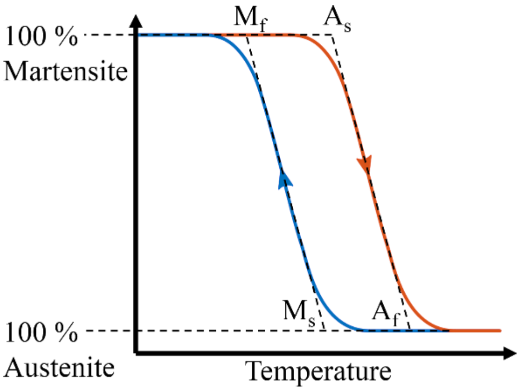

Figure 3. Illustration of the start and finish temperatures and hysteresis $(A_f - M_s)$ for the SME.

The hysteresis in the B2 → B19′ transformation is large, up to over 40 °C [1, 14]. For the B2 → R transformation the hysteresis is very small, about 1-2 °C. The trade-off is a small shape change, about 1 %, compared to the 8.5 % possible for the full B2 → B19′ transformation [5]. Different applications can make use of either a large or a small hysteresis. For example, a small hysteresis is required for fast actuation applications, as in micro-electromechanical systems. A large hysteresis is important for components that are required to maintain a defined shape within a large temperature range [4, 5].

The advantage of NiTi based SMAs is their relative stability, ductility, biocompatibility and good thermomechanical performance compared to other shape memory alloys, such as iron-based or copper-based SMAs. The NiTi shape memory alloy is used in several industries including automotive, aerospace, robotic and biomedical. [4, 5]. Producing NiTi components using powder metallurgy allows for near-net shape processing [4]. This minimises the amount of processing steps that are needed to achieve the final product, reducing the time and cost to produce the component. Powder metallurgy also allows for more complex designs of the products, and better control of the composition and thus of the transformation temperatures [4].

1.1.2. Nickel-Iron System

The binary Ni-Fe phase diagram, Figure 4, shows that for a large temperature range nickel and iron form a solid solution, γ-(Fe,Ni). The intermetallic compound $FeNi_3$ exists at lower temperatures, up to 517 °C, and is the only stable intermetallic compound in the Ni-Fe system. Pure iron exists as α-Fe (bcc) at low temperatures up to 912 °C where it transforms into γ-Fe (fcc), and then at 1394 °C it transforms back into the bcc crystal structure, which at high temperatures is called δ-Fe. The temperatures at which the pure elements, nickel and iron, melts are 1455 °C and 1538 °C, respectively. α-Fe and δ-Fe can dissolve up to 5 at.% Ni and 3 at.% Ni, respectively [1-3].

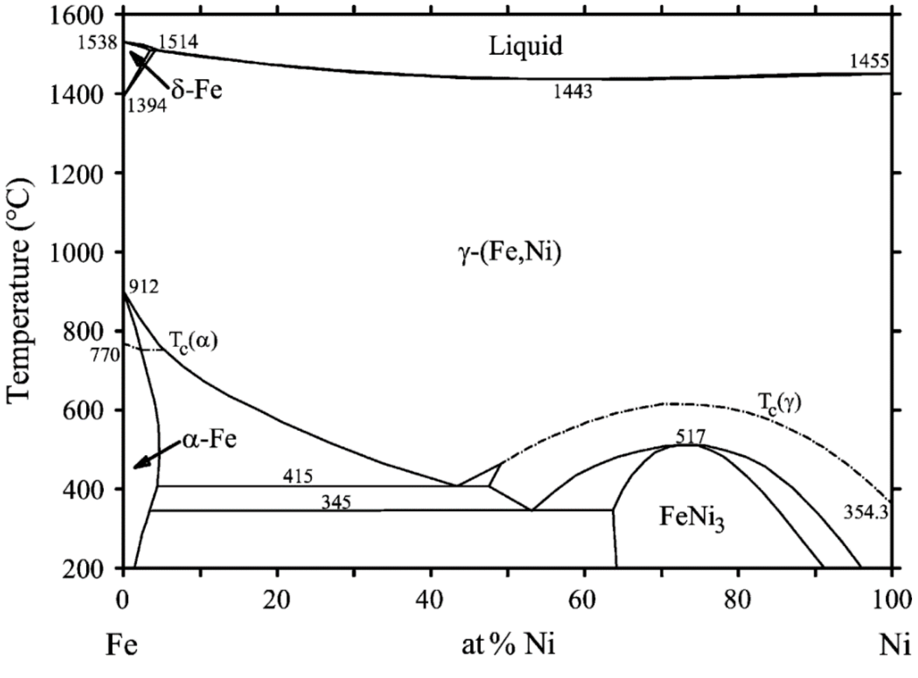

Figure 4. Binary Ni-Fe phase diagram [1].

Iron and nickel are both ferromagnetic at room temperature; at higher temperatures, these elements become paramagnetic. The Curie temperature, T_c, is the critical temperature below which the material is ferromagnetic, and when the temperature is increased above T_c the material becomes paramagnetic [6]. The dashed lines in Figure 4 corresponds to the Curie temperatures for different compositions in the system. The miscibility gap present in the phase diagram is induced by the magnetic transition [1].

1.1.3. Titanium-Iron System

Figure 5 shows the Ti-Fe phase diagram and its two intermetallic compounds, $TiFe_2$ and TiFe. As mentioned previously pure iron has two crystal structures, bcc (α-Fe) and fcc (γ-Fe). Pure titanium has two allotropes, α-Ti (hcp) and β-Ti (bcc). The allotropes of the pure elements exist in the same temperature ranges as mentioned previously, with the δ-Fe here being the high temperature α-Fe. The two intermetallic compounds, $TiFe_2$ and TiFe, are non-stoichiometric and stable up to 1427 °C and 1317 °C, respectively. α-Fe and $TiFe_2$ forms a mixture that has a eutectic point at 1293 °C. Iron is ferromagnetic below T_c, this also applies to the iron in the mixture of α-Fe and $TiFe_2$. Above T_c they become paramagnetic. γ-Fe can dissolve less than 1 at.% Ti, but α-Fe can dissolve up to 10 at.% Ti. Similar to nickel, iron does not dissolve to a significant extent in α-Ti, but the solubility of iron in β-Ti reaches its highest value of 22 at.% Fe at 1082 °C. It is also at this temperature that the mixture of TiFe and β-Ti has its eutectic point [1-3].

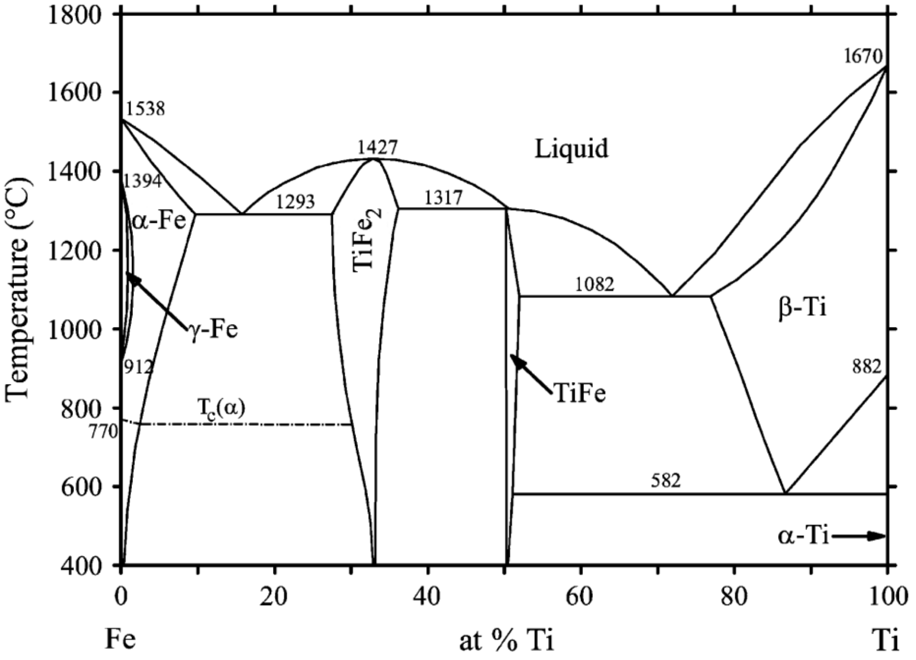

Figure 5. Binary Ti-Fe phase diagram [1].

The eutectoid point, for the α-Ti + TiFe → β-T transformation, exists at 582 °C. This temperature is almost 200 °C lower than the eutectoid point for the α-Ti + $NiTi_2$ → β-T transformation, found in the Ni-Ti phase diagram, see Figure 1. Since neither iron nor nickel is soluble in α-Ti, the earlier transformation of α-Ti → β-Ti in the Ti-Fe phase diagram shows that iron can start to dissolve into titanium at a lower temperature than nickel can.

1.1.4. Nickel-Titanium-Iron System

The ternary Ni-Ti-Fe system is poorly known considering the importance of alloys based on the individual elements, especially since many of these alloys contain one or both of the other two elements. No ternary phase has been found to exist in the Ni-Ti-Fe system, but the binary Ni_3Ti, $NiTi_2$ and $TiFe_2$ phases show large solubility of the third element [1-3]. Thermodynamic calculations of the ternary Ni-Ti-Fe system has been made, but not everything has been confirmed experimentally, and not all of the experimental results are in agreement [1-3, 15].

An isothermal section of the Ni-Ti-Fe phase diagram at 900 °C is shown in Figure 6. Among the intermetallic compounds present at this temperature are $TiFe_2$, which can dissolve up to 30 at.% Ni, and also Ni_3Ti and $NiTi_2$, these can dissolve up to 20 at.% Fe and 30 at.% Fe, respectively. TiFe and NiTi have similar crystal structures and form a continuous solid solution at about 50 at.% Ti. $NiTi_2$ extends almost to the Ti-Fe binary, but not completely since the Ti_2Fe is not stable in the Ti-Fe binary system [1-3]. Due to the very high solubility of nickel in Ti_2Fe, it is at times referred to as $(Fe,Ni)Ti_2$. In Ni_3Ti and $NiTi_2$ the dissolved iron can act as a substituent to nickel, and in $TiFe_2$ the dissolved nickel will take the place of iron [1, 3]. Combined with the solid solutions, (Fe,Ni)Ti and γ-(Fe,Ni), this makes the iron and nickel largely interchangeable in the Ni-Ti-Fe system.

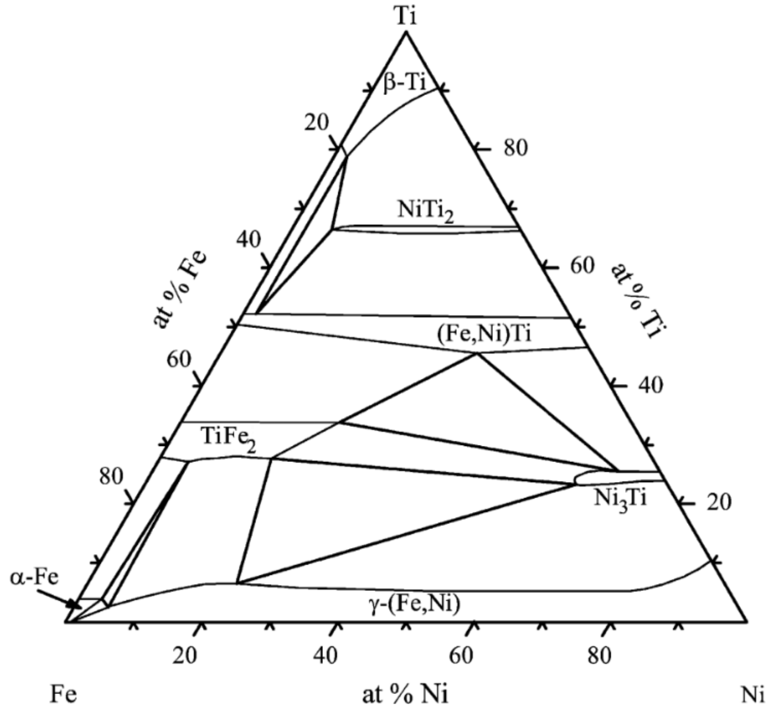

Figure 6. Isothermal section at 900 °C of the ternary Ni-Ti-Fe phase diagram [1].

Figure 7 shows the isothermal section of the Ni-Ti-Fe phase diagram at 1000 °C. The bottom half, containing less than 50 at.% Ti has not changed much, compared to the isothermal section at 900 °C. The compositional extent of the phases has shifted some, and γ-(Fe,Ni) can for certain compositions dissolve a lot more titanium. In the top half of the isothermal section in Figure 7 the majority of the $NiTi_2$ phase has disappeared in favour of a liquid extending from the Ni-Ti binary. The $NiTi_2$ is however still stable for a small compositional range close to the Ti-Fe binary. The dashed lines in Figure 7 indicates that the extent of the concerned phases is uncertain.

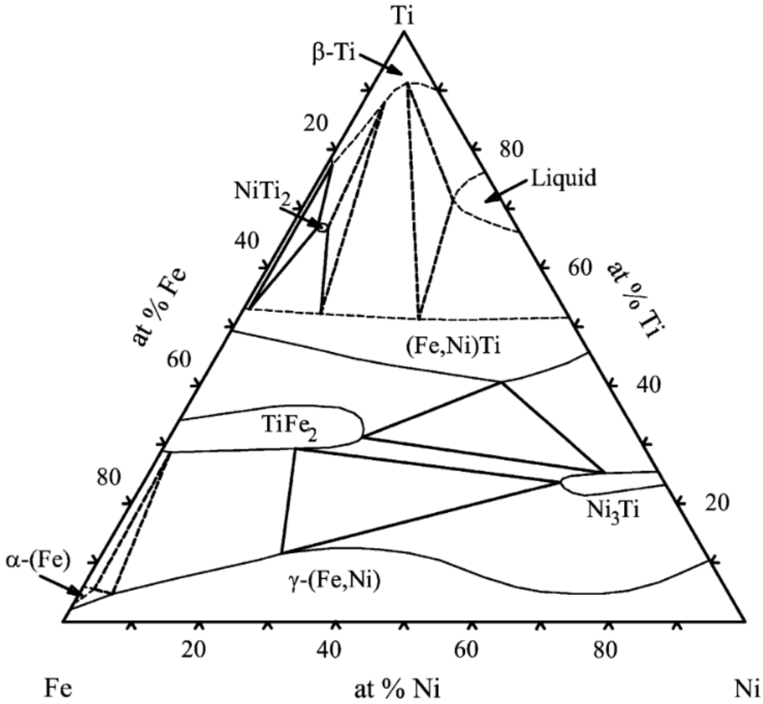

Figure 7. Isothermal section at 1000 °C of the ternary Ni-Ti-Fe phase diagram [1].

An example of how the Ni-Ti-Fe system is poorly known is the lack of an agreed upon reaction scheme for the system, see Table 1. Some of the proposed reactions are more supported than others are, but even in those cases, the given temperatures can vary by up to 70 °C. This disagreement makes it difficult to predict which phases could be present at different temperatures. Additionally the reactions in Table 1 are given for when the system is in equilibrium. This is not a state found in practice and phases can exist outside of their stability range due to kinetics.

Table 1. Proposed reactions in the Ni-Ti-Fe reaction scheme.

Reaction	Temperature (°C)	Source
L → $TiFe_2$ + Ni_3Ti	max 1320	[1]
	1320	[3]
L + $TiFe_2$ → (Fe,Ni)Ti	1317	[3]
L → γ-(Fe,Ni) + Ni_3Ti	1304	[1, 15]
L + δ-Fe → γ-(Fe,Ni) + $TiFe_2$	1200	[1, 3]
	1270	[2]
	~1199	[15]
L → $TiFe_2$ + Ni_3Ti	1187	[2]
	max ~1150	[15]
L → (Fe,Ni)Ti + Ni_3Ti	1120	[3]
L +$TiFe_2$ → (Fe,Ni)Ti + Ni_3Ti	1118 < T < 1317	[1]
	?	[3]
L → γ-(Fe,Ni) + Ni_3Ti + $TiFe_2$	1110	[1]
	1123	[2]
	1113	[3]
	~1109	[15]
L → (Fe,Ni)Ti + $TiFe_2$ + Ni_3Ti	1103	[2]
	~1099	[15]

Reaction	Temperature (°C)	Source
L → β-Ti + (Fe,Ni)Ti	1085 1081	[3] [2]
L → β-Ti + $NiTi_2$	1044	[2]
L + β-Ti → (Fe,Ni)Ti + $NiTi_2$	1043	[2]
L + NiTi → $NiTi_2$	max ~1030 max ~1035	[1] [15]
L + (Fe,Ni)Ti → $(Fe,Ni)Ti_2$ + β-Ti	~1030	[15]
L + (Fe,Ni)Ti → β-Ti + $NiTi_2$	~1025 960	[1] [3]
L + (Fe,Ni)Ti → NiTi	985	[3]
L + (Fe,Ni)Ti → $NiTi_2$	985	[2]
β-Ti + $NiTi_2$ → α-Ti + (Fe,Ni)Ti	650	[3]
β-Ti → α-Ti + (Fe,Ni)Ti	590	[3]

Diffusion

Transition metal elements, such as nickel and iron exhibit fast diffusion in α-Ti, between four and five orders of magnitude faster than the self-diffusion of titanium. In β-Ti the diffusion rate of nickel and iron is at least one order of magnitude faster than the self-diffusion [1, 16]. The diffusivity of nickel and iron in titanium is very similar and increases with increasing temperature. The diffusion mechanism of the transition metal elements in titanium is believed to be a type of interstitial mechanism [16]. Comparisons of the diffusion rate of titanium in α-Fe with the diffusion rates of nickel and iron in titanium indicates that the diffusivity of the two latter are faster than the diffusion of titanium in α-Fe [16, 17].

Concerning the diffusion of nickel and titanium in β-Ti(Ni), $NiTi_2$ and NiTi, nickel was found to be by far the fastest moving component. For NiTi consisting of 50-53 at.% Ni, in the temperature range between 550 °C and 940 °C, the diffusion occurs almost exclusively by the motion of the nickel atoms [18]. Since iron appears to diffuse similarly to nickel then it is possible that iron is also a fast diffuser in β-Ti(Ni), $NiTi_2$ and NiTi.

Shape Memory Effect

The purpose of adding iron to the Ni-Ti system when it comes to the SME is that iron can affect the properties of the martensitic transformation [3]. The NiTi intermetallic compound responsible for the SME is very sensitive to the ratio of nickel to titanium, and if it is slightly richer in nickel, then metastable Ni_4Ti_3 precipitates can form [3, 4]. Iron is able to substitute nickel in NiTi and can thus be used to promote the formation of Ni_4Ti_3. This is one method of introducing the intermediate R-phase into the martensitic B2 → B19′ transformation as well as stabilising it [7]. Iron is also able to decrease the transformation temperatures of both steps in the B2 → R → B19′ transformation, as well as separate them in temperature [2-4, 19].

With equiatomic amounts of nickel and titanium, the maximum amount of iron that can be added while remaining within the (Fe,Ni)Ti phase region is approximately 8 at.% Fe at 900 °C and 18 at.% Fe at 1000 °C, according to the isothermal sections of the Ni-Ti-Fe phase diagram in Figure 6 and 7, respectively. The majority of studies on the effect of iron on the NiTi shape memory effect has been done on systems containing 50 at.% Ti, and up to 9 at.% Fe [1, 7, 9, 20-22]. Presumably to be able to stay within or very close to the (Fe,Ni)Ti region at lower temperatures. By doing so, the material could benefit from both the superior properties of a composition close to the equiatomic NiTi, and the separation of the B2 → R and R → B19′

transformations. By separating the transformations the small hysteresis associated with the R-phase can be utilised in applications that need to be able to quickly change shape [3]. Examples of such applications are miniaturised actuators to be used in microrobots [4]. SMA based on the Ni-Ti-Fe system is also useful in low temperature applications as the iron lowers the martensitic transformation temperatures down below 0 °C [1].

1.2. Objective

The aim of this project was to provide a deeper understanding of the intermetallic compound formation in the ternary Ni-Ti-Fe system. The focus was on how iron affected the phase evolution in the system and how it differed from the binary Ni-Ti system.

2. Materials and Methods

The experimental work done includes sample preparation, differential scanning calorimetry (DSC), scanning electron microscopy (SEM), complemented by energy-dispersive spectroscopy (EDS), and x-ray diffraction (XRD). Elemental powders of nickel, titanium and iron were mixed to create powder mixtures of different compositions, based on equiatomic amounts of nickel and titanium. The powders were compacted into discs and sintered at different temperatures. The sintering process was studied using DSC. Further analysis of the microstructure and phase evolution was done by SEM, EDS and XRD.

2.1. Sample Preparation

The elemental metal powders of nickel, titanium and iron used in this project are listed in Table 2. The nickel and titanium powders both had a maximum particle size of 45 µm, and the iron powder had an average particle size of 6-8 µm. Equal particle size of the nickel and titanium promotes a homogeneous mixture of the two. The smaller size of the iron powder means there will be a larger number of particles present compared to if the powder consisted of particles of a larger size. A greater number of iron particles makes it more probable that there will be an iron particle in close proximity to each nickel and titanium particle and smaller particles have a larger surface to volume ratio. Both of these factors promote interaction between the iron and the nickel and titanium.

Table 2. Metal powders used in this project.

Powder [a]	Particle size (µm)	Purity (%)
Nickel	≤ 45	99.5
Titanium	≤ 45	99.5
Iron	6-8 [b]	99.0

[a] Supplied by Goodfellow (UK), [b] average.

Preparation of the samples started with creating a master mixture of equiatomic amounts of nickel and titanium. It was mixed using a shaker mixer (TURBULA® T 2 F), which ran at 72 rpm for 20 minutes. Using the master mixture smaller mixtures of Ni-Ti-Fe was prepared according to the compositions listed in Table 3. These were also mixed in the shaker mixer at 72 rpm for 20 minutes. Binary mixtures of nickel and iron, and of titanium and iron were made in addition to the equiatomic NiTi-0Fe. The compositions of these are also listed in Table 3.

Table 3. Chemical compositions of the samples.

Sample	Nickel (at.%)	Titanium (at.%)	Iron (at.%)
NiTi-0Fe	50	50	-
NiTi-2Fe	49	49	2
NiTi-4Fe	48	48	4
NiTi-6Fe	47	47	6
NiTi-8Fe	46	46	8
NiTi-10Fe	45	45	10
NiTi-15Fe	42.5	42.5	15
NiTi-20Fe	40	40	20

Sample	Nickel (at.%)	Titanium (at.%)	Iron (at.%)
Ni-10Fe	90	-	10
Ni-50Fe	50	-	50
Ti-10Fe	-	90	10
Ti-50Fe	-	50	50

A hydraulic press (ENERPAC P-392) was used to uniaxially press the powder mixtures into discs that could be used in the differential scanning calorimeter. The discs were 4 mm in diameter and approximately 1 mm thick. The compaction pressure used was 25 MPa.

2.2. Differential Scanning Calorimetry (DSC)

Differential scanning calorimetry (DSC) is a thermal analysis technique that measures the change in heat flow rate as a function of temperature as a material is heated or cooled. Both chemical and physical changes can occur in a material as its temperature is altered, examples of these are: changes in crystal structure, melting and solidification [6, 23]. The changes can either, release energy as they occur (exothermic) or they absorb energy (endothermic). As an example, the melting process is endothermic while the solidification process is exothermic.

2.2.1. Differential Scanning Calorimeter

The main parts of a differential scanning calorimeter is the chamber with the sample holder, surrounded by heating elements, the systems for evacuation, gas supply and cooling, and the balance system to measure the sample mass change, see Figure 8. The machine measures the difference in heat flow rate between the sample and a reference [23]. It operates in a controlled atmosphere. Evacuation of the chamber combined with purging and protective gases work together to create the desired atmosphere.

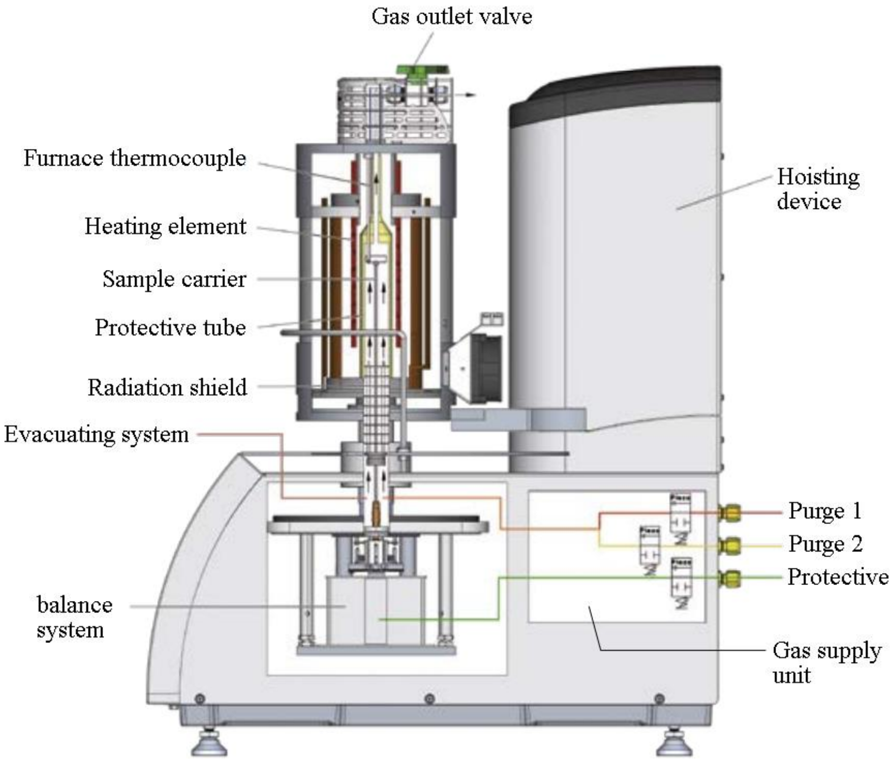

Figure 8. Schematic of a differential scanning calorimeter (NETZSCH STA 449 F3 Jupiter) [24].

The data from a measurement is in the form of a graph with the heat flow plotted against either time or temperature. These will be called DSC curves, see Figure 9. A measurement also gives data about the mass change of the sample; this can be plotted against either time or temperature. The basic features of a DSC curve are illustrated in Figure 9. Deviations from the baseline are either endothermic or exothermic. The onset temperature of a peak is measured as shown in Figure 9, and the area of a peak is the area between the curve and the extrapolated baseline.

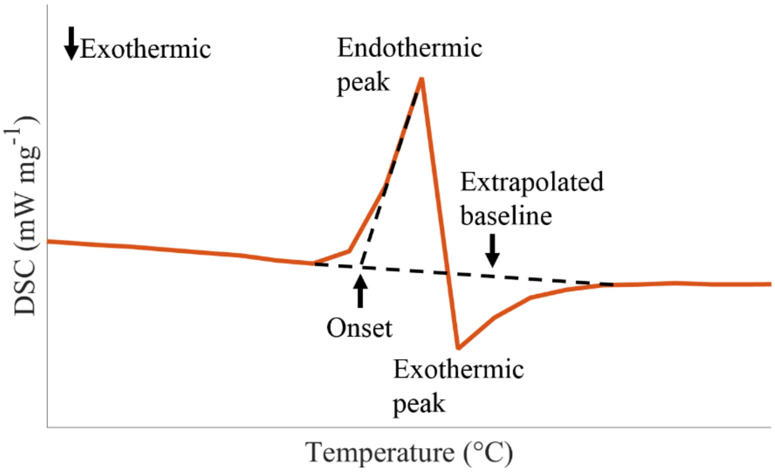

Figure 9. Basic features of a DSC curve.

2.2.2. DSC Experimental Procedure

The differential scanning calorimeter used in this project was a NETZSCH STA 449 F3 Jupiter, see Figure 8, its temperature operating range was from room temperature to 1550 °C. The sample was placed into an alumina crucible, and an empty alumina crucible was used as a reference. These were placed on the sample holder in the chamber of the machine. The chamber was evacuated and flushed with argon gas at least three times, to avoid oxidation of the sample during heating. The heating and cooling rate was 10 °C min^{-1} and a protective argon gas flow of 20 ml min^{-1}, combined with a purging argon gas flow of 50 ml min^{-1}, was maintained during the heating and cooling.

The first step for the DSC was to calibrate the machine; it was done using pure metal standards: tin, aluminium, silver and gold. The metals were heated to a temperature above their respective melting point, so that both the endothermic melting and exothermic solidification could be measured by the differential scanning calorimeter. A temperature baseline correction was made by heating empty alumina crucibles to 1200 °C.

Each DSC experiment started at room temperature and the sample was heated to a maximum of 1200 °C. The sample was after the heating step cooled down to room temperature by the machine. For the different compositions of the Ni-Ti-Fe system, so called interrupted runs were performed. This was to allow further analysis of events recorded during the initial measurement to 1200 °C. The temperatures for these runs are listed in Table 4.

Table 4. Interruption temperatures, in addition to 1200 °C.

Sample	Stop temperatures (°C)
NiTi-6Fe	900, 970, 1000, 1030, 1115, 1140
NiTi-10Fe	900, 960, 1000, 1030, 1060, 1110, 1150
NiTi-15Fe	1090
NiTi-20Fe	1090

For each composition and interruption temperature at least two experiments were performed. The DSC data was analysed and compared in terms of onset temperatures, peak areas and peak temperatures with NETZSCH Proteus Thermal Analysis software (version 6.1.0).

2.3. Scanning Electron Microscopy (SEM)

Scanning electron microscopy (SEM) is an imaging technique that utilises a beam of electrons to reproduce an image of the surface of a material. The electron beam scans the surface and interacts with the atoms in the material to create a set of signals that can be recorded by different detectors [6, 25].

Energy-dispersive spectroscopy (EDS) utilises x-rays generated in the material by the electron beam to identify the elements present in the material [6, 25].

2.3.1. Scanning Electron Microscope

The main components of a scanning electron microscope are, an electron gun, a set of apertures and magnetic lenses, and a set of detectors, all positioned at least partially within an evacuated chamber, see Figure 10. The electrons generated by the electron gun are focused onto a spot on the sample by the lenses. There the electrons interact with the atoms close to the surface, and in doing so give rise to a variety of signals, see Figure 11. The electron beam is scanned over the surface of the sample and detects the generated signals from each point to create an image of the surface. The system needs to be evacuated, to avoid the electrons interacting with atoms in the air on their way from the electron gun to the sample, and from there to the detectors.

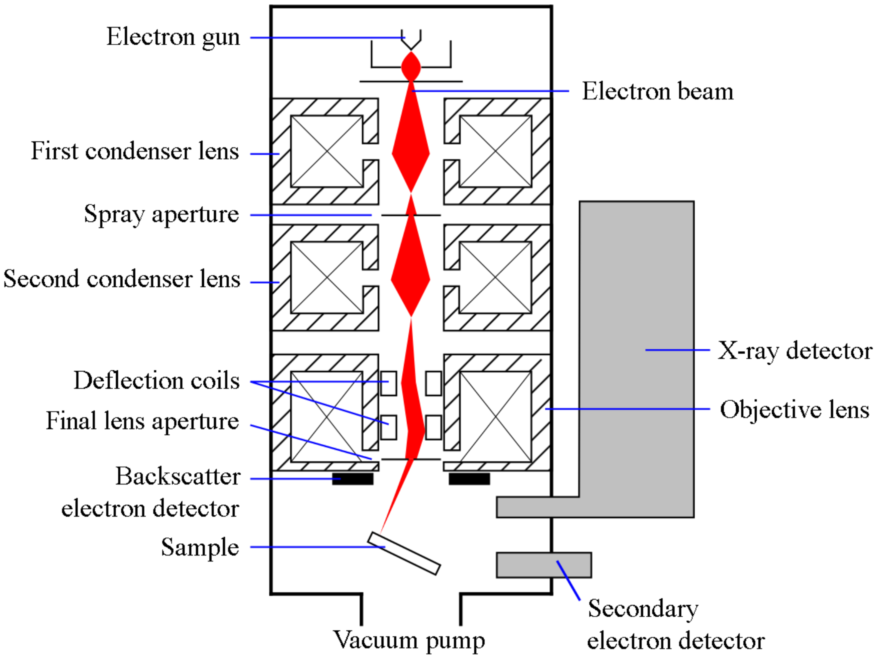

Figure 10. Schematic of a scanning electron microscope [26].

A scanning electron microscope can create an image of the sample surface in two main ways, by detecting the secondary electrons (SE) or by detecting the backscattered electrons (BSE). As can be seen in Figure 11 the secondary electrons come from a narrow volume close to the surface and the backscattered electrons can come from further down in the sample. SE originate from the atoms in the sample, these electrons have, due to interactions with the electron beam, been given enough energy to leave their atoms and can be collected by a detector. BSE are electrons from the beam that have close to reversed their direction when they interacted with the sample and their detector is positioned around the electron beam, see Figure 10. In broad terms the SE are used to image the topography of the surface and the BSE are used to image the chemical composition of the surface [6].

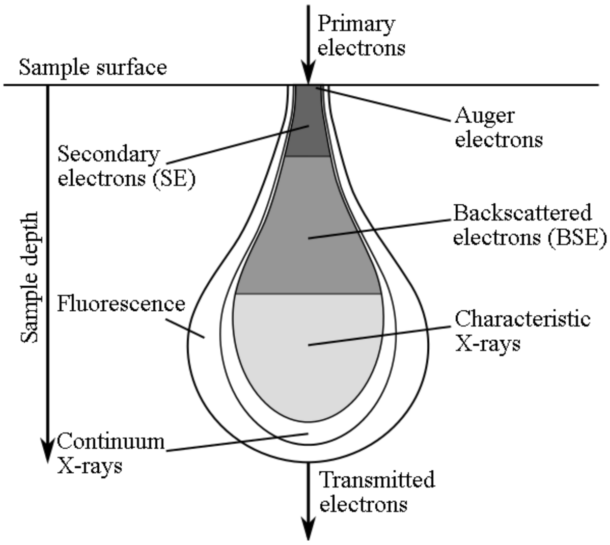

Figure 11. Interaction volume of an electron beam and various signals generated.

The signals depicted in Figure 11 can all be used to give varying kinds of information about the sample. The characteristic x-rays are used in energy-dispersive spectroscopy (EDS). An electron from the beam can give some of its energy to an electron in the sample. If enough energy is provided that electron can leave its atom and becomes a secondary electron. But if the amount of energy transferred is lower the electron in the sample enters a higher energy state. When returning to a more favourable lower energy state characteristic x-rays are emitted. These x-rays can then be detected and provide information about which elements are present in the sample [6, 25]. EDS can be used to estimate the composition in a spot or region of the sample. It can also create maps of where the different elements are located in the sample.

The characteristic x-rays originate from deeper within the sample than the BSE, see Figure 11. Thus the composition given by the EDS may not be in complete agreement with the image provided by the BSE. It is therefore important to make multiple measurements on regions that are visually the same, in case another phase lies just beneath the surface.

2.3.2. Sample Preparation for SEM

Prior to examining the samples in the scanning electron microscope, they had to go through a grinding and polishing procedure to create an even surface suitable for microstructure analysis. The grinding and polishing were performed both manually and with a polishing machine (Struers RotoPol-22), which used a rotational speed of 150 rpm.

Silicon carbide (SiC) grinding papers and polishing cloths (Struers) were used to grind and polish the samples. The grinding papers have different grits depending on the size of the SiC particles on them, a smaller grit number corresponds to larger particles, and papers with higher girt number have smaller particles. SiC papers with grits of 2000 and then 4000 were used to gradually create a smoother surface. For the most uneven samples, SiC papers with a grit of 1000 was used as a first step. After grinding the surface as even as possible, a polishing cloth was used in an effort to remove the scratches left over from the grinding steps.

2.3.3. SEM Experimental Procedure

The scanning electron microscope used in this project was a Philips, XL-30 ESEM. It had a LaB_6 solid-state crystal as electron source, and detectors for secondary electrons (SE) and backscattered electrons (BSE). It was also equipped with a liquid nitrogen cooled Si(Li) detector (EDAX) that was used for the energy-dispersive spectroscopy (EDS).

The polished samples were attached to a sample holder using conductive tape. The sample holder was placed into the chamber of the microscope, which was evacuated to about 10^{-3} mbar. An accelerating voltage of 15-30 keV was used to study the samples. SE and BSE images were taken at several magnifications and areas of the sample.

The quantitative EDS analysis was done using the Genesis software (version 5.21), based on ZAF correction and standardless calibration. Multiple measurements were performed in at least two sections of each sample to confirm the validity of the data. Finally, EDS maps were created to show the distribution of the elements.

2.4. X-Ray Diffraction (XRD)

X-ray diffraction (XRD) is a technique for determining the atomic and molecular structure of a crystal. It can also be used to identify elements or compounds by comparing the experimental diffraction pattern with already determined patterns. XRD uses x-rays, a form of electromagnetic radiation with high energy, to analyse the material. When x-rays hit the material, they are diffracted by the crystal structure, and interference causes them to have higher intensity at specific angles, depending on the crystal structure [6].

2.4.1. X-Ray Diffractometer

In an x-ray diffractometer, see Figure 12, the x-rays are produced by bombarding a metal target with electrons, this is the x-ray source [6]. The focussing monochromator allows x-rays of a specific energy to continue towards the sample. There they are diffracted and the x-rays that leave the sample at a specific angle can reach the detector. The detector moves around the sample to record the intensity of x-rays at different angles. The output data is in the form of XRD patterns that plot the intensity of the x-rays against the angle it was recorded at.

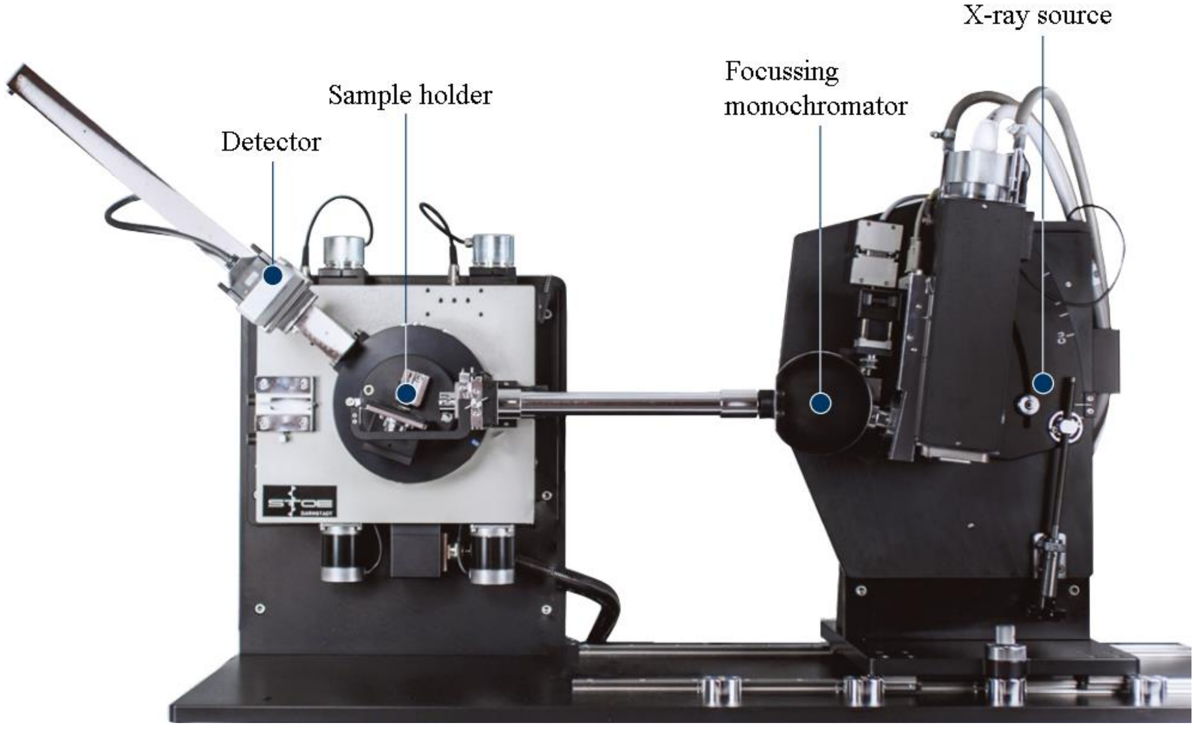

Figure 12. An x-ray diffractometer (STOE STADI-MP) [27].

2.4.2. XRD Experimental Procedure

The x-ray diffractometer used in this project was a STOE STADI-MP, see Figure 12. It had a MYTHEN 1K detector, used copper as the x-ray source and was operated in reflection mode. Calibration of the machine was done using pure nickel. The data was collected for the angles 10-120°, with a step of 0.9° and a dwell time of 10 s.

For each experiment, the sample was mounted using silicone gel onto a sample holder. They were placed onto a rotating disc between the x-ray source and a beam stopper and exposed to the x-ray beam. The diffraction data was recorded for the angles 10-120°, each step was 0.5° and the dwell time was 15 s. The software used to record the data was WinX^{POW} and the analysis of the data was done with Match! (version 3.6) using the PDF-2 Release 2004 database.

3. Results

The results from the differential scanning calorimetry is presented in the form of DSC curves. The scanning electron microscopy results, including those of the energy-dispersive spectroscopy, are in form of secondary electron and backscattered electron images, tables and maps over the distribution of nickel, titanium and iron in sections of the samples. The x-ray diffraction results are presented as diffraction patterns.

3.1. DSC Results

3.1.1. Binary Systems

The DSC heating curve for NiTi-0Fe exhibits three features of interest, see Figure 13. The first is small but broad endothermic peak between 770 °C and 850 °C. The second is a large exothermic peak in the range 946-953 °C, and the third is an endothermic peak, followed by a smaller exothermic peak, found between 1111 °C and 1131 °C. The cooling curve does not have any peaks.

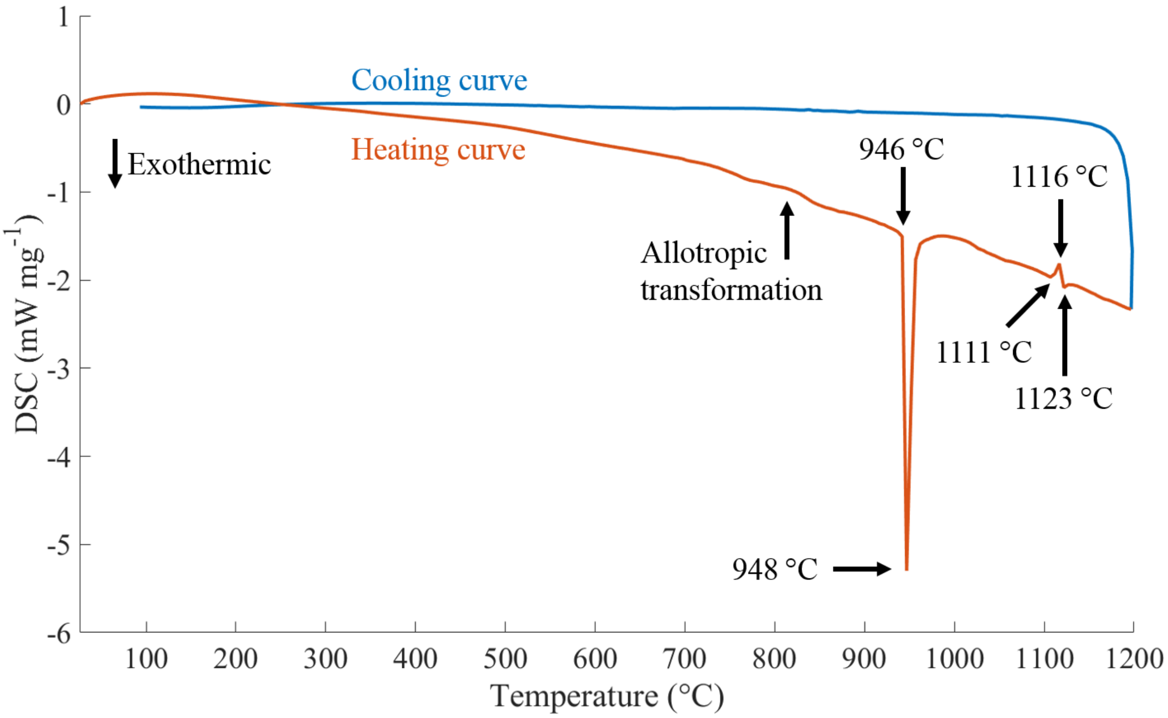

Figure 13. DSC curve for the NiTi-0Fe sample heated to 1200 °C.

The DSC curves for the binary samples: Ni-10Fe, Ni-50Fe, Ti-10Fe and Ti-50Fe, are presented in Figure 14. The first three show no clear endothermic or exothermic peaks. There may be a slight endothermic peak for Ti-10Fe around 838 °C. For the Ti-50Fe sample the DSC curve shows a combined endothermic and exothermic reaction, which has an onset temperature of 1091 °C.

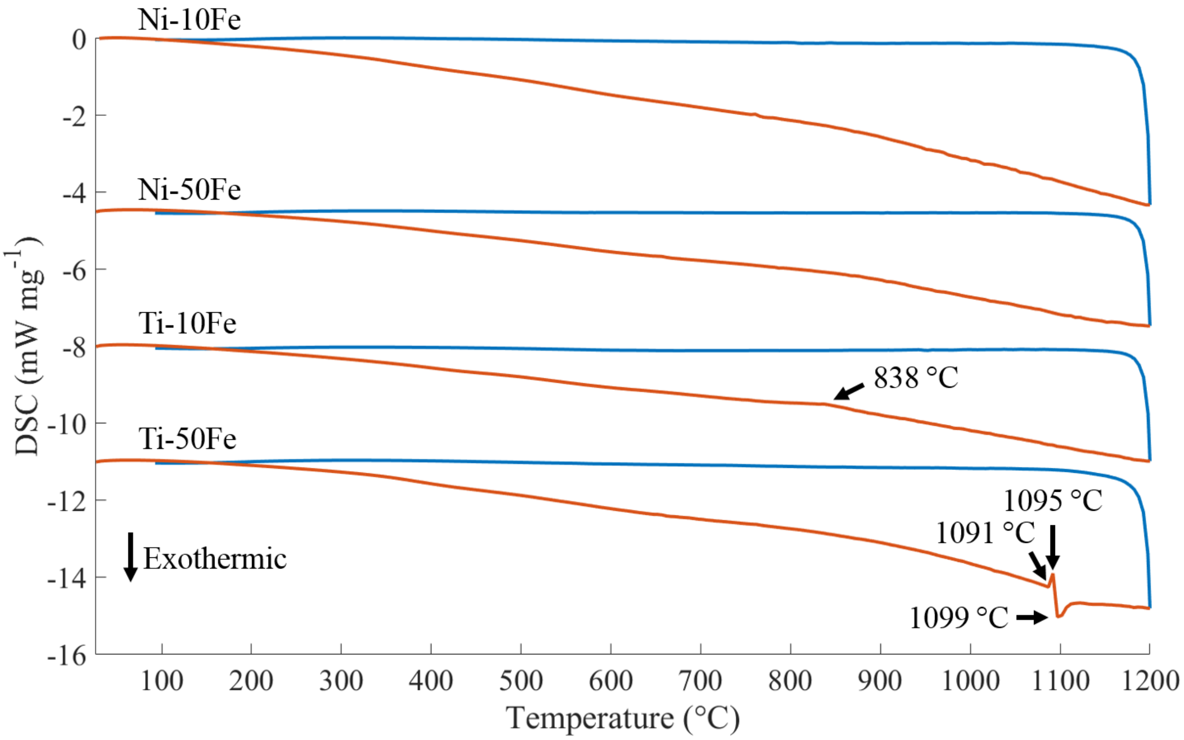

Figure 14. DSC curves for the Ni-10Fe, Ni-50Fe, Ti-10Fe and Ti-50Fe samples. Heating curves in red (bottom) and cooling curves in blue (top).

3.1.2. Ternary Systems

A collection of the DSC curves for 0-20 at.% Fe is shown in Figure 15. The onset of the large exothermic peak found in NiTi-0Fe shifts to higher temperatures as the iron content is increased. The onset temperature in the NiTi-0Fe sample is 946 °C, and in NiTi-20Fe the onset has shifted by more than 50 °C to 999 °C. The size of this peak also decreases as the iron content is increased. For the samples with higher iron content the peak has also split into two distinct peaks. This splitting of the peak is first observed in the sample NiTi-4Fe, and from there becomes more pronounced for the higher iron contents. The onset of this second part increases with the iron content, from 996 °C in NiTi-4Fe to 1027 °C in NiTi-20Fe. Its area also grows with the increase in iron content.

The combined endothermic and exothermic peak found in the NiTi-0Fe sample at 1111-1131 °C is also affected by the iron content. The size of the endothermic part of the peak grows as the iron content is increased. It is more difficult to determine how the size of the exothermic part changes. In contrast to the first exothermic peak, the onset of this combined peak does not change as much as the iron content is increased. The onset varies from its lowest value of 1097 °C in NiTi-10Fe, NiTi-15Fe and NiTi-20Fe to the highest value of 1112 °C found in NiTi-2Fe and NiTi-4Fe.

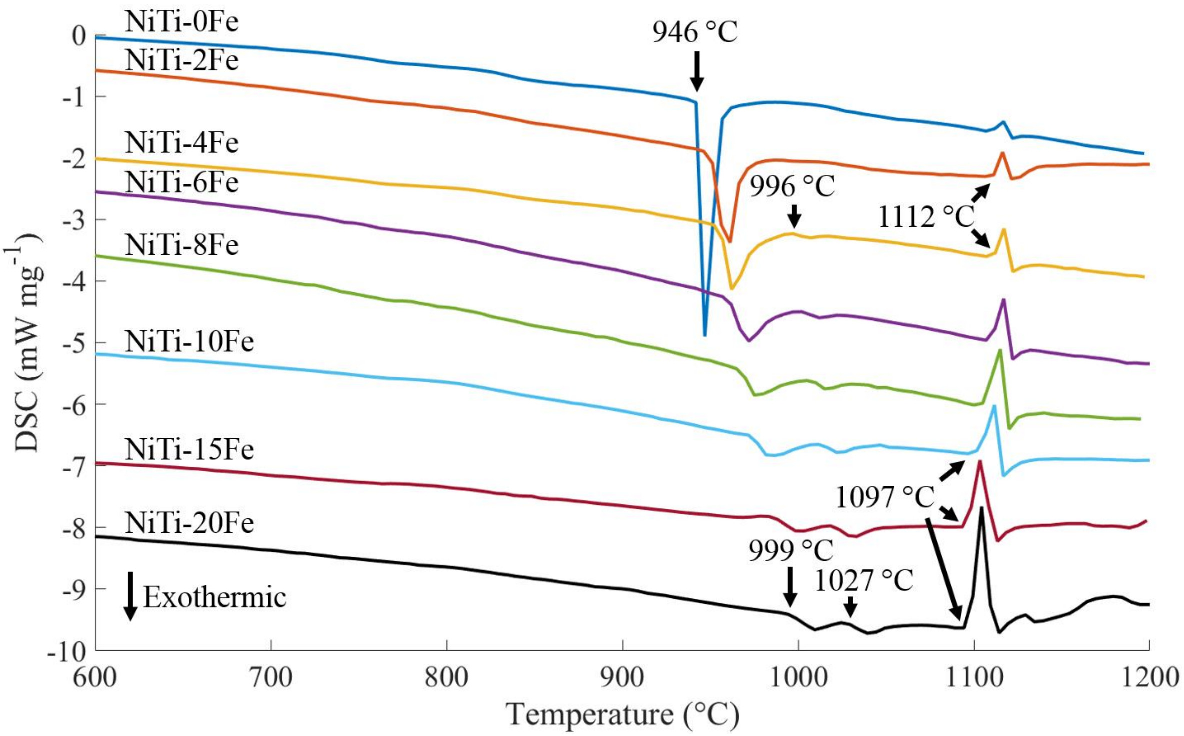

Figure 15. Part of the DSC heating curves for samples containing 0-20 at.% Fe.

The DSC curves for each composition and their respective interruption temperatures are presented in Appendix I – DSC.

3.2. SEM and EDS Results

3.2.1. SEM Results

Figure 16 shows how the porosity in the samples increases as the sintering time and temperature is increased. In Figure 16 (a) the porosity is relatively low, in (b) after the exothermic event the porosity has increased and smaller pores have grown together to form larger ones. This trend continues in Figure 16 (c), here, after the combined endothermic and exothermic event, the pores have grown significantly. The size of the pores are approximately the same for the highest temperature in Figure 16 (d).

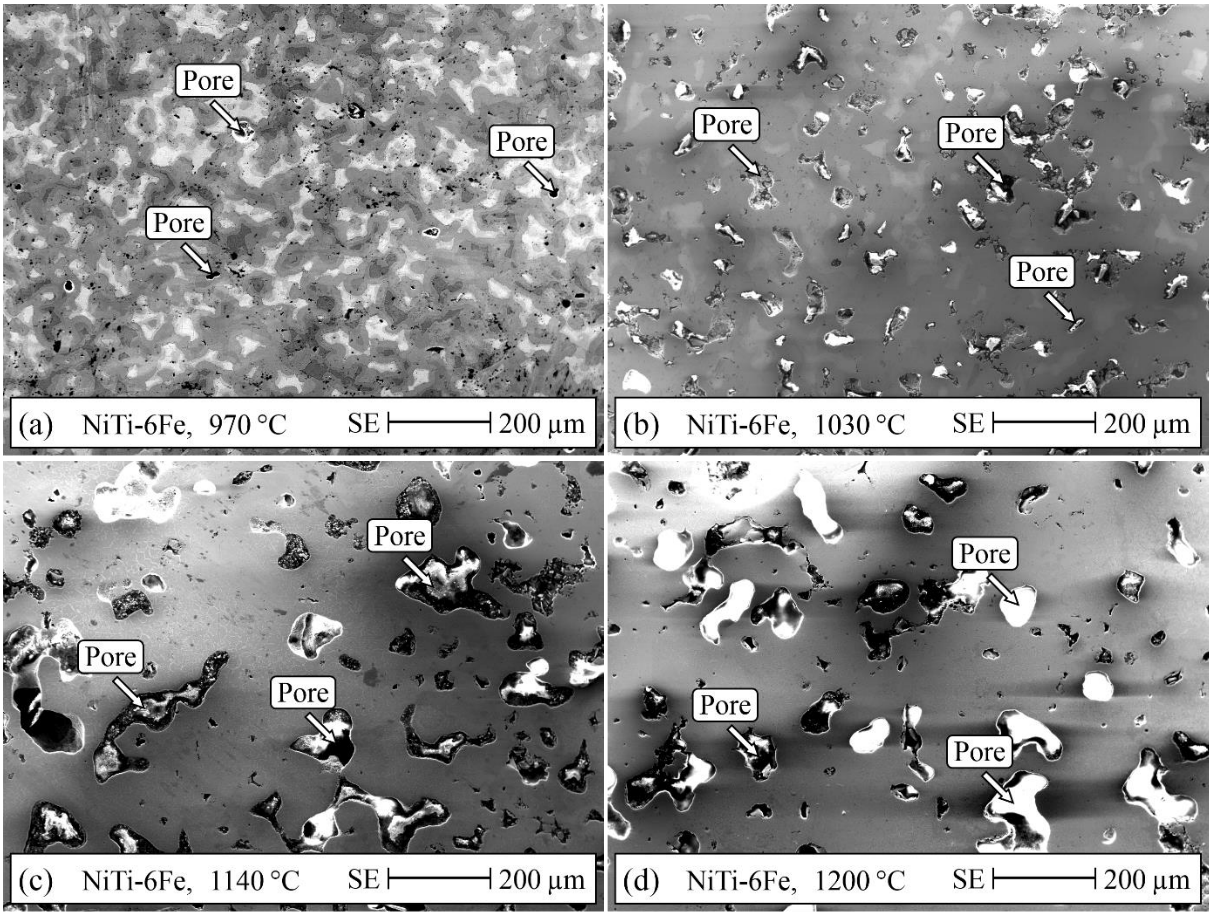

Figure 16. SEM images of the porosity evolving as the temperature is increased.

3.2.2. EDS Results

EDS results are presented in Appendix II – EDS. A BSE image, on which the investigated regions are marked, is presented together with a table over the recorded composition for each region.

3.3. XRD Results

The XRD patterns for the samples containing 0-10 at.% Fe heated to 1200 °C are shown in Figure 17. They all have their largest peak at 42.5°, and it corresponds to NiTi. The relative intensity of the peak at 44.5°, identified as belonging to iron, varies the most between the samples. The largest changes in the patterns occur between the NiTi-0Fe and NiTi-2Fe samples, because of the introduction of iron; and between the NiTi-6Fe and NiTi-8Fe samples, where several of the smaller peaks disappear.

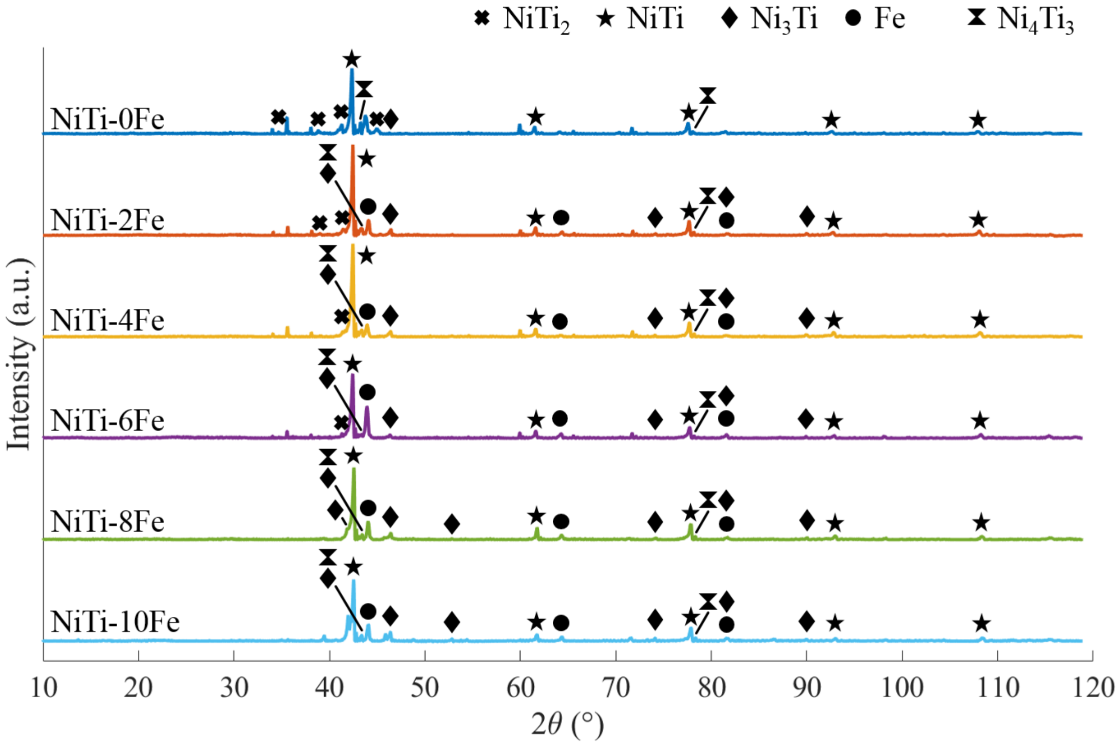

Figure 17. XRD patterns for the samples containing 0-10 at.% Fe, heated to 1200 °C. For more detailed patterns see Appendix III – XRD.

Individual XRD patterns, with labelled peaks, for all the investigated samples are presented in Appendix III – XRD. The XRD database did not have any entries for the (Fe,Ni)Ti and (Fe,Ni)Ti_2 compounds. Because of the comparatively low amount of iron to nickel in these compounds their XRD peaks were identified as belonging to NiTi and $NiTi_2$, respectively, by the analysis program Match!, and are presented as such in Figure 17, 32, 36 and 37, as well as in Appendix III – XRD.

4. Discussion

4.1. Binary systems

In order to understand the results from the ternary Ni-Ti-Fe system, the three binary systems were also investigated using DSC. The endothermic and exothermic events found in these three systems gave an indication of from which binary system the events found in the ternary Ni-Ti-Fe originated.

The DSC curve for the NiTi-0Fe sample, Figure 13, shows three features of interest, the first is the broad endothermic peak between 770 °C and 850 °C. The second is the exothermic peak that occurs at 946-953 °C, and the third feature is the combined endothermic and exothermic peak at 1111-1131 °C. The endothermic peak between 770 °C and 850 °C is attributed to the allotropic transformation of α-Ti to β-Ti, which occurs at 767 °C according to the Ni-Ti phase diagram. The large exothermic peak originates from the reaction of the liquid formed during the eutectic melting of β-Ti and NiTi, which occurs at 942 °C, according to the Ni-Ti phase diagram in Figure 1. The combined peak is connected to another eutectic melting, the $NiTi + Ni_3Ti \rightarrow L$, at 1118 °C. The endothermic part of the peak is the melting of these two intermetallic compounds, and the exothermic part is the reaction of the liquid [28].

Of the four binary systems: Ni-10Fe, Ni-50Fe, Ti-10Fe and Ti-50Fe, only the last one have any clear peaks recorded by the differential scanning calorimeter, see Figure 14, This combined endothermic and exothermic peak has an onset at 1091 °C. According to the Ti-Fe phase diagram in Figure 5, this should be the eutectic melting, and subsequent reaction, of the mixture between TiFe and β-Ti. For Ti-10Fe, the iron is assumed to dissolve in the titanium rather than form any intermetallic compound. Thus the TiFe + β-Ti → L reaction cannot occur and give rise to a peak as seen for Ti-50Fe. There is however a small and broad endothermic peak around 838 °C that could match the allotropic transformation of α-Ti to β-Ti. For Ni-10Fe and Ni-50Fe, the DSC curves show no indication of any reactions taking place. This is in good agreement with the Ni-Fe phase diagram in Figure 4, which shows how nickel and iron form a solid solution for the majority of the studied temperature interval.

4.2. Ternary systems

The amount of iron added to the equiatomic Ni-Ti clearly has an effect on the shape of the DSC curves, see Figure 15. There are four prominent changes to the shape of the NiTi-0Fe curve (Figure 13) as the amount of iron is increased. The first is that the exothermic peak, which for NiTi-0Fe has an onset temperature of 946 °C, becomes less exothermic. The second change is that the exothermic peak shifts its onset to higher temperatures, and the third is that the peak splits into two parts. The fourth change concerns the combined endothermic and exothermic peak, which for NiTi-0Fe exists at 1111-1131 °C; it becomes more endothermic as the iron content is increased. The onset of this peak shifts around slightly, but does not follow any discernible pattern. The broad endothermic peak between 770 °C and 850 °C that is attributed to the α-Ti → β-Ti allotropic transformation is present for all compositions.

4.2.1. Samples Heated to 1200 °C

Samples of all compositions were heated to 1200 °C. The individual DSC curves for the NiTi-0Fe, NiTi-6Fe, NiTi-10Fe, NiTi-15Fe and NiTi-20Fe samples can be seen in Figure 13, 19, 20, 29 and 30 respectively. For the NiTi-2Fe, NiTi-4Fe and NiTi-8Fe samples the DSC curves are presented in Appendix I - 1, 2 and 5, respectively.

The microstructure at 1200 °C for the samples containing 0-10 at.% Fe is very similar. The porosity is high, as can be seen in the representative SE image in Figure 18 (a). In addition to the large pores there are also much smaller round pores scattered across the sample, see Figure 18 (b). BSE images show that all samples heated to 1200 °C have a grey background that is interspersed with small darker and brighter areas, see Appendix II - 1 and Figure 18 (d). The background was determined by EDS to be NiTi (Appendix II - 2). This was supported by the XRD patterns in Figure 17, all compositions had their highest peak at 42.5°, this peak belongs to NiTi, as does the peaks at 61.7°, 77.7°, 92.8° and 108.2°. The NiTi was, for all compositions, rich in nickel. The dark regions present in the microstructure form mostly irregular spots and are rich in titanium, with a trend of lower nickel content for higher amounts of iron. They are gathered mostly around the pores, see Figure 18 (c). The brighter areas are rich in nickel and come in two shapes resembling needles and grain boundaries. The EDS analysis (Appendix II - 2) of the grey spots, needles and grain boundaries showed that the grey spots consistently contained the most iron of the phases, at each composition. Most often, the grain boundaries contained the least iron, and were richer in nickel than the needles. Thus, iron seems to have a stronger tendency to dissolve into the titanium than into the nickel. However, the variance of iron content in the different phases was small and iron does not appear to strongly favour one phase above another.

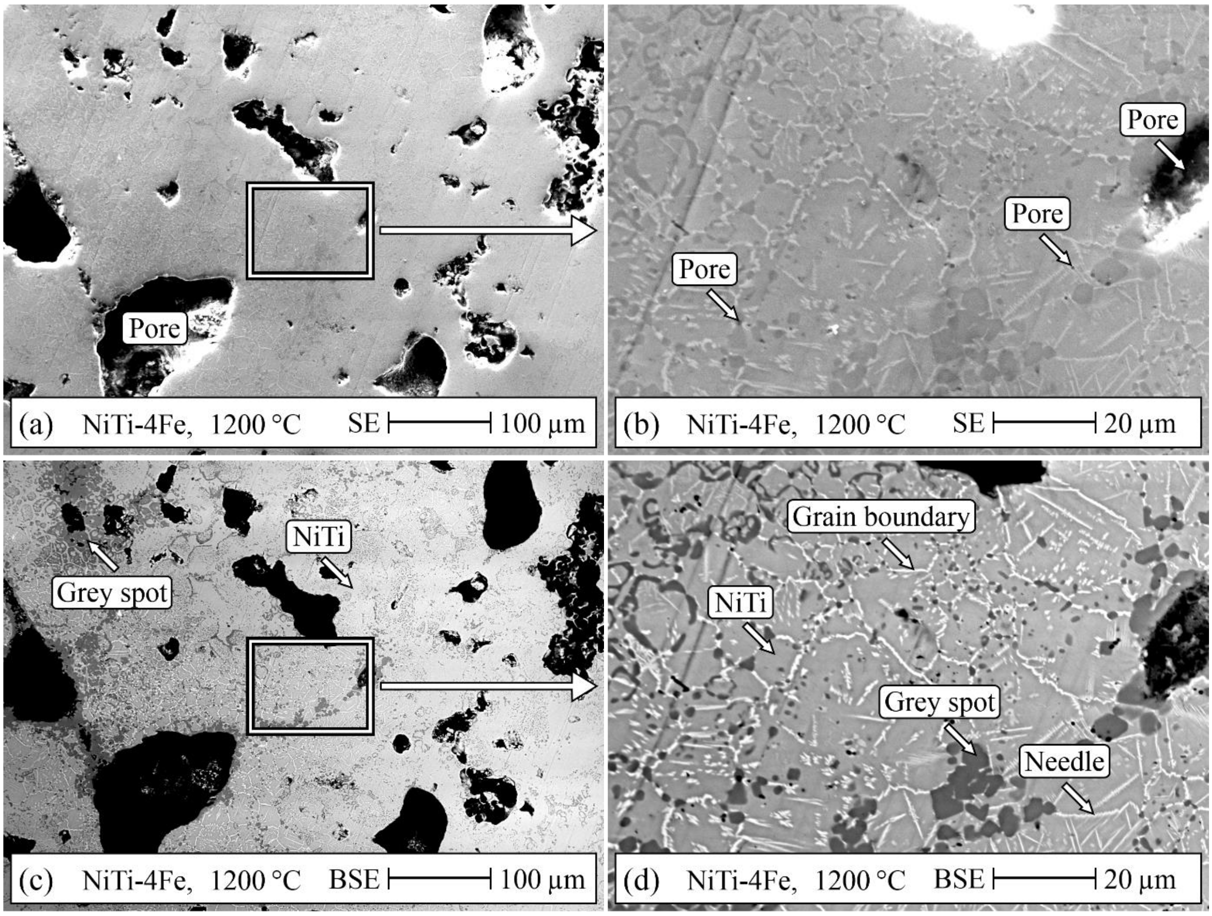

Figure 18. SE and BSE images at two magnifications, of NiTi-4Fe heated to 1200 °C.

The individual XRD patterns, for the samples containing 0-10 at.% Fe heated to 1200 °C, can be found in Appendix III - 1, 2, 3, 8, 9 and 17. As mentioned, they identify the presence of NiTi in all samples. In addition to this phase, the XRD analysis showed the presence of $NiTi_2$, Ni_3Ti, Ni_4Ti_3 and iron. The $NiTi_2$ is present for low iron contents, up to 6 at.% Fe. Ni_3Ti and Ni_4Ti_3 are present for all compositions, as is iron, with the natural exception of the NiTi-0Fe sample. As the composition given by the EDS for the grey spots does not match $NiTi_2$, they are assumed to be a mixture of $NiTi_2$ and NiTi with iron substituting some of the nickel. Similarly the needles and grain boundaries does not contain enough nickel to be Ni_3Ti. Their compositions do occasionally fall very close to the metastable Ni_4Ti_3. For some samples this is true if the iron is assumed to act as a substitute for nickel, and for some if the iron is simply assumed to be dissolved in the Ni_4Ti_3. Nonetheless, both the needles and grain boundaries appear to be some kind of mixture between NiTi, Ni_3Ti and Ni_4Ti_3, with the grain boundaries being the more Ni-rich of the two.

Returning to the XRD patterns in Figure 17, they showed the presence of small amounts of $NiTi_2$ for samples containing up to 6 at.% Fe. Since $NiTi_2$ is not stable at 1200 °C, and should have melted at 984 °C, it is surprising to find it among these samples. However, it is completely possible for a compound to exist outside of its stability range. According to the XRD patterns, the relative amount of Ni_3Ti increased with increasing iron content, supporting the belief that iron and nickel are largely interchangeable in the Ni-Ti-Fe system. It should also be noted that no iron-based intermetallic compounds was found among the samples. However, the $NiTi_2$ and NiTi found in the binary Ni-Ti system do appear to become $(Fe,Ni)Ti_2$ and (Fe,Ni)Ti, respectively, as iron is added to the system. Further, as the iron content increases, the ratio between nickel and titanium in NiTi grows closer to being equiatomic. However, the overall effect is that the (Fe,Ni):Ti ratio moves further from 1:1.

4.2.2. Samples containing 6 and 10 at.% Fe

In order to determine why the peaks on the DSC curves changes when iron is added to the system, samples containing 6 at.% and 10 at.% Fe were investigated further. NiTi-6Fe was chosen because it was the composition with the lowest amount of iron that clearly showed the splitting of the first exothermic peak. NiTi-10Fe was chosen since it contained the highest amount of iron that allowed investigation of the samples heated to temperatures after the combined endothermic and exothermic peak. The NiTi-6Fe and NiTi-10Fe samples were studied by means of heating the sample discs to temperatures of interest, determined by the DSC curves, see Figure 19 and Figure 20, respectively. The temperatures the NiTi-6Fe and NiTi-10Fe samples were heated to, were given in Table 4. They can be divided into four groups; the first consists of the temperatures before the exothermic peak (900 °C, 960 °C and 970 °C). The second contains one temperature between the two parts of the split peak (1000 °C). The third group is the temperatures between the exothermic peak and the end of the combined endothermic and exothermic peak (1030 °C, 1060 °C, 1110 °C and 1115 °C). The fourth and final group contains the temperatures after the combined peak (1140 °C, 1150 °C and 1200 °C).

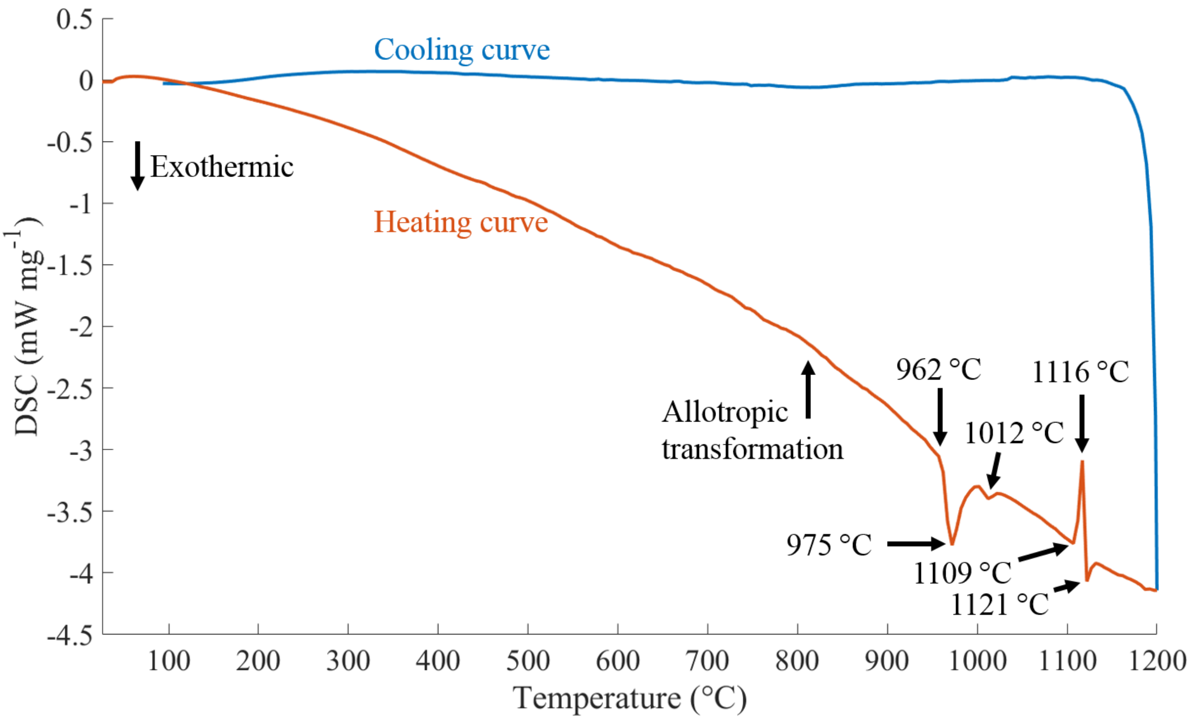

Figure 19. DSC curve for NiTi-6Fe heated to 1200 °C.

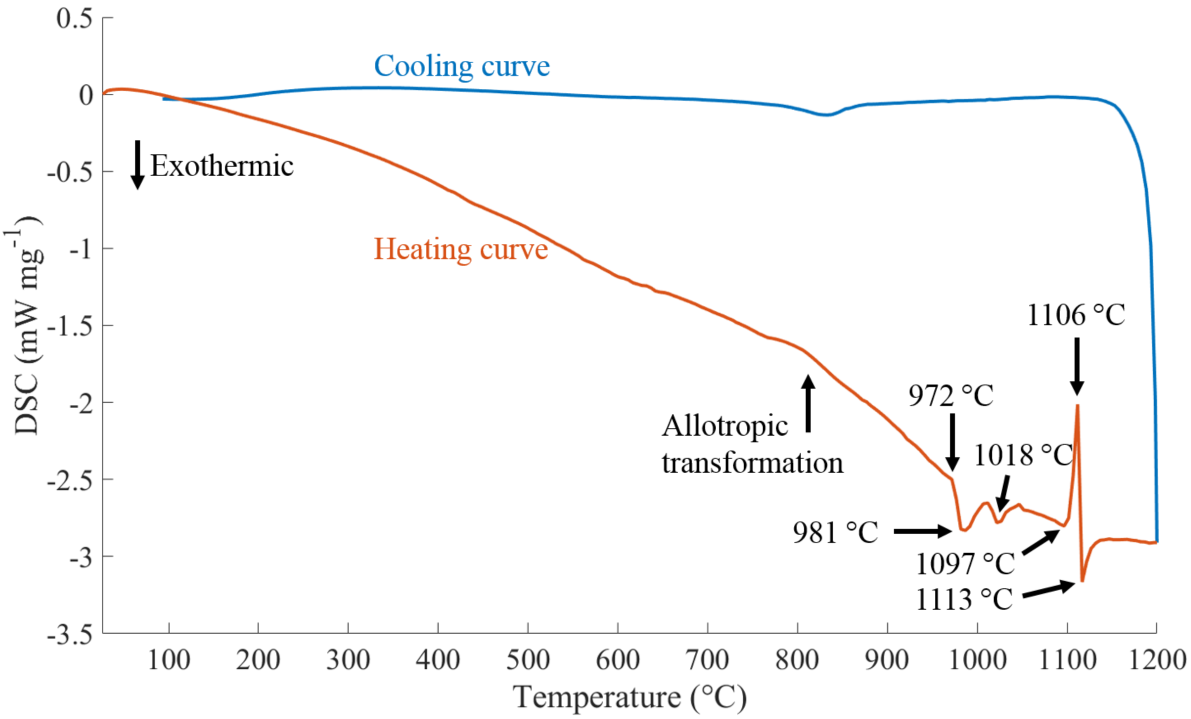

Figure 20. DSC curve for NiTi-10Fe heated to 1200 °C.

900 to 970 °C

The DSC curves for the NiTi-6Fe samples heated to 900 °C and 970 °C are presented in Appendix I - 3. For the NiTi-10Fe samples heated to 900 °C and 960 °C the DSC curves are found in Appendix I - 6. The heating curves for the four samples are very similar; the only variance is that the beginning of the exothermic peak is present for the NiTi-6Fe sample heated to 970 °C.

The microstructure of these samples contains plenty of small pores, see Figure 21 (a) and (b). Several phase regions can be distinguished in Figure 21 (c) and (d), see also Appendix II - 3 (a) and Appendix II - 5 (a) and (b). There are five distinct shades of grey visible, the EDS analysis of both the NiTi-6Fe and the NiTi-10Fe samples (Appendix II - 4 and Appendix II - 6, respectively) provided the compositions of these regions. The darkest areas were determined to be nearly pure titanium, while the brightest regions were nearly pure nickel. Between them were the remaining three shades of grey, ranging from the darkest found around the titanium particles, to the brightest around the nickel particles. The region closest to the titanium particles was determined to be $NiTi_2$, the area closest to the nickel particles were Ni_3Ti, and between them were NiTi. The compositions given by the EDS analysis for the three intermetallic compounds only slightly deviate from the stoichiometry if iron is seen as a substituent to nickel. The titanium, $NiTi_2$, NiTi, Ni_3Ti and nickel was also identified by the XRD, along with the iron. The individual XRD patterns from these samples can be found in Appendix III - 4, 10 and 11.

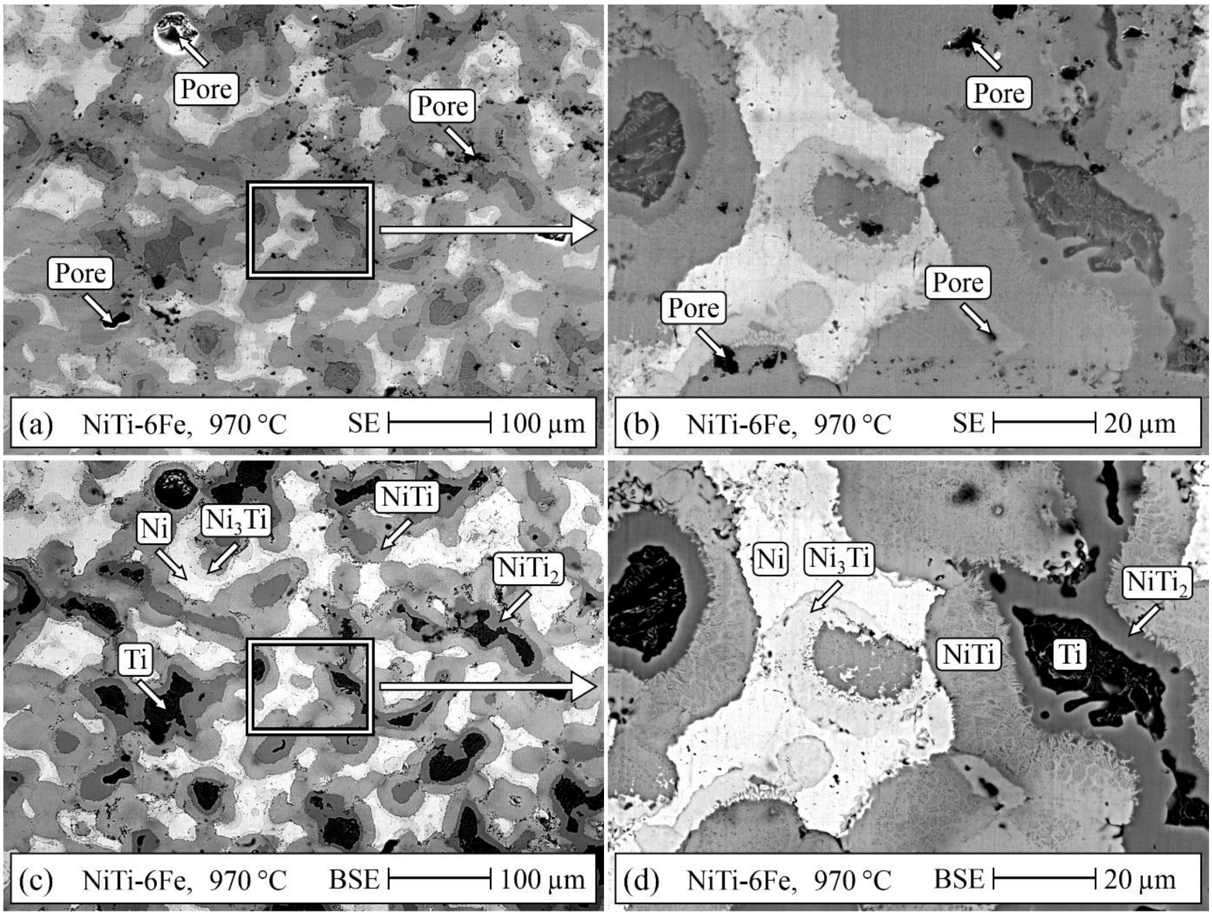

Figure 21. SE and BSE images at two magnifications, of NiTi-6Fe heated to 970 °C.

Consistently for the samples at these lower temperatures, the regions of high purity nickel were larger than the regions of high purity titanium, see Figure 21 (c). The brightest and darkest regions are the original nickel and titanium particles that have not yet formed intermetallic compounds through solid-state diffusion. Since the particle size of these two elements were originally similar, the smaller size of the titanium region indicates that nickel diffuses into titanium to a higher degree than titanium diffuses into nickel, resulting in larger cores of pure nickel. This is supported by the relative intensity of the XRD peaks of nickel compared to those of titanium, as the former are clearly larger than the latter. The regions of Ti-rich compounds are also larger than the areas of the Ni-rich compounds. Additionally the titanium cores contain larger amounts of nickel, compared to the amounts of titanium in the nickel cores, see Appendix II - 4 and 6. From the XRD patterns (Appendix III - 4, 10 and 11) it can also be seen that the relative intensity of the nickel and titanium peaks decrease as the temperature is increased, mainly $NiTi_2$ and NiTi grows at the expense of these two elements.

EDS mapping, of the region in Figure 21 (b) and (d), shows the uneven distribution of all three elements at these temperatures, the positions of the original particles can still be distinguished, see Figure 22. The nickel and titanium maps (Figure 22 (b) and (c), respectively) are complementary, the bright areas in the nickel map are dark in the titanium map, and vice versa. The iron is mainly concentrated in two small regions along the bottom of Figure 22 (d). The corresponding areas in Figure 22 (a) are different shades of grey. The Fe-rich region on the left is the same shade as the surrounding nickel and the region on the right has a similar grey shade as the surrounding NiTi. It is therefore difficult to visually distinguish a Fe-rich region from an area with low iron content. In Figure 22 it can also be seen that the iron content in the Ni_3Ti regions is lower than in the other intermetallic phases.

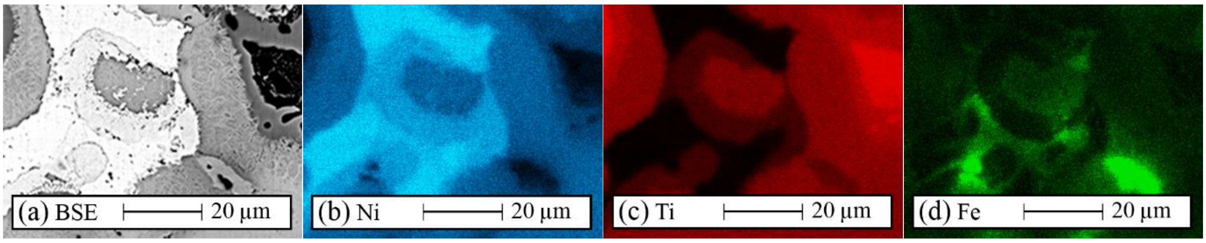

Figure 22. EDS mapping of an area in the NiTi-6Fe sample heated to 970 °C, (a) shows the BSE image, and (b), (c) and (d) show the distribution of nickel, titanium and iron, respectively.

1000 °C

The two DSC curves, for the NiTi-6Fe and NiTi-10Fe samples heated to 1000 °C, can be found in Appendix I - 3 and 6, respectively. They show their difference in onset temperature for the exothermic peak. For NiTi-6Fe the onset is 962 °C, and for NiTi-10Fe it is 972 °C.

There are two major microstructural changes occurring in the samples during the first part of the exothermic peak. The first is an increase in porosity. The pores are mainly forming in the regions that are riches in titanium. This indicates that the titanium was involved in the reaction responsible for the first part of the exothermic peak. The second change is a decrease in size of the regions of nickel and titanium, see Figure 23 (a) and (c), and Appendix II - 5 (c). According to the EDS analysis (Appendix II - 6) the purity of the nickel and titanium is also decreasing, that of the titanium more rapidly than that of nickel. The EDS analysis identified Ni_3Ti, NiTi and $NiTi_2$ as being present in the sample in addition to the nickel and titanium. The XRD results are not in complete agreement with the EDS results, the XRD did not detect any titanium in the sample. One possible explanation for this discrepancy is that there was simply not sufficient amounts of unreacted titanium to give peaks high enough to be identified in the XRD pattern. Compared to the XRD patterns for lower temperatures the peak with the highest relative intensity is now clearly that which belongs to NiTi, which shows that this phase grows at the expense of the others.

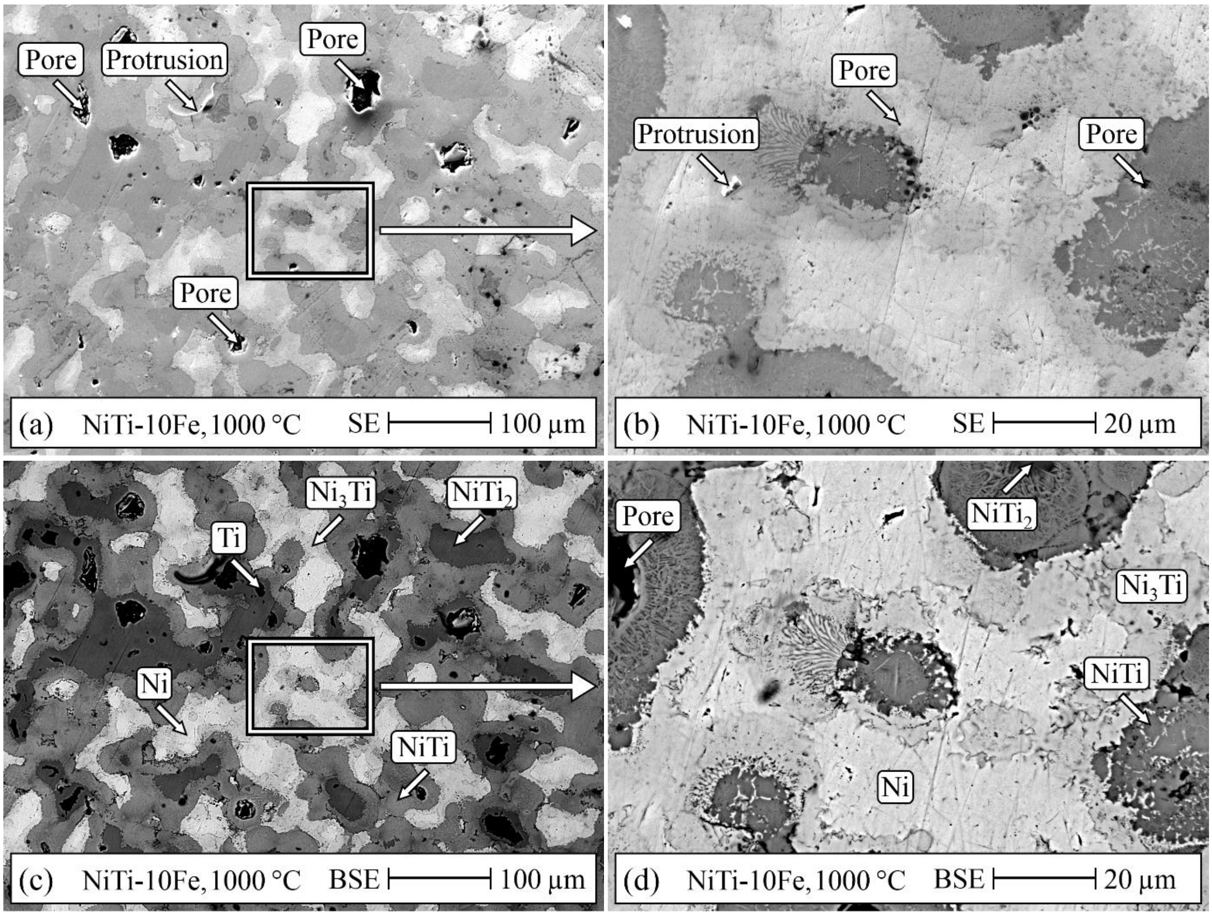

Figure 23. SE and BSE images at two magnifications, of NiTi-10Fe heated to 1000 °C.

There is still a significant amount of $NiTi_2$ present in the sample, according to both the EDS and the XRD results, even though $NiTi_2$ has a melting point of 984 °C, see Figure 1. The isothermal section at 1000 °C of the ternary Ni-Ti-Fe phase diagram in Figure 7 does however show $NiTi_2$ as stable at this temperature if it contains slightly less than 30 at.% Fe and a few atomic percent of nickel. But that is not the composition of the phase according to the EDS results, these would place the composition in the (Fe,Ni)Ti + L two-phase region in the isothermal section of the phase diagram in Figure 7. Since there is no exothermic peak on the DSC cooling curve, see Appendix I - 6, it is unlikely that there was any liquid present that would then have solidified when the sample was cooled down. So either the $NiTi_2$ is existing outside of its stability range due to kinetic limitations, or $NiTi_2$ is stable at this temperature due to it being a solid solution of $NiTi_2$ and Ti_2Fe, which is stable in a broader region than indicated in Figure 7.

Figure 24 shows the EDS mapping of an area in the NiTi-10Fe sample heated to 1000 °C, it looks similar to the EDS mapping of NiTi-6Fe heated to 970 °C in Figure 22. The nickel and titanium maps (Figure 24 (b) and (c), respectively) are still complimentary. Bright areas in the nickel map are dark in the titanium map, and vice versa. The iron, in Figure 24 (d) is no longer as concentrated, but still appears to be less dissolved in the Ni_3Ti than the other two intermetallic compounds. Once more, the Fe-rich areas cannot be distinguished by only looking at the BSE image in Figure 24 (a).

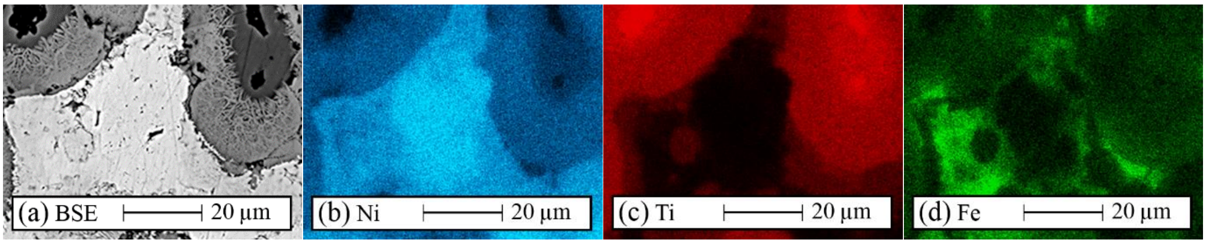

Figure 24. EDS mapping of an area in the NiTi-10Fe sample heated to 1000 °C, (a) shows the BSE image, and (b), (c) and (d) show the distribution of nickel, titanium and iron, respectively.

1030 to 1115 °C

In the temperature range between the end of the first exothermic peak and the end of the combined endothermic and exothermic peak, samples of the NiTi-6Fe composition were heated to 1030 °C and to 1115 °C. The NiTi-10Fe samples were heated to 1030 °C, 1060 °C and to 1110 °C. The highest temperatures for each composition are interrupted in the combined peak. The DSC curves for the NiTi-6Fe and NiTi-10Fe samples heated to 1030 °C are found in Appendix I - 3 and Appendix I - 6, respectively. The remaining three can be seen in Appendix I - 4 and Appendix I - 7 for the NiTi-6Fe and NiTi-10Fe samples, respectively. The overall shape of the curves is similar for all five samples. The main differences are the onset temperatures for the two parts of the exothermic peak. For the NiTi-6Fe samples the onsets are at 962 °C and 1004 °C, while for the NiTi-10Fe samples the temperatures are higher, 972 °C and 1009 °C. The size of the two parts of the exothermic peak becomes more equal with higher iron content.

The microstructure of these samples is much more porous, see Figure 25 (a), but otherwise less varied compared to the samples heated to lower temperatures. The EDS analysis (Appendix II - 4 and 6) indicates that there are fewer phases present, no unreacted titanium was identified. NiTi is the dominant matrix phase, in addition to it, there are both darker and larger, brighter areas distinguishable, see Figure 25 (c) and (d), as well as Appendix II - 3 (b) and (c), and Appendix II - 5 (d), (e) and (f). According to the EDS analysis, the darker areas are Ti-rich with a composition close to that of $NiTi_2$. This phase is present for temperatures up to the combined endothermic and exothermic peak. Then the $NiTi_2$ presumably starts morphing into the grey spots found at higher temperatures, as this is the only other Ti-rich phase found at higher temperatures. The grey spots appear to be a mixture of $NiTi_2$ and NiTi according to the EDS and XRD results. Thus no pure $NiTi_2$ is present for neither the NiTi-6Fe sample heated to 1115 °C, nor the NiTi-10Fe sample heated to 1110 °C. The brighter areas in the microstructure are much larger than the dark areas. At the lower temperatures in this group the samples still contain cores of unreacted nickel, but as the temperature is increased, more titanium and iron is able to diffuse into the nickel. By the time the combined endothermic and exothermic peak is reached the bright regions are made up of Ni_3Ti, according to the EDS analysis.

The NiTi-10Fe sample heated to 1110 °C shows a different microstructure compared to the other samples in this group, see Appendix II - 5 (f). It appears the Ni_3Ti regions start to break up during the end of the combined peak, as this sample is interrupted after the endothermic part of the peak and the NiTi-6Fe sample heated to the beginning of the endothermic part (1115 °C) did not show the same broken up structure. In the same image the other two Ni-rich structures, the needles and grain boundaries, are also found. Thin bright lines similar to the grain boundaries are also found among the other four samples in this group, see Appendix II - 3 (b) and (c), as well as Appendix II - 5 (d) and (e). These are however too thin to be able to obtain any reliable EDS data, as the area probed will extend beyond the limits of the phase. Thus the composition of these very thin grain boundaries is unknown, but presumably it is similar to that of the grain boundaries.

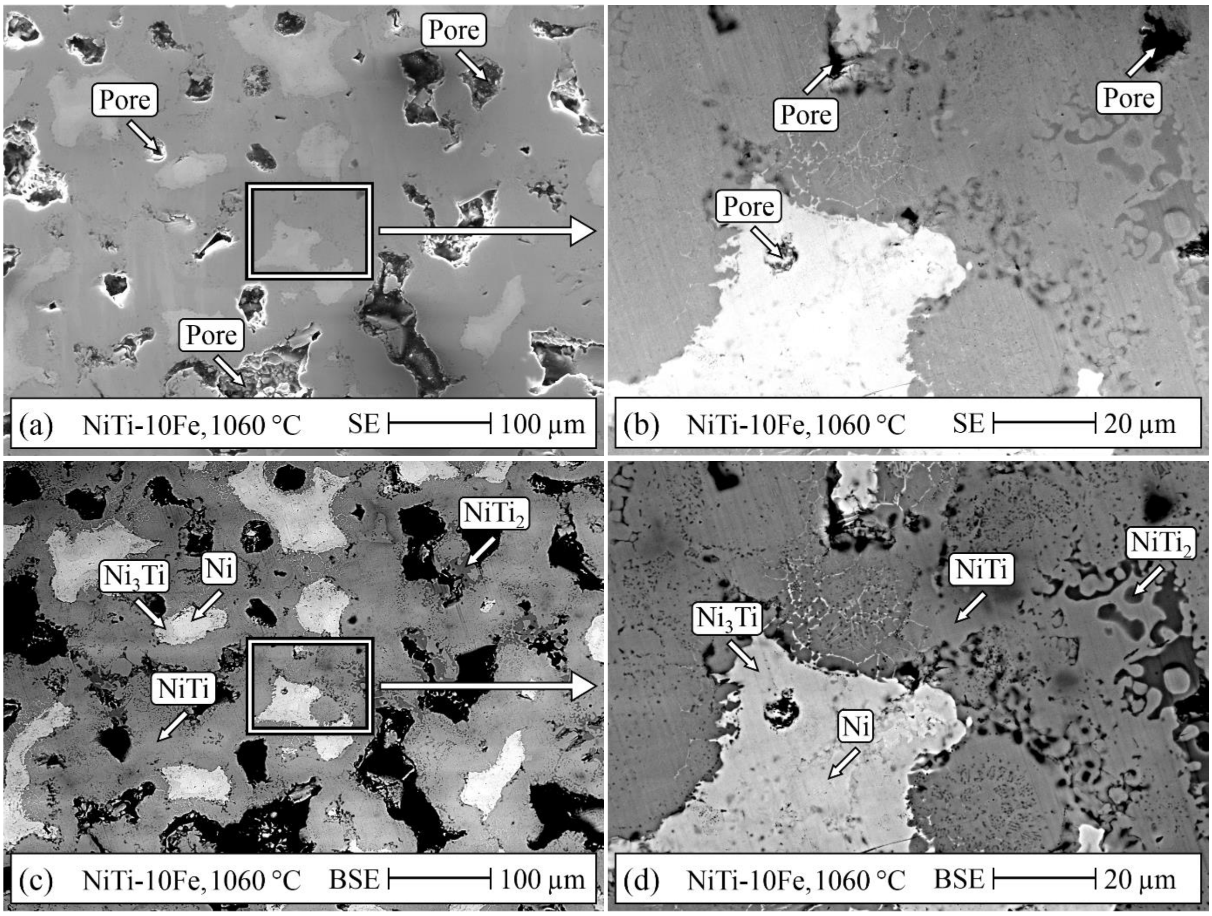

Figure 25. SE and BSE images at two magnifications, of NiTi-10Fe heated to 1060 °C.

The presence of the $NiTi_2$, NiTi and Ni_3Ti phases are confirmed by the XRD analysis for all five samples, along with the iron. The individual XRD patterns for the five samples in this group are found in Appendix III - 5, 6, 13, 14 and 15. Nickel was also detected by the XRD for the samples heated to 1030 °C and 1060 °C. Starting from the NiTi-10Fe sample heated to 1060 °C the XRD also detected the metastable phase Ni_4Ti_3, in the samples heated to higher temperatures.

EDS mapping of part of the area depicted in Figure 25 (b) is shown in Figure 26. Once more the nickel map and the titanium map (Figure 26 (b) and (c), respectively) are complimentary. But the intensity of the regions are much more uniform compared to the intensity at lower temperatures. In Figure 26 (a) the Fe-rich areas among the NiTi can actually be distinguished. The iron map in Figure 26 (d) shows that the iron still tends to dissolve less in the Ni_3Ti than the other phases, even though the contrast between the phases is not as sharp anymore.

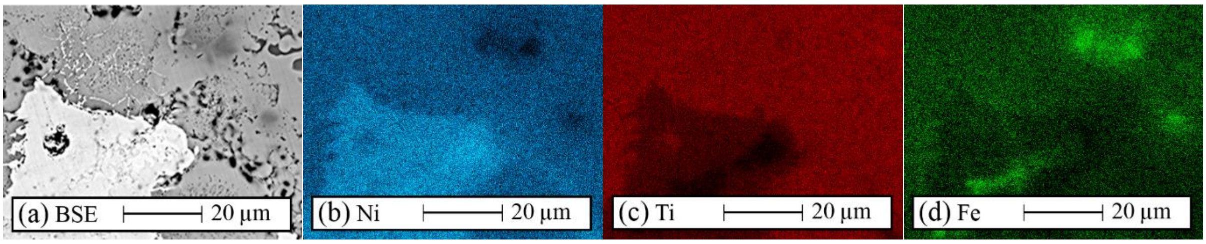

Figure 26. EDS mapping of an area in the NiTi-10Fe sample heated to 1060 °C, (a) shows the BSE image, and (b), (c) and (d) show the distribution of nickel, titanium and iron, respectively.

1140 to 1200 °C

DSC curves for the NiTi-6Fe samples heated to 1140 °C and 1200 °C are shown in Appendix I - 4, and the DSC curves for the NiTi-10Fe samples heated to 1150 °C and 1200 °C are presented in Appendix I - 7. Apart from the different onset temperatures, the shape of the curves for the NiTi-6Fe samples are similar to those for the NiTi-10Fe samples. For the NiTi-6Fe sample heated to 1200 °C the relative size of the two parts of the exothermic peak differs from the samples heated to lower temperatures. So in this specific regard the NiTi-6Fe sample heated to 1200 °C is considered an outlier.

The microstructure of the NiTi-6Fe and NiTi-10Fe samples heated to 1140 °C and 1150 °C, respectively, are presented in Figure 27 as well as Appendix II - 3 (d) and Appendix II - 5 (g). For the samples heated to 1200 °C the microstructure is shown in Appendix II - 1 (d) and (f), for the NiTi-6Fe and NiTi-10Fe samples, respectively. At these high temperatures the samples show a pronounced difference in the microstructure compared to the samples heated to lower temperatures. This new microstructure was seen beginning to form in the NiTi-10Fe sample heated to 1110 °C (Appendix II - 5 (f)). The large bright regions of Ni_3Ti have disappeared in favour of the formation of small Ni-rich structures that resemble the so called grain boundaries found in the samples heated to 1200 °C, see Figure 18 and Appendix II - 1. The needles found in the samples heated to 1200 °C have also begun to emerge, but to a smaller extent than the grain boundary structures. The dark Ti-rich regions have decreased somewhat in size and are mainly located in vicinity of the pores. The compositions of the grey spots, needles and grain boundaries can be found in Appendix II - 2, 4 and 6, along with the composition of the main phase, the NiTi. Additionally, the porosity has increased a lot due to the melting and subsequent reaction of the melt that occurs during the combined endothermic and exothermic peak.

The XRD analysis identified NiTi, Ni_3Ti, iron and the metastable phase Ni_4Ti_3 among all samples in this group. In addition to them, $NiTi_2$ was also identified in both of the NiTi-6Fe samples. The individual XRD patterns can be found in Appendix III - 7, 8, 16 and 17. The relative intensity of the Ni_3Ti peaks is higher in the NiTi-10Fe samples. It appears that as iron is added to the system the overall composition of the samples shifts further towards the Ni-rich side. Since iron is able to replace nickel in both $NiTi_2$ and in NiTi, forming $(Fe,Ni)Ti_2$ and (Fe,Ni)Ti, respectively, this leaves more nickel to form Ni_3Ti and Ni_4Ti_3. Thus it is reasonable to find a higher Ni_3Ti peak in the NiTi-10Fe sample than in the NiTi-6Fe sample. The origin of the combined endothermic and exothermic peak was determined to be the $NiTi + Ni_3Ti \rightarrow L$ reaction. The increasing size of the endothermic part of the peak, as the iron content increases, is probably due to the higher availability of Ni_3Ti, since NiTi seems to be the most prominent phase. When the liquid formed then reacts with the other phases during the exothermic part of the combined peak it will most likely form a mixture of Ni-rich phases and produce the needles and grain boundaries.

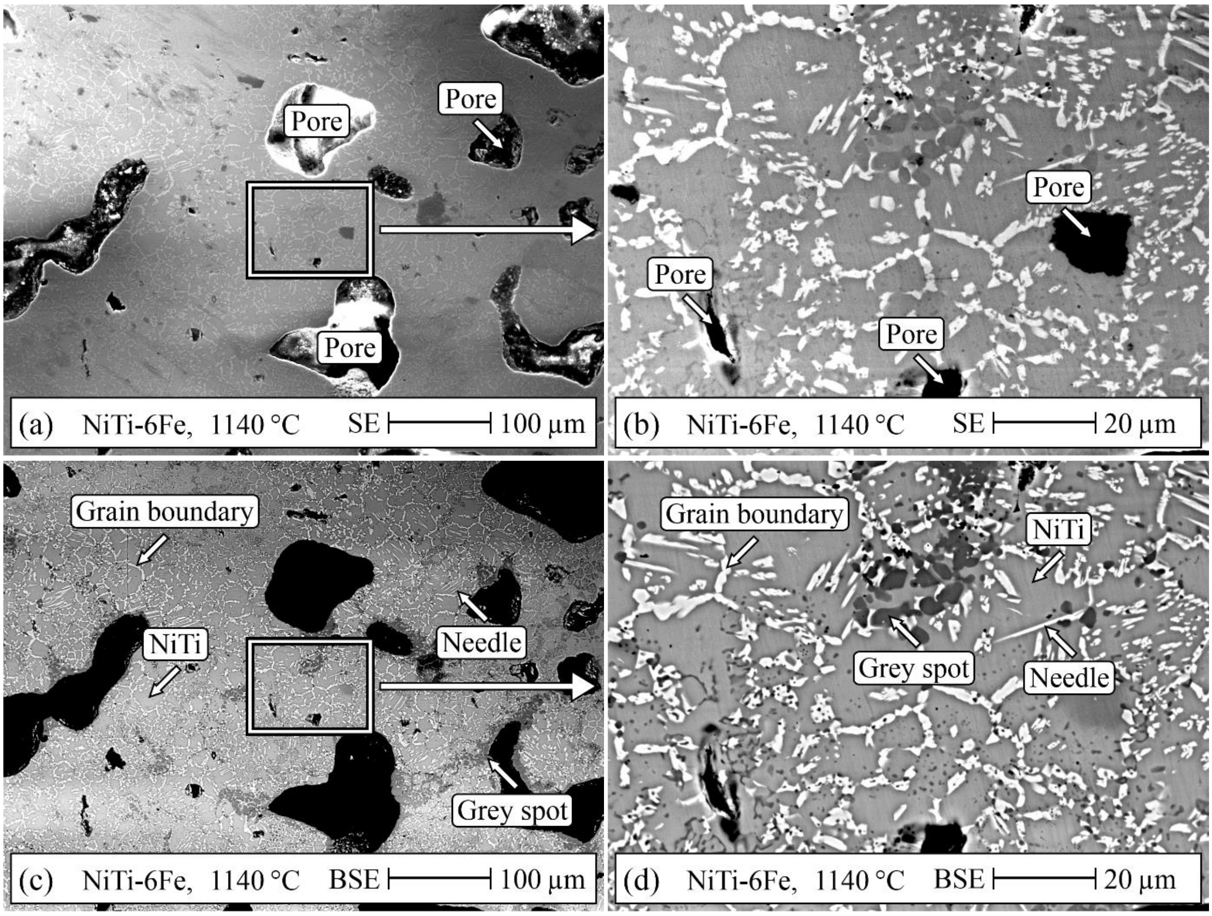

Figure 27. SE and BSE images at two magnifications, of NiTi-6Fe heated to 1140 °C.

The EDS maps at these high temperatures are highly uniform, see Figure 28. It is barely possible to distinguish the brighter and darker regions in Figure 28 (a) from the nickel and titanium maps in Figure 28 (b) and (c). The iron map in Figure 28 (d) shows that the iron is evenly distributed throughout the sample.

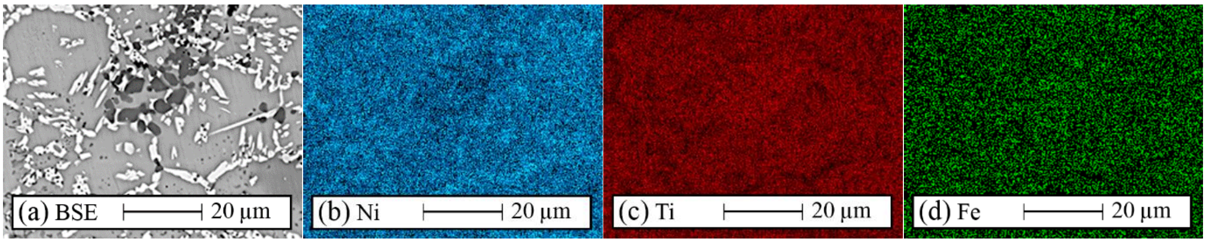

Figure 28. EDS mapping of an area in the NiTi-6Fe sample heated to 1140 °C, (a) shows the BSE image, and (b), (c) and (d) show the distribution of nickel, titanium and iron, respectively.

4.2.3. Samples containing 15 and 20 at.% Fe

The DSC curves for the NiTi-15Fe and NiTi-20Fe samples in Figure 29 and 30, respectively, both show the split exothermic peak and the combined endothermic and exothermic peak. The onset temperatures for the two parts of the exothermic peak are 987 °C and 1021 °C for the NiTi-15Fe sample, and 999 °C and 1027 °C for the NiTi-20Fe sample. The endothermic part of the combined peak starts at 1097 °C during the heating process for both samples. The DSC heating curve for the NiTi-15Fe sample looks mostly familiar after the combined peak, but just before the onset of the split exothermic peak there is a small endothermic peak. This peak is ostensibly the $\beta\text{-Ti} + (\text{Fe,Ni})\text{Ti}_2 \rightarrow \text{L}$ melting, as the first part of the exothermic peak is understood to be the reaction of the melt formed in this melting process. The cooling curve for the NiTi-15Fe sample exhibits a prominent exothermic peak around 804 °C that is thought to be connected to the allotropic transformation of Fe. The DSC cooling curve for the NiTi-20Fe sample has a sharp exothermic peak around 1096 °C that lines up nicely with the large endothermic peak on the heating curve. These two peaks indicate that the melt, formed in the (Fe,Ni)Ti + Ni_3Ti → L reaction connected to the endothermic part of the combined peak, does not react completely during the exothermic part of the peak. Thus, some of the melt is left over and solidifies during the cooling. The origin of the peaks between 1120 °C and 1200 °C, on both the heating and the cooling curve for the NiTi-20Fe sample, has not been determined.

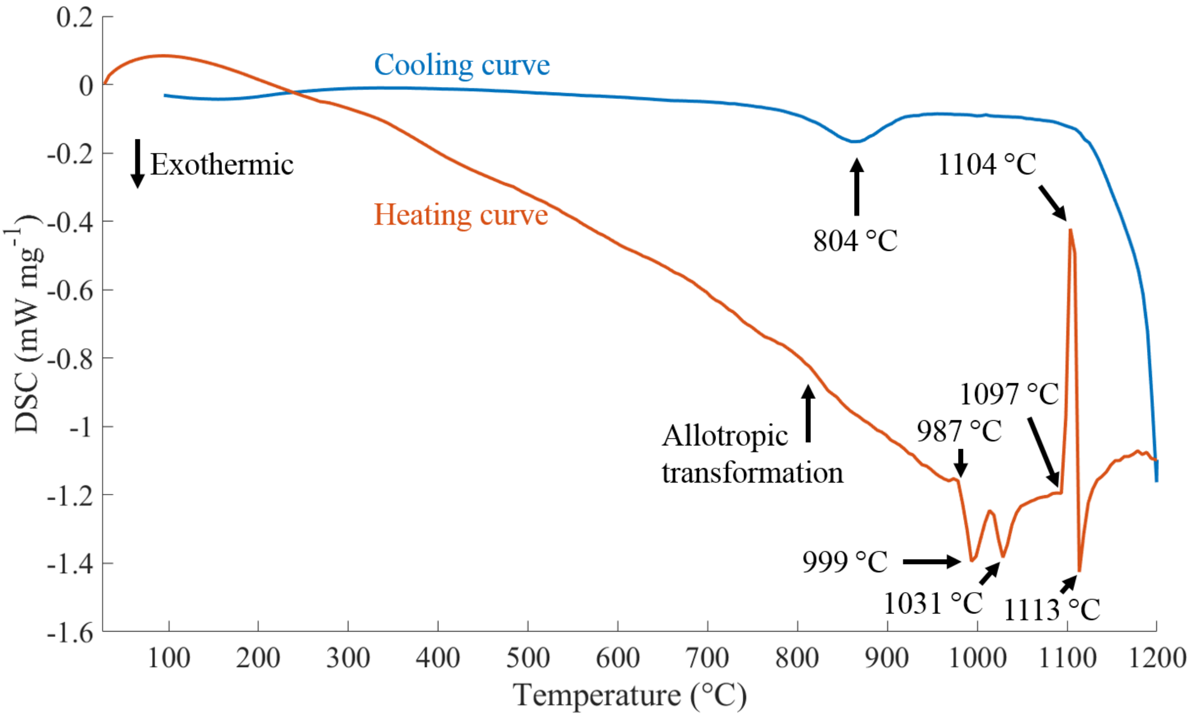

Figure 29. DSC curve for NiTi-15Fe heated to 1200 °C.

When the crucibles containing the NiTi-15Fe and NiTi-20Fe sample discs were removed from the differential scanning calorimeter, the melting process indicated by the DSC curve was evident since the discs had lost their original shape and melted across the bottom of the crucible. The samples could not be removed from their crucibles. For this reason, the NiTi-15Fe and NiTi-20Fe samples heated to 1200 °C were not analysed by SEM, EDS or XRD. Instead, these compositions were heated to 1090 °C, interrupting the heating before the onset of the endothermic peak to avoid the melting. These samples were then studied using SEM, EDS and XRD.

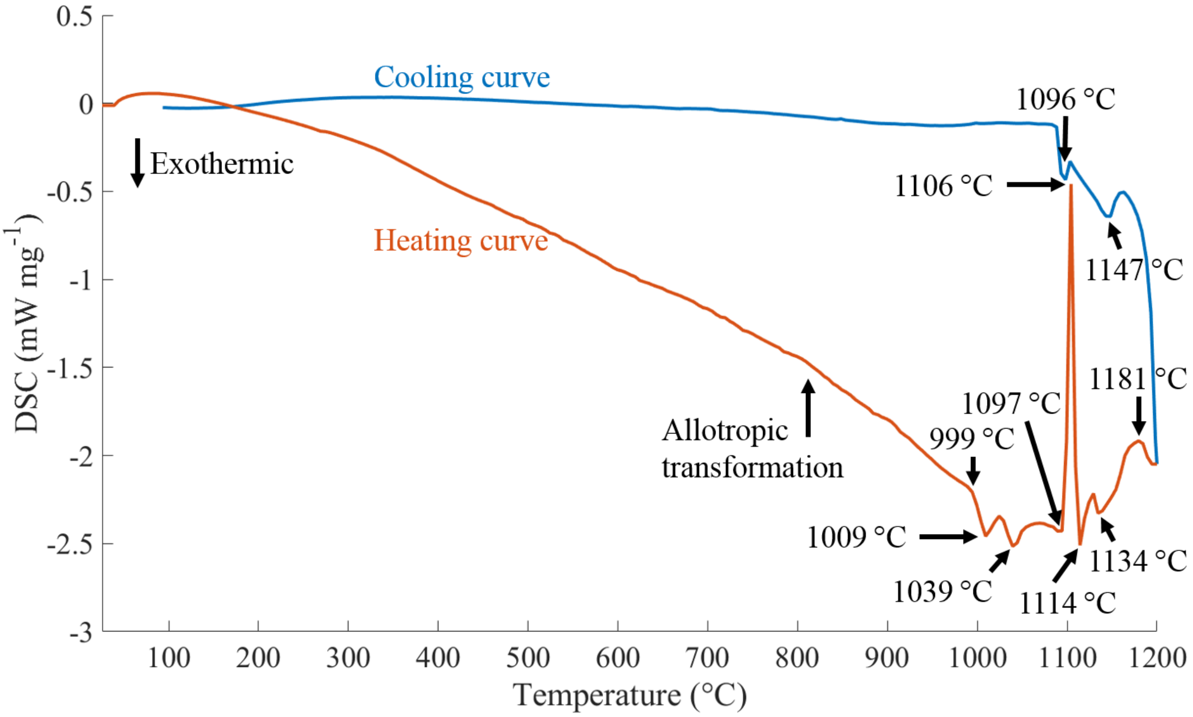

Figure 30. DSC curve for NiTi-20Fe heated to 1200 °C.

A consequence of only being able to analyse the NiTi-15Fe and NiTi-20Fe samples at lower temperatures is that the shape of the DSC curve for NiTi-20Fe between 1120 °C and 1200 °C, see Figure 30, could not be explained. The shape of both the heating and cooling curve between these temperatures differs from samples with lower iron content. Some indication of this shape is present in the NiTi-15Fe samples. The phases involved in creating these peaks could not be determined. However, there appears to be both an exothermic event occurring around 1134 °C and an endothermic event around 1181 °C. The uncertainty, as to whether they are actually exothermic and endothermic, respectively, stems from the difficulties in determining where the baseline lies. But the belief that the event around 1181 °C is endothermic is supported by the matching exothermic peak on the cooling curve at 1147 °C. Presumably some intermetallic compound, or combination of compounds, melts during the endothermic peak and then solidifies during cooling, creating the exothermic peak.

The microstructure of the NiTi-15Fe and NiTi-20Fe samples heated to 1090 °C can be seen in Figure 31 and in Appendix II - 7. The porosity in Figure 31 (a) is similar to that found in the group of samples heated to between 1030 °C and 1115 °C. Several regions can be seen in Figure 31 (c) and (d). The estimated composition of the different regions are presented in Appendix II - 8. The identified phases are Ni_3Ti and NiTi, for both samples. Additionally the NiTi-15Fe sample contained the Ni-rich structures resembling needles and grain boundaries. The NiTi-20Fe sample contained unreacted nickel and titanium, as well as $NiTi_2$. The overall look of the NiTi-15Fe and NiTi-20Fe samples resemble the NiTi-6Fe and NiTi-10Fe samples at similar temperatures, but with larger regions of Ni-rich phases for higher iron contents.

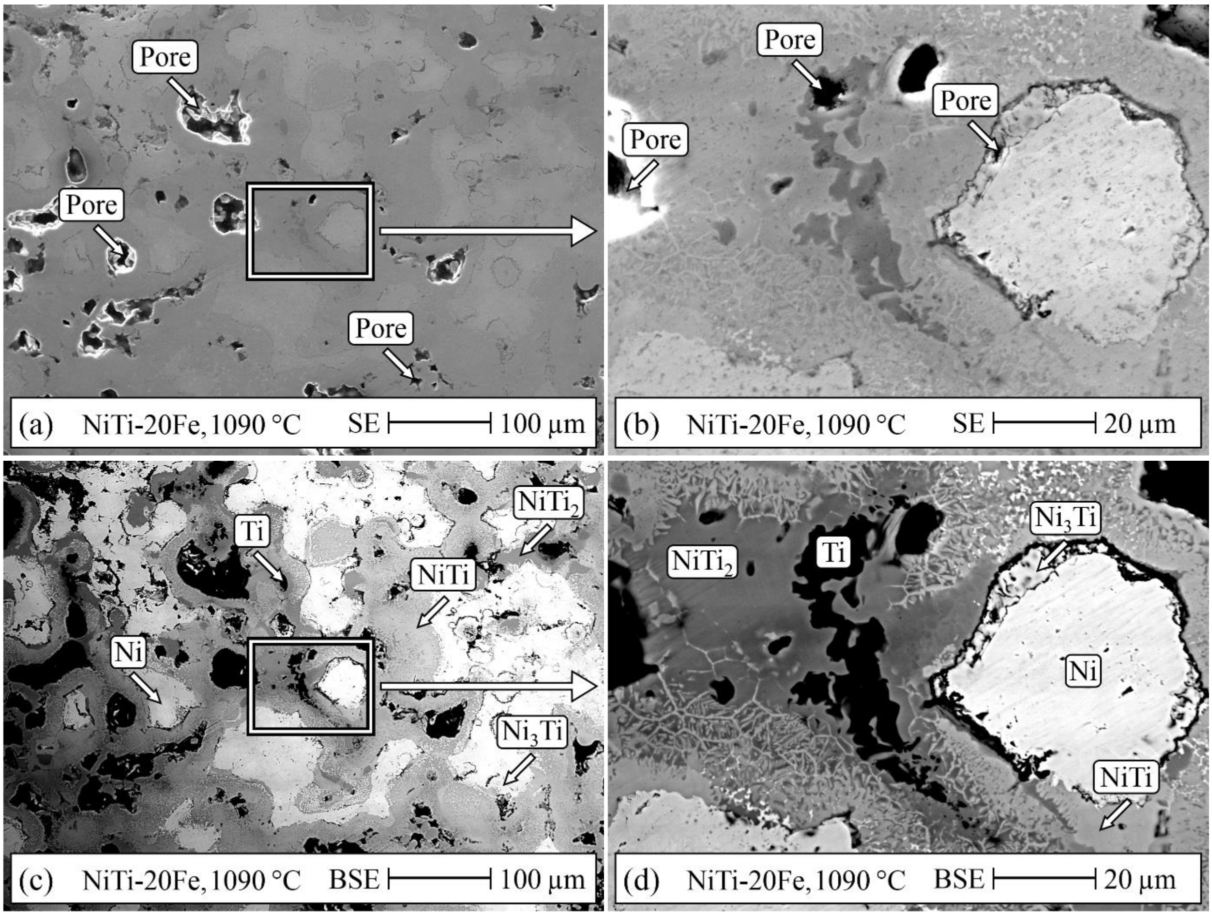

Figure 31. SE and BSE images at two magnifications, of NiTi-20Fe heated to 1090 °C.

An unusual number of the points measured by the EDS were excluded from the data presented in Appendix II - 8, as they did not match the composition of the region they were thought to belong to, according to the visual information given by the BSE image. A few of the Fe-rich regions may have consisted of iron based intermetallic compounds. However the XRD patterns did not match any such compounds, see Appendix III - 18 and 19, or Figure 32. The compounds identified by the XRD analysis were, $NiTi_2$, NiTi, Ni_3Ti and iron for both samples. These XRD results are not in good agreement with the EDS results, as no Ti-rich phase was found by the EDS in the NiTi-15Fe sample and the EDS found both unreacted nickel and unreacted titanium in the NiTi-20Fe sample. The lack of an identified Ti-rich phase in the NiTi-15Fe sample is probably not because it does not exist in the sample, but rather that it was not present in the areas investigated by EDS. A possible explanation for the lack of titanium and nickel peaks in the XRD pattern for NiTi-20Fe, see Appendix III - 19, is that the sample did not contain large enough amounts of unreacted nickel and titanium for them to be distinguishable in the XRD pattern. As can be seen in Figure 32 the relative amounts of Ni_3Ti in these samples are higher than for the samples with lower iron content (Appendix III – XRD). The amount of Ni_3Ti present before the combined endothermic and exothermic peak does also appear to increase with increasing iron content. Since NiTi is the most common phase at all of the higher temperatures, then an increase in Ni_3Ti would allow for a larger $(Fe,Ni)Ti + Ni_3Ti \rightarrow L$ reaction, resulting in a larger endothermic peak as the iron content is increased.

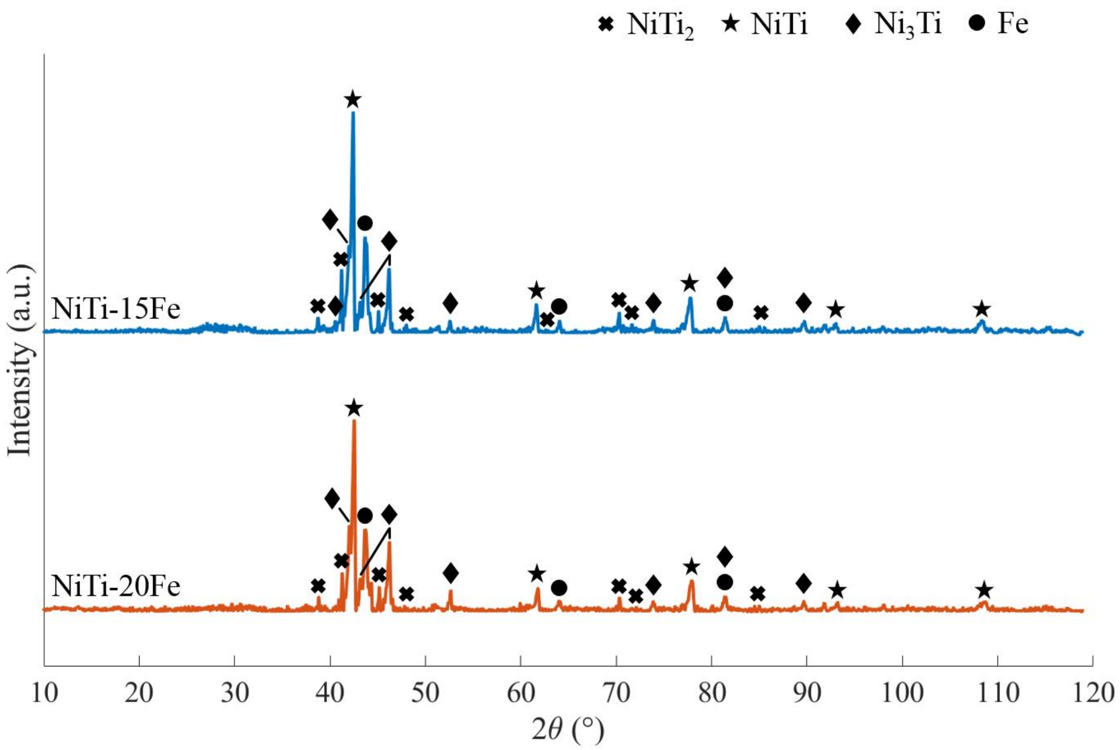

Figure 32. XRD patterns for NiTi-15Fe and NiTi-20Fe heated to 1090 °C.

The EDS mapping of the area in Figure 31 (b) is shown in Figure 33. The nickel and titanium maps are in Figure 31 (b) and (c), respectively, are complementary in that the dark regions in the nickel map are bright in the titanium map. The iron map in Figure 31 (d) shows that less iron is present in the unreacted nickel and titanium compared to the surrounding phases. In addition, the amount of iron in the Ni_3Ti region is lower than in $NiTi_2$ or NiTi. A few areas contain a higher concentration of iron and is probably the remains of the original iron particles. It is once more difficult to distinguish the Fe-rich regions by looking at the BSE image in Figure 31 (a).

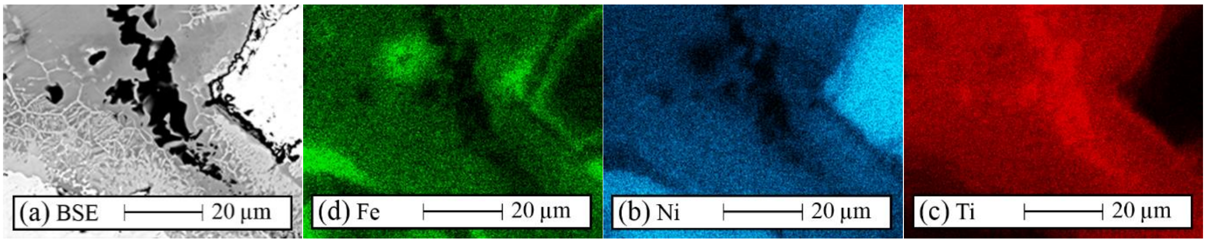

Figure 33. EDS mapping of an area in the NiTi-20Fe sample heated to 1090 °C, (a) shows the BSE image, and (b), (c) and (d) show the distribution of nickel, titanium and iron, respectively.

4.3. Cooling Curves

A majority of the cooling curves did not show any features, see Appendix I – DSC. Typical examples of the exceptions are collected in Figure 34. They can be divided into three groups, the first consisting of samples exhibiting a broad exothermic peak somewhere between 780 °C and 930 °C. The second group has a sharp exothermic peak around 1103 °C. The third and final group consists of samples with an exothermic peak between 640 °C and 700 °C. In addition to these there are also the NiTi-15Fe and NiTi-20Fe samples, they have multiple peaks on their cooling curves.

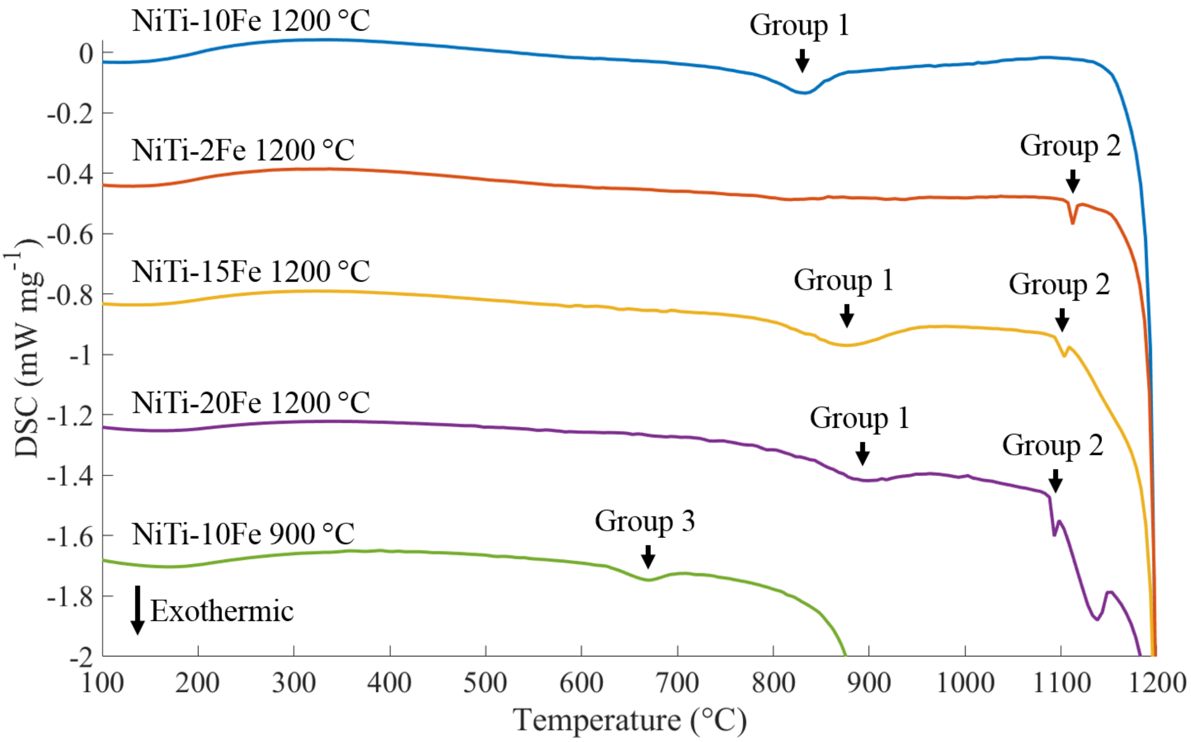

Figure 34. DSC cooling curves showing the features found among them.

The first group, with the broad exothermic peak between 780 °C and 930 °C, consists of samples with higher iron content. The peak first appears for the NiTi-8Fe sample and then also makes appearances among the NiTi-10Fe, NiTi-15Fe and NiTi-20Fe samples. It only shows up for samples heated to temperatures after the combined endothermic and exothermic peak. The temperature interval it exists for, together with the fact that it only appears for higher iron contents indicates that this peak could be connected to the allotropic transformation of iron. The γ-Fe → α-Fe transformation takes place at 912 °C, according to the binary phase diagrams in Figure 4 and Figure 5. However, the heating curve did not show a corresponding endothermic peak, but that could be because it got lost among the reactions connected to the first exothermic peak.

The sharp peak of the samples in the second group is connected to the combined endothermic and exothermic peak that shows up on the heating curve. The endothermic part of the combined peak sometimes resulted in this exothermic peak on the cooling curve, at approximately the same temperature as the endothermic one. This is because not all the melt that formed during the endothermic peak had an opportunity to react with the surrounding material. Thus the melt solidified during the cooling. This occurred for one NiTi-0Fe sample and for one NiTi-2Fe sample. For these samples the solidification peak was not present when the experiment was repeated, indicating that the melt would typically be able to react completely. A reason it had not done so could be due to inhomogeneity in the sample discs. This might cause a lot of liquid to form in one area and the liquid at the centre not having sufficient time to reach any material it could react with. The NiTi-15Fe and NiTi-20Fe samples also had these exothermic peaks on their cooling curves. The reason for these is presumably that a lot of material melted during the large endothermic peak, too much for all of it to be able to react before the sample was cooled down.

For the samples in the third group, they have the broad exothermic peak that occurs during cooling, between 640 °C and 700 °C. This peak only shows up for samples heated to temperatures below the onset of the first exothermic peak on the heating curve. Thus, the peak appeared for NiTi-6Fe heated to 900 °C and for NiTi-10Fe heated to both 900 °C and 960 °C. However, it did not appear for NiTi-6Fe heated to 970 °C as this sample was interrupted shortly after the onset of the exothermic peak. Another thing these samples have in common is that they still contain unreacted titanium, both according to the EDS and XRD analysis. The origin of this peak could thus be the allotropic transformation of β-Ti to α-Ti. The NiTi-6Fe sample heated to 970 °C did also contain titanium according to the EDS and XRD results, but the amount of unreacted titanium is less in this sample compared to the other three. The temperature range of this exothermic peak is lower than that of the broad endothermic peak on the heating curve (770-850 °C), which was determined to be the α-Ti → β-Ti allotropic transformation. The relative positions of these two peaks supports the idea that this peak originates from the β-Ti → α-Ti reaction.

4.4. Phase Evolution in Ni-Ti-Fe

Ni-Ti-Fe samples containing equiatomic amounts of nickel and titanium, and 0-20 at.% Fe, exhibited a phase evolution that was dependent on the iron content. The trends of the DSC curves produced by heating the samples from room temperature to 1200 °C, at a rate of 10 °C min^{-1}, and then immediately cooling them down to room temperature at the same rate, are presented in Figure 35. With increasing iron content the exothermic peak decreases in size, broadens, and splits into two peaks, the second part growing at the expense of the first, and the onset temperatures of both parts increase. The size of the endothermic peak also increases.

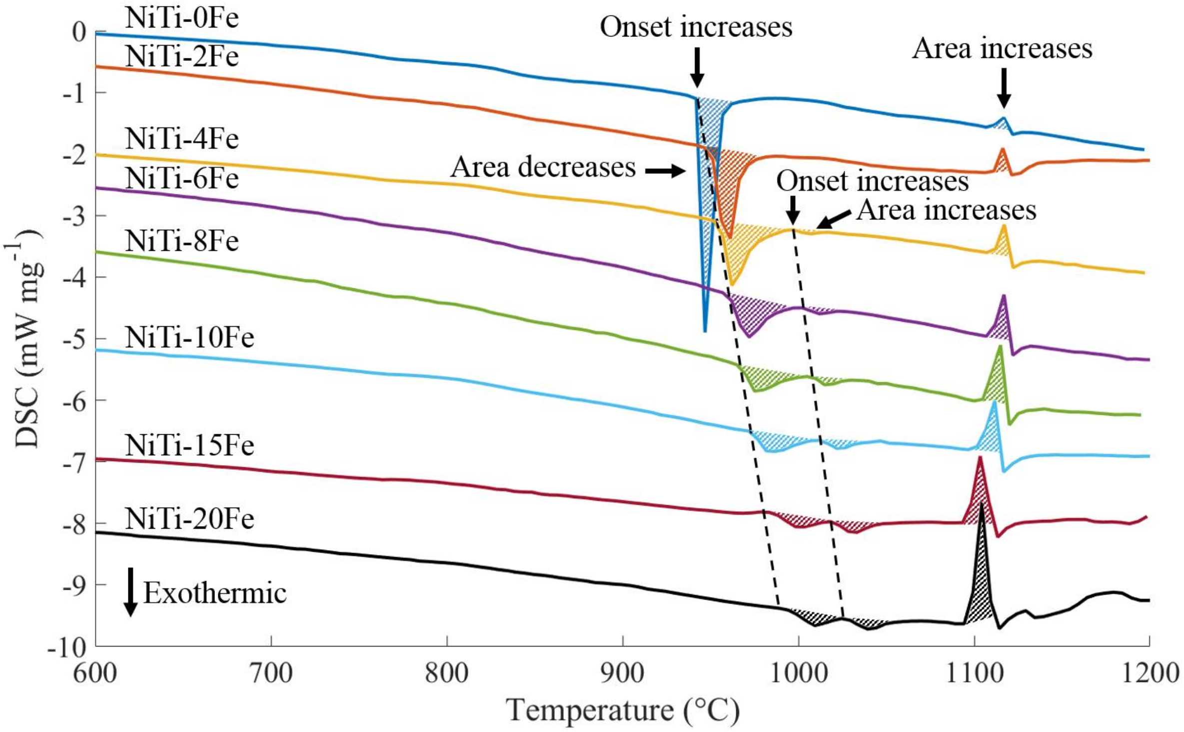

Figure 35. Trends in the DSC heating curves for 0-20 at.% Fe.

The resulting microstructures of the samples, presented in Appendix II - 1, show an increasingly strong presence of the Ni-rich structures resembling needles and grain boundaries, when the iron content is increased. In addition to them the microstructures also feature darker grey spots on a background of NiTi. Appendix II - 2 provides the results of the EDS analysis of these microstructures. If the regions labelled with NiTi in the microstructures are actually (Fe,Ni)Ti then the ratio of (Fe,Ni):Ti increases with increasing iron content. The EDS analysis of the needles, grain boundaries and grey spots is challenging since they are relatively small. When they are probed by the electron beam it is probable that the interaction volume encompasses more than the phase of interest. This would result in a composition that is a combination of, not only the structure in question, but also most likely (Fe,Ni)Ti. Therefore, the grey spots could actually be (Fe,Ni)Ti_2 and the needles and grain boundaries could be Ni_3Ti or Ni_4Ti_3.

The EDS analysis indicates that the $NiTi_2$ and NiTi phases were actually (Fe,Ni)Ti_2 and (Fe,Ni)Ti, respectively. However, the XRD database did not have any data for these solid solutions and the patterns for Fe-based compounds did not match the experimental patterns. Treating the (Fe,Ni)Ti_2 as $NiTi_2$ and the (Fe,Ni)Ti as NiTi when comparing the EDS and XRD results, then the general trends of these results are in good agreement. At the lowest investigated temperatures both unreacted nickel and titanium is present along with iron, $NiTi_2$, NiTi and Ni_3Ti, see Figure 36 and 37. The intermetallic compounds have formed through solid-state diffusional reactions. No unreacted titanium is left after the exothermic peak. The amount of unreacted nickel decreases significantly in connection to the first part of the exothermic peak and then gradually decreases so that it by the combined endothermic and exothermic peak is no longer present. $NiTi_2$ is clearly present up to the combined peak, thereafter very small amounts were detected by the XRD in the NiTi-6Fe samples, and the EDS identified the grey spots as Ti-rich phases in all samples. The NiTi is present for all compositions and temperatures. It is the main phase in all samples heated to 1000 °C or higher. Ni_3Ti is also present in all samples, but the relative amounts are not especially large but appear to be larger in the NiTi-10Fe samples than in the NiTi-6Fe samples, see Figure 36 and 37, or the corresponding XRD patterns in Appendix III – XRD. The metastable Ni_4Ti_3 appears for temperatures of 1060 °C and above for the XRD results, it is also around 1060 °C that the grain boundaries and needles start to develop in the microstructures.

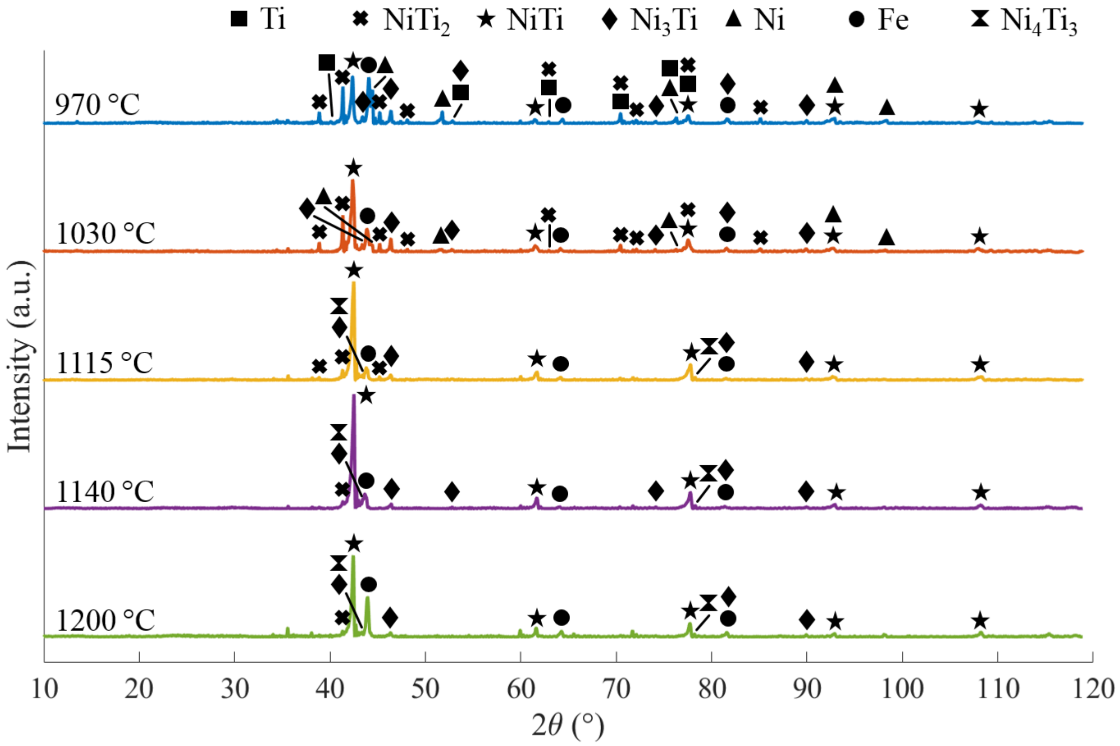

Figure 36. XRD patterns for the NiTi-6Fe samples.

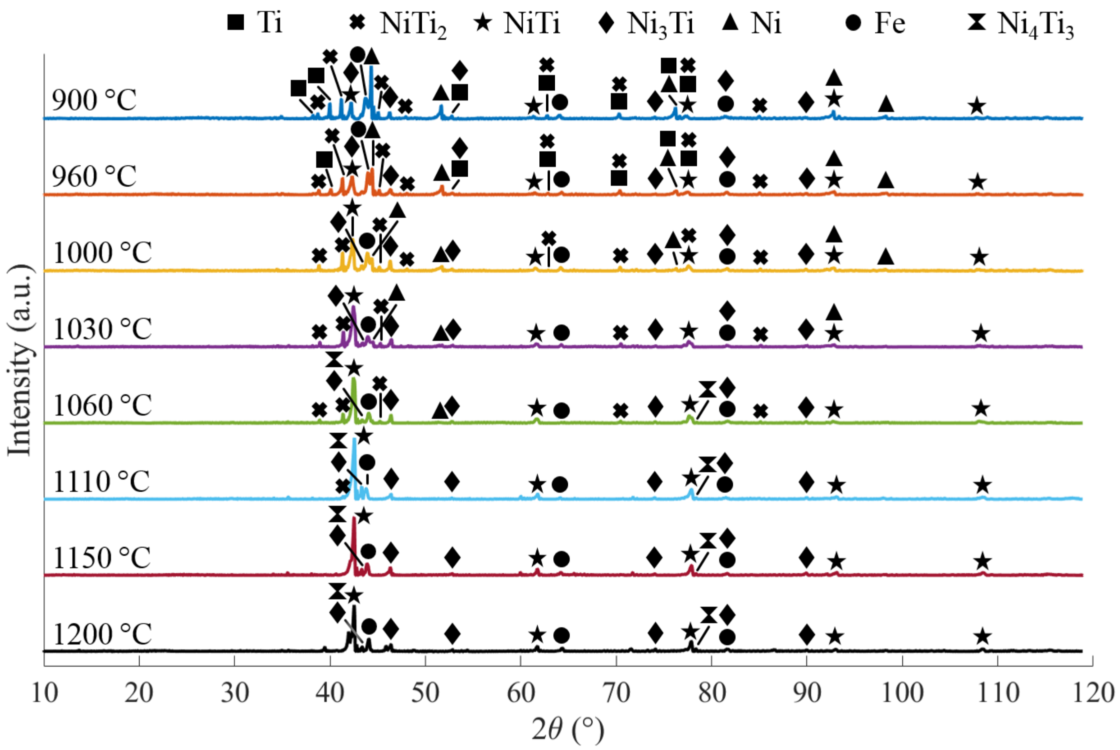

Figure 37. XRD patterns for the NiTi-10Fe samples.

From the binary Ni-Ti system, see Figure 13, the exothermic peak was determined to be connected to the β-Ti + NiTi$_2$ → L eutectic melting, and the combined endothermic and exothermic peak to the NiTi + Ni$_3$Ti → L reaction. The endothermic peak being the melting itself and the exothermic peaks being the reactions of the melts. The NiTi$_2$ → NiTi + L melting, if there is any NiTi$_2$ remaining, is assumed to occur within the large exothermic peak, as the heat created during it could increase the temperature of the sample above the melting temperature of NiTi$_2$. In the ternary Ni-Ti-Fe system the peaks are presumed to originate from the Ni-Ti binary system. With the addition of iron, the reactions are altered to β-Ti + (Fe,Ni)Ti$_2$ → L and (Fe,Ni)Ti$_2$ → (Fe,Ni)Ti + L. The splitting of the exothermic peak is believed to occur because, as less heat is released when the peak becomes smaller, the (Fe,Ni)Ti$_2$ → (Fe,Ni)Ti + L melting is unable to occur in direct connection with the exothermic reaction of the melt that creates the peak. The second part of the peak would thus be the reaction of the melt formed when (Fe,Ni)Ti$_2$ does melt. There are several possible reasons as to why the area of the first part of the exothermic peak decreases as the iron content is increased. As both the iron and nickel can form compounds with the titanium, then a higher iron content will mean a larger (Fe,Ni):Ti ratio. If more (Fe,Ni)Ti$_2$ forms then there is less titanium available for the β-Ti + (Fe,Ni)Ti$_2$ → L reaction. Further, the amount of (Fe,Ni)Ti$_2$ that is in direct contact with the β-Ti would presumably be less, as the area of the unreacted titanium cores would become smaller in conjunction with a decrease in unreacted titanium. If the size of the first part of the exothermic peak is dependent on the amount of β-Ti available then, with higher amounts of iron in the system, more (Fe,Ni)Ti$_2$ will remain after the first part of the exothermic peak. The second part of the peak does therefore grow at the expense of the first part. The temperatures associated with the β-Ti + (Fe,Ni)Ti$_2$ → L and (Fe,Ni)Ti$_2$ → (Fe,Ni)Ti + L reactions, are assumed to depend on the ratio of iron to nickel in (Fe,Ni)Ti$_2$. Especially since the increase in onset temperatures for the two parts of the exothermic peak show a clear dependence on the iron content in the sample, see Figure 38. If the ratio of iron to nickel in the (Fe,Ni)Ti$_2$ compound does affect the temperatures for the reactions connected to the two parts of the exothermic peak, it can explain why these peaks are relatively broad. Variations in the local composition of (Fe,Ni)Ti_2 would cause the β-Ti + (Fe,Ni)Ti_2 → L and (Fe,Ni)Ti_2 → (Fe,Ni)Ti + L reactions to occur at different temperatures in different parts of the sample. This could also be a contributing factor to the decreasing size of the first part of the peak, as both endothermic melting and exothermic reaction of the melt will overlap throughout the peak, decreasing its total area.

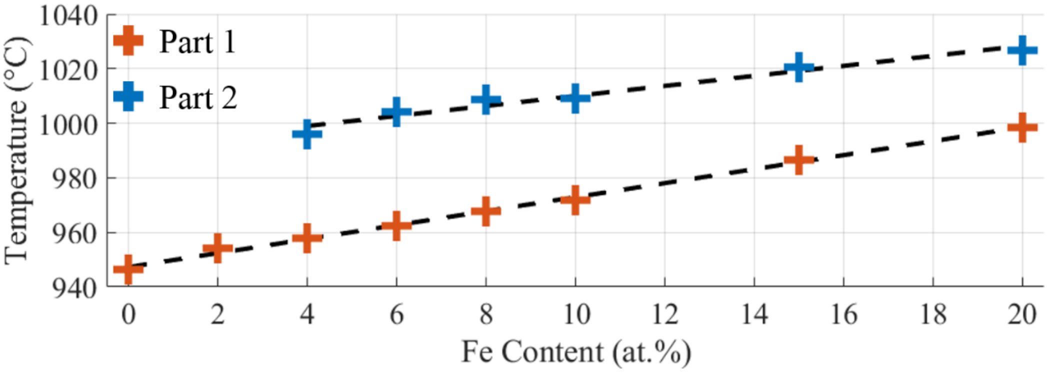

Figure 38. Average onset temperatures of the two parts of the exothermic peak plotted against the iron content in the sample, together with a linear regression for each.

The combined endothermic and exothermic peak is the result of the (Fe,Ni)Ti + Ni_3Ti → L melting. A probable reason as to why the endothermic part grows in size as the iron content is increased is that the (Fe,Ni):Ti ratio increases. This causes more Ni-rich compounds to form, including Ni_3Ti, and since the (Fe,Ni)Ti phase is plentiful in the sample it is the availability of Ni_3Ti that limits the (Fe,Ni)Ti + Ni_3Ti → L reaction. Thus higher iron content corresponds to higher amounts of Ni_3Ti and consequently a larger endothermic peak. The TiFe + β-Ti → L melting found in the binary Ti-50Fe sample (see Figure 14) has an onset temperature of 1091 °C, which is close to the onset temperatures of the combined peak. It is however unlikely that the TiFe + β-Ti → L reaction is involved in this peak as no unreacted titanium has been detected in any sample after the exothermic peak.

4.5. Additional Comments

Concerning the prepared samples, it was assumed that the nickel, titanium and iron were evenly distributed in the powder mixtures. Further, that no element had stuck to, for example the vials they were stored in, to a higher degree than either of the two other elements. Since the powder mixtures were assumed to be homogeneous the same was expected of the sample discs. However, these assumptions are unlikely to be true and minor deviations from the homogeneity can explain the slight differences between the results from repeated experiments.

For the analysis of the DSC curves, the temperatures of several points of interest were measured, among them the onset and peak temperatures. The values given for these are averages, as they occasionally varied by up to a few degrees between repeated experiments. When measuring the areas of the peaks it was on several occasions difficult to determine the position of the baseline. Thus, no specific values are given for the areas. However the trends are given in the cases they could be determined. A peak that becomes either less exothermic or less endothermic thus has a smaller area compared to a different composition, and similarly if the area increases.

Due to time constraints, and limited access to the right equipment the NiTi-6Fe samples heated to 900 °C and to 1000 °C were not analysed by neither SEM nor XRD. The binary samples, apart from the NiTi-0Fe, were also only studied using DSC.

The porosity of the samples were shown to increase with increasing temperature in Figure 16. The increase in porosity followed largely from when melting occurred in the sample. Between Figure 16 (a) and (b) the β-Ti + (Fe,Ni)Ti_2 → L and (Fe,Ni)Ti_2 → (Fe,Ni)Ti + L melting procedures occurred, and between (b) and (c) was the (Fe,Ni)Ti + Ni_3Ti → L reaction. As no melting took place between Figure 16 (c) and (d) the porosity in these samples is about the same.

For the EDS analysis it would have been beneficial to use different accelerating voltages in order to obtain better data for the compositions of the needles, grain boundaries and grey spots. As it was the EDS analysis was mainly performed using 30 keV. During the analysis of the EDS data, the composition determined for a few points in several of the samples did not match the expected composition, based on the visual information provided by the BSE image. Therefore, these points were excluded when calculating the average composition in each phase.

A metastable Ni_2Ti compound could be present in several of the samples. The EDS showed multiple areas with a composition matching it. However, it could also have been a mixture of NiTi and some more Ni-rich compound. It is difficult to determine if that compound was Ni_3Ti, Ni_4Ti_3 or perhaps Ni_2Ti. The XRD patterns were clearer about the presence of Ni_3Ti and Ni_4Ti_3 than Ni_2Ti. In the case of the first two, the patterns showed a few peaks that only matched either Ni_3Ti or Ni_4Ti_3. However, for Ni_2Ti all of its characteristic peaks were overlapping with peaks belonging to other elements or compounds.

Unfortunately, there were several smaller peaks in the XRD patterns that could not be identified. They could potentially be the minor peaks of some of the elements and compounds present. Another possibility is that they are part of the background noise. The XRD database had no data on the (Fe,Ni)Ti and (Fe,Ni)Ti_2 compounds, as the exact position of their peaks would depend on their specific composition. Thus these peaks could only be compared to reference patterns of NiTi and $NiTi_2$, and are therefore presented as these compounds, even though they actually belong to (Fe,Ni)Ti and (Fe,Ni)Ti_2, respectively.

5. Conclusions

In this project, the intermetallic compound formation in the Ni-Ti-Fe ternary system was studied using elementary powder mixtures of nickel, titanium and iron. In samples containing equiatomic amounts of nickel and titanium, and 0-20 at.% Fe, heated from room temperature to 1200 °C, the (Fe,Ni)Ti_2, (Fe,Ni)Ti, Ni_3Ti and Ni_4Ti_3 compounds formed, with iron acting as a substituent to nickel in both (Fe,Ni)Ti_2 and (Fe,Ni)Ti. The compounds all have their origin in the Ni-Ti binary system, and no Fe-based intermetallic compounds were identified in the samples.

The (Fe,Ni)Ti_2, (Fe,Ni)Ti and Ni_3Ti compounds formed due to solid-state diffusional reactions prior to any melt formation in the sample. Iron and nickel diffused into titanium to a higher degree than titanium diffused into nickel. As the heating was prolonged, the reactions in the system moved it towards the (Fe,Ni)Ti compound that matches the composition of the sample. Further, with increasing (Fe,Ni):Ti ratio, the amount of the Ni-rich compounds also increased.

The DSC curves evolved from the shape found in the equiatomic Ni-Ti binary system, the large exothermic peak became smaller, split into two parts and the onset temperatures of both parts increased with the iron content. The onset temperature of the combined endothermic and exothermic peak remained roughly the same, but the size of the endothermic part increased with increasing iron content. The onset temperatures of the two parts of the exothermic peak was seen to depend linearly on the iron content in the sample. It is believed that the temperatures associated with the $\beta\text{-Ti} + (\text{Fe,Ni})\text{Ti}_2 \rightarrow \text{L}$ melting connected to the first part of the peak, and the $(\text{Fe,Ni})\text{Ti}_2 \rightarrow (\text{Fe,Ni})\text{Ti} + \text{L}$ reaction connected to the second part, are both dependent on the ratio of iron to nickel in the (Fe,Ni)Ti_2 compound. The temperatures of the $(\text{Fe,Ni})\text{Ti} + \text{Ni}_3\text{Ti} \rightarrow \text{L}$ melting, which is responsible for the combined endothermic and exothermic peak, does not appear to be strongly affected by the ratio of iron to nickel.

It is still unknown exactly what happens in the samples containing 15 and 20 at.% Fe above 1120 °C, as complications, related to the strong melting that occurred, made it difficult to further investigate samples heated to these temperatures. The origin of the broad exothermic peaks that appear between 780 °C and 930 °C on the cooling curves of some samples is also uncertain, but proposed to be connected to the allotropic transformation of iron.

6. Future work

There are a number of parameters that affect the phase evolution in Ni-Ti-Fe powder mixtures, many of them have not been investigated in this project as the focus here was in the effect of the iron content. One of these parameters is the particle size of the powders as well as different combinations of small and large particle sizes. Another parameter is the composition of the samples. Compositions that deviate from the equiatomic Ni-Ti could be investigated, as could higher amounts of iron. It would also be very beneficial to develop a method that allowed a more thorough analysis of the samples containing more than 10 at.% Fe. Especially as it seems likely that intermetallic compounds containing iron does not form in samples with small amounts of iron, as the solubility of the element is high in the Ni-Ti based intermetallic compounds.

The effect of heating and cooling rate on the shape of the DSC curves is another avenue for further investigation. A faster rate has the possibility of allowing reactions that exhibit less exothermicicty or endothermicity to present themselves on the DSC curve. Prolonged sintering at a specific temperature, to investigate which compound is the most stable under those conditions, could also be done. The differential scanning calorimeter used in this project had an operating temperature range outside of the temperatures for which the shape memory effect in Ni-Ti-Fe is supposed to take place. With a temperature range extending into lower temperatures it would be possible to investigate the shape memory effect of the material.

Due to the small size of the samples produced in this project no mechanical testing was performed. If larger samples could be produced then studies on the mechanical properties of the materials would be of great interest. Alternatively, mechanical testing designed for small samples, such as nanoindentation, could be performed.

Finally, it would also be of interest to investigate the effect of another element on the binary Ni-Ti system. A study on the Ni-Ti-Cu system has already begun, other elements of interest are aluminium, palladium, zirconium and hafnium.

References

Literature

1. Cacciamani, G., et al., *Critical evaluation of the Fe–Ni, Fe–Ti and Fe–Ni–Ti alloy systems.* Intermetallics, 2006. **14**(10): p. 1312-1325.

2. De Keyzer, J., et al., *Thermodynamic modeling and optimization of the Fe–Ni–Ti system.* Calphad, 2009. **33**(1): p. 109-123.

3. Ghosh, G., *Fe-Ni-Ti (Iron - Nickel - Titanium)*, in *Light Metal Systems. Part 4: Selected Systems from Al-Si-Ti to Ni-Si-Ti*, G. Effenberg and S. Ilyenko, Editors. 2006, Springer Berlin Heidelberg: Berlin, Heidelberg. p. 299-316.

4. Otsuka, K. and C.M. Wayman, *Shape memory materials*. 1999: Cambridge : Cambridge University Press, 1999, 1. paperback ed.(with corr.).

5. Mohd Jani, J., et al., *A review of shape memory alloy research, applications and opportunities.* Materials & Design (1980-2015), 2014. **56**: p. 1078-1113.

6. Smallman, R.E. and A.H.W. Ngan, *Modern Physical Metallurgy*. 8 ed. 2014, Oxford, UK: Butterworth-Heinemann. 720.

7. Ekhard, K.H.S., et al., *Martensitic transformation B2–R in Ni–Ti–Fe: experimental determination of the Landau potential and quantum saturation of the order parameter.* Journal of Physics: Condensed Matter, 2008. **20**(27): p. 275216.

8. Basu, R., et al., *A systematic investigation on the role of microstructure on phase transformation behavior in Ni–Ti–Fe shape memory alloys.* Journal of Alloys and Compounds, 2015. **645**(C): p. 213-222.

9. Edmonds, K.R. and C.M. Hwang, *Phase transformations in ternary TiNix alloys.* Scripta Metallurgica, 1986. **20**(5): p. 733-737.

13. Jabur, A.S., J.T. Al-Haidary, and E.S. Al-Hasani, *Characterization of Ni–Ti shape memory alloys prepared by powder metallurgy.* Journal of Alloys and Compounds, 2013. **578**: p. 136-142.

14. de Araújo, C.J., et al., *A comparative study of Ni–Ti and Ni–Ti–Cu shape memory alloy processed by plasma melting and injection molding.* Materials & Design, 2011. **32**(10): p. 4925-4930.

15. Duarte, L.I., et al., *Experimental study of the Fe–Ni–Ti system.* Intermetallics, 2010. **18**(3): p. 374-384.

16. Nakajima, H. and M. Koiwa, *Diffusion in Titanium.* ISIJ International, 1991. **31**(8): p. 757-766.

17. Shapovalov, V.P. and A.N. Kurasov, *Diffusion of titanium in iron.* Metal Science and Heat Treatment, 1975. **17**(9): p. 803-805.

18. Bastin, G.F. and G.D. Rieck, *Diffusion in the titanium-nickel system: II. calculations of chemical and intrinsic diffusion coefficients.* Metallurgical Transactions, 1974. **5**(8): p. 1827-1831.

19. Frenzel, J., et al., *On the influence of thermomechanical treatments on the microstructure and phase transformation behavior of Ni–Ti–Fe shape memory alloys.* Materials Science and Engineering: A, 2008. **481-482**: p. 635-638.

20. Xu, H., et al., *Martensitic transformation of the Ti50Ni48Fe2 alloy deformed at different temperatures.* Materials Science and Engineering: A, 2000. **281**(1): p. 234-238.

21. Chu, J.P., et al., *Deposition and characterization of TiNi-base thin films by sputtering.* Materials Science and Engineering: A, 2000. **277**(1): p. 11-17.

22. Basu, R., et al., *Dynamic recrystallization in a Ni–Ti–Fe shape memory alloy: Effects on austenite–martensite phase transformation.* Journal of Alloys and Compounds, 2015. **639**: p. 94-101.

23. Höhne, G., W. Hemminger, and H.J. Flammersheim, *Differential scanning calorimetry : an introduction for practitioners*. 2nd rev. and enl. ed. ed. 2003: Berlin ; New York : Springer.

25. Goldstein, J.I., et al., *Scanning Electron Microscopy and X-Ray Microanalysis*. 2018: New York, NY : Springer New York : Imprint: Springer, 2018. 4th ed. 2018.

28. Sina, H., K.B. Surreddi, and S. Iyengar, *Phase evolution during the reactive sintering of ternary Al–Ni–Ti powder compacts.* Journal of Alloys and Compounds, 2016. **661**: p. 294-305.

Figures

10. *Cubic*. https://commons.wikimedia.org/wiki/File:Cubic.svg by Stannered is licensed under CC BY-SA 3.0. Accessed 2018-06-29.

11. *RhombohedralD*. https://commons.wikimedia.org/wiki/File:RhombohedralD.svg by Officer781 is licensed under CC BY-SA 4.0. Accessed 2018-06-29.

12. *Monoclinic*. https://commons.wikimedia.org/wiki/File:Monoclinic.svg by Stannered is licensed under CC BY-SA 3.0. Accessed 2018-06-29.

24. NETZSCH, *Simultaneous Thermal Analyzer – STA 449 F3 Jupiter®.* https://www.netzsch-thermal-analysis.com/en/products-solutions/simultaneous-thermogravimetry-differential-scanning-calorimetry/sta-449-f3-jupiter/. Accessed 2018-07-11.

26. *Schema MEB (en)*. https://commons.wikimedia.org/wiki/File:Schema_MEB_(en).svg by Steff is licensed under CC BY-SA 3.0. Accessed 2018-07-11.

27. STOE, *STOE STADI MP*. https://www.stoe.com/product/stadi-mp/. Accessed 2018-07-26.

Appendices

Appendix I – DSC

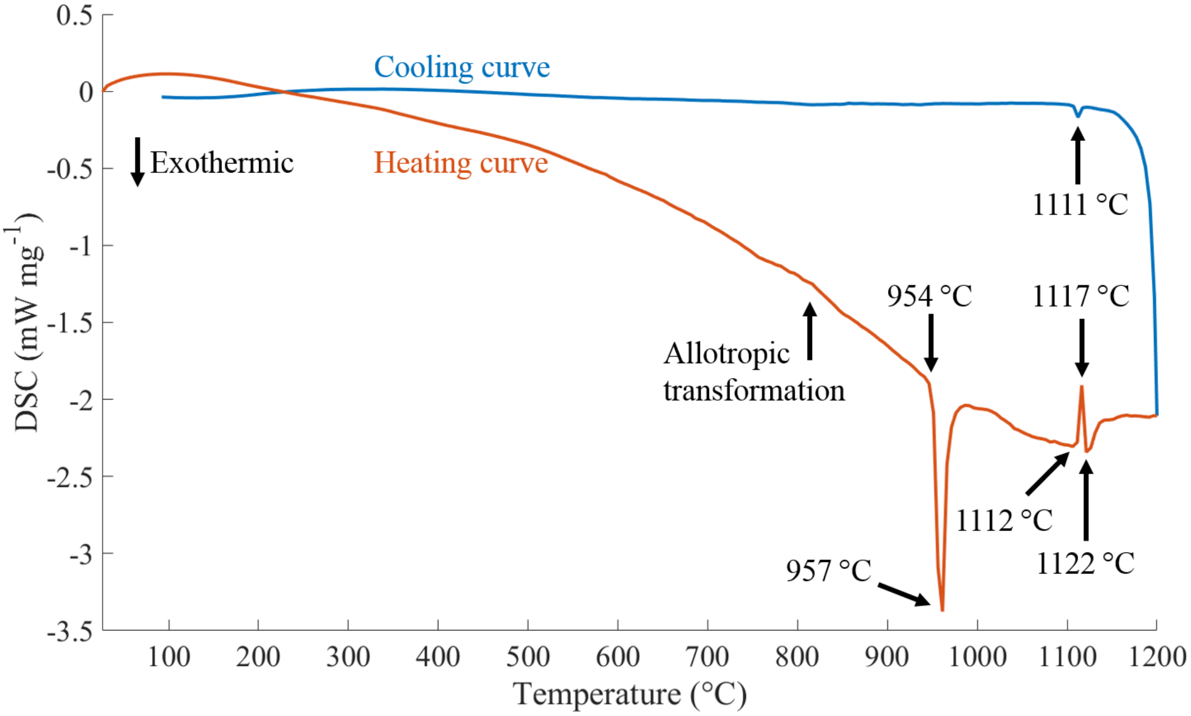

Appendix I - 1. DSC curve for NiTi-2Fe heated to 1200 °C.

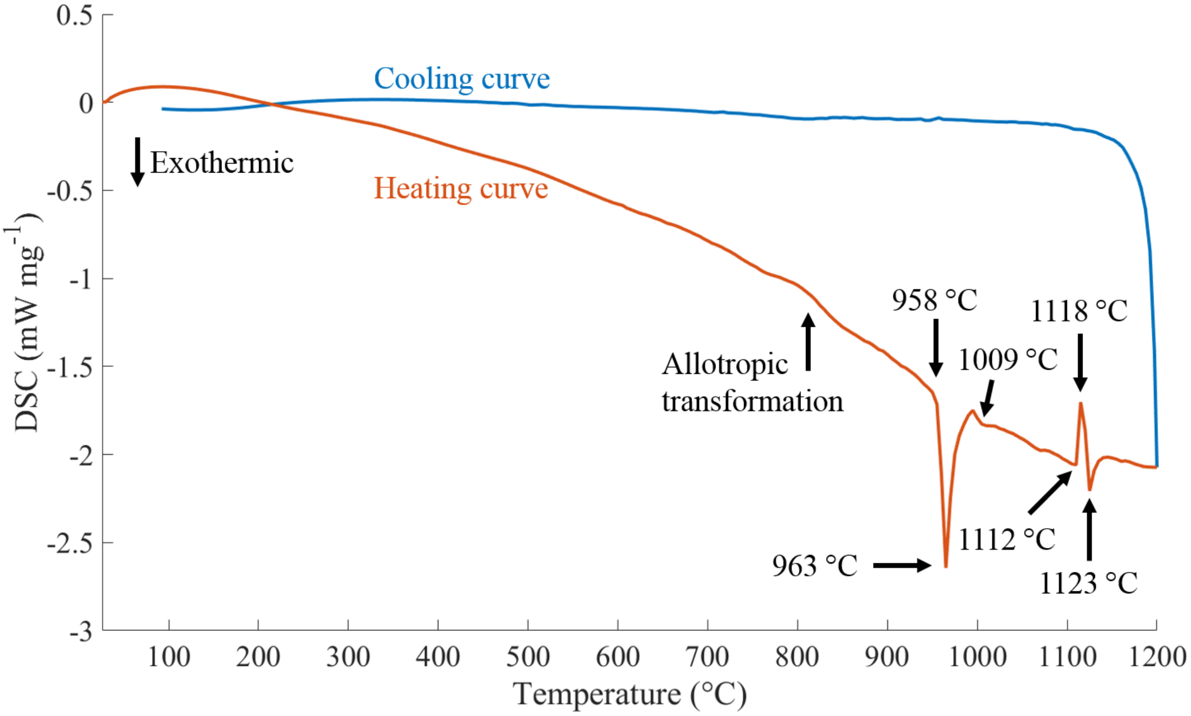

Appendix I - 2. DSC curve for NiTi-4Fe heated to 1200 °C.

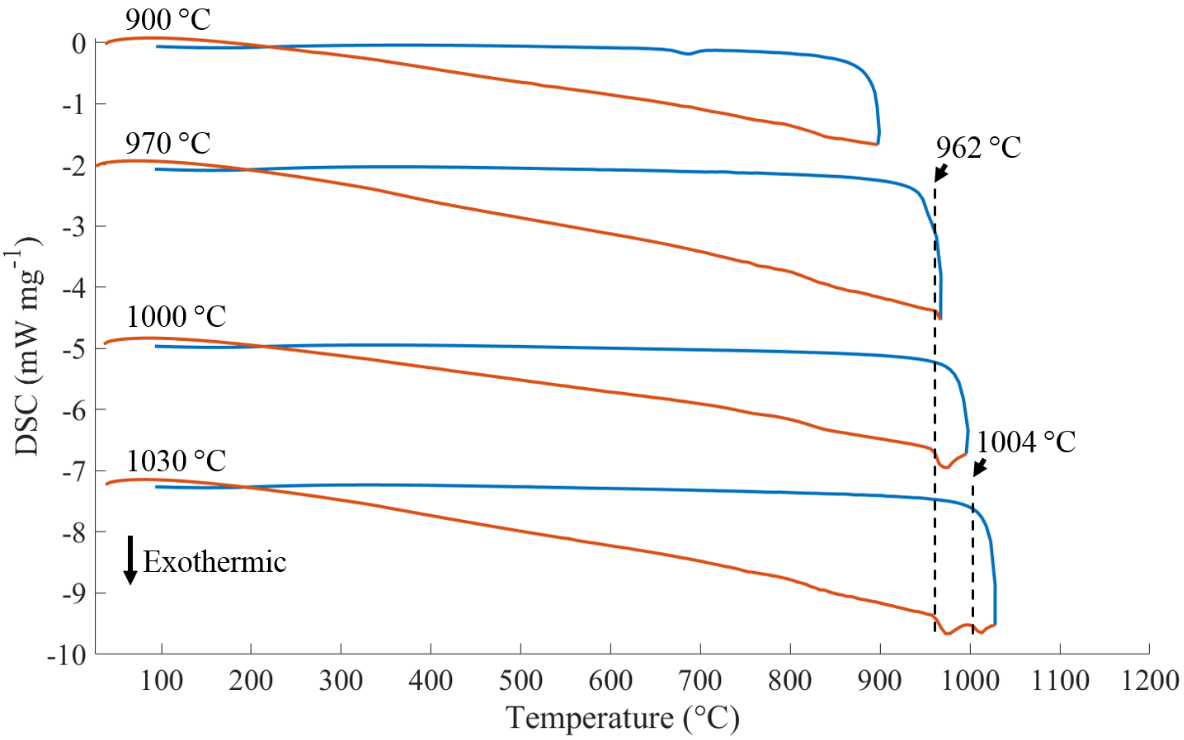

Appendix I - 3. DSC curves for the NiTi-6Fe samples, heated to 900 °C, 970 °C, 1000 °C and 1030 °C. Heating curves in red (bottom) and cooling curves in blue (top).

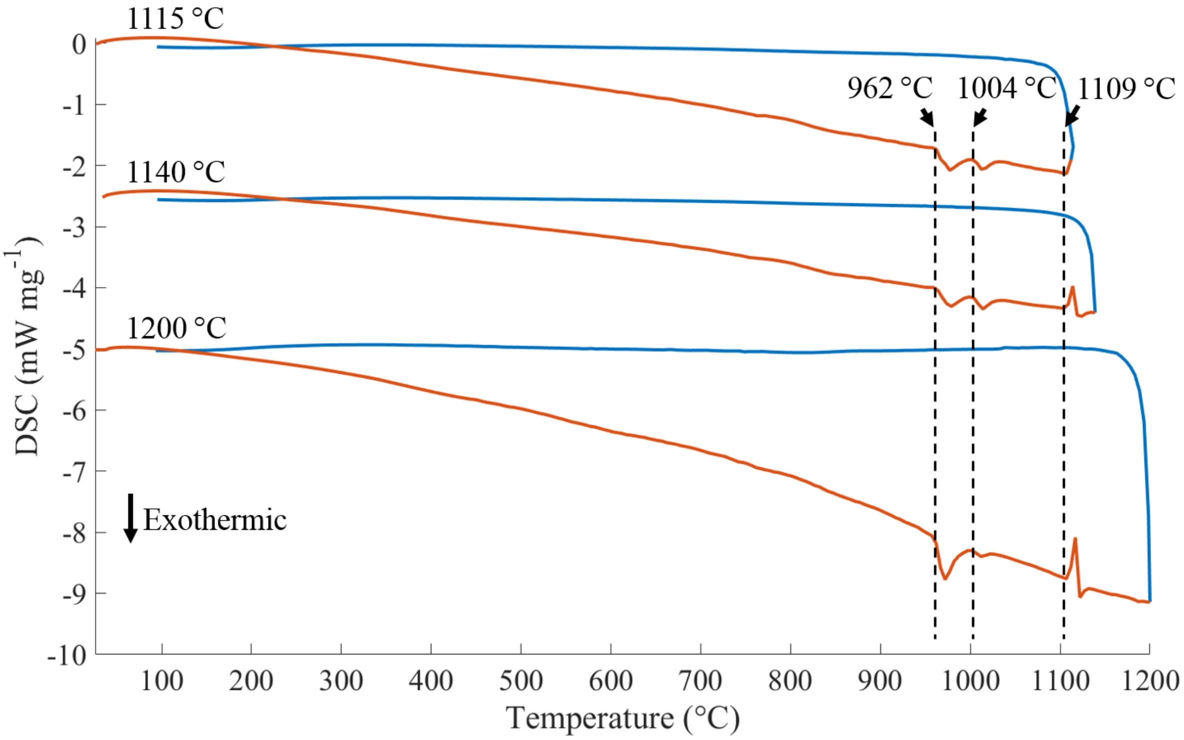

Appendix I - 4. DSC curves for the NiTi-6Fe samples, heated to 1115 °C, 1140 °C and 1200 °C. Heating curves in red (bottom) and cooling curves in blue (top).

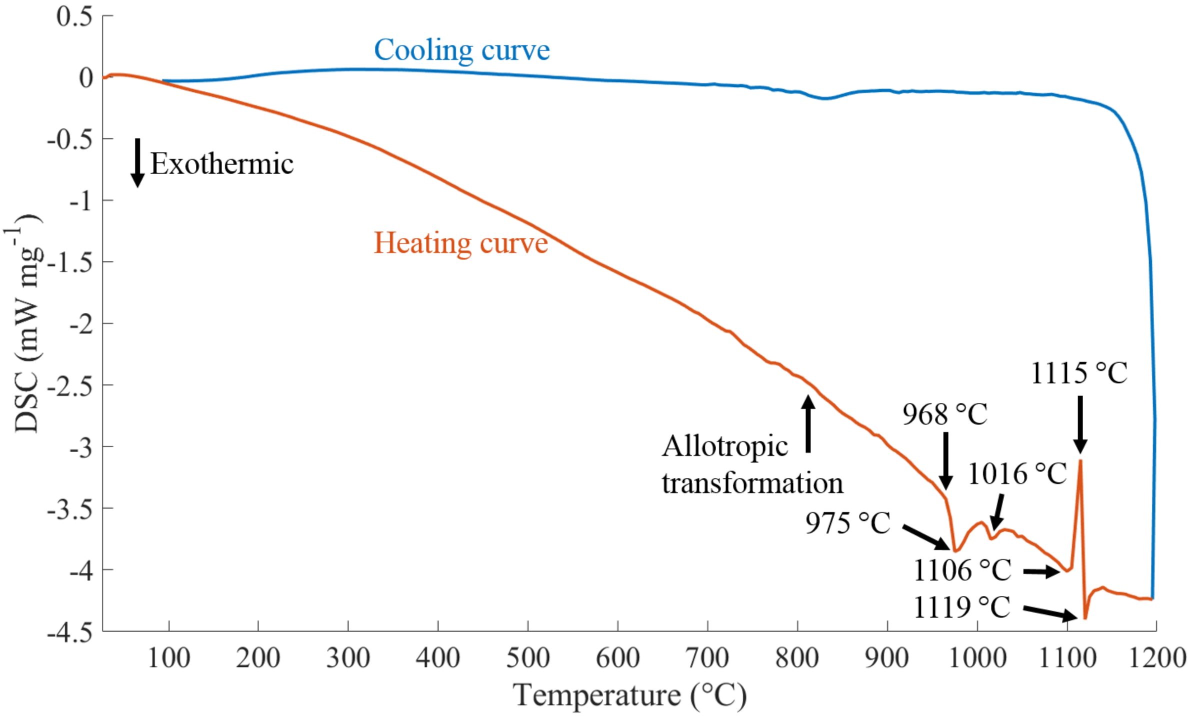

Appendix I - 5. DSC curve for NiTi-8Fe heated to 1200 °C.

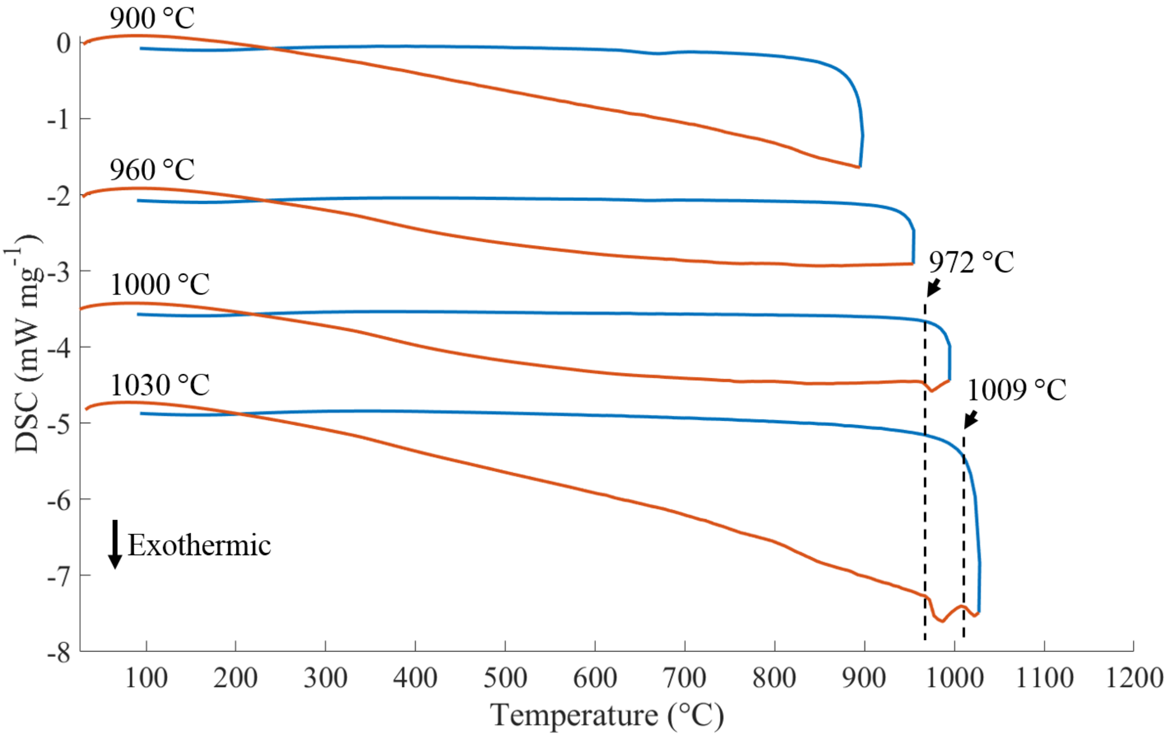

Appendix I - 6. DSC curves for the NiTi-10Fe samples, heated to 900 °C, 960 °C, 1000 °C and 1030 °C. Heating curves in red (bottom) and cooling curves in blue (top).

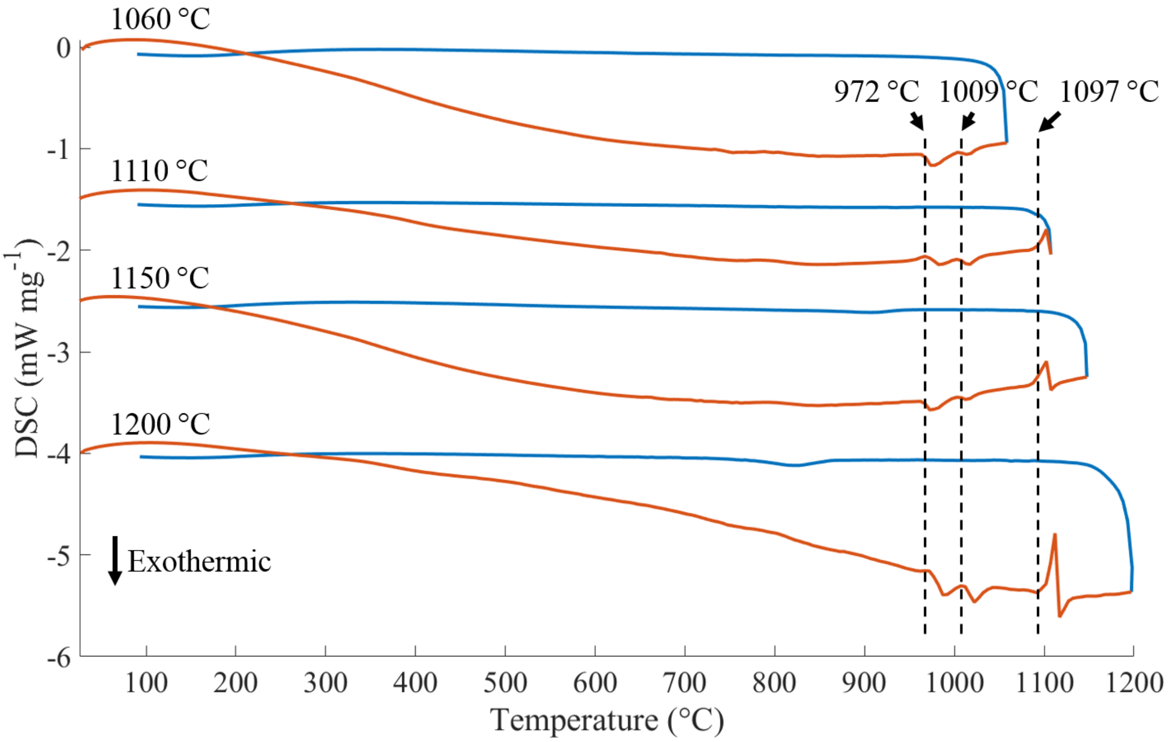

Appendix I - 7. DSC curves for the NiTi-10Fe samples, heated to 1060 °C, 1110 °C, 1150 °C and 1200 °C. Heating curves in red (bottom) and cooling curves in blue (top).

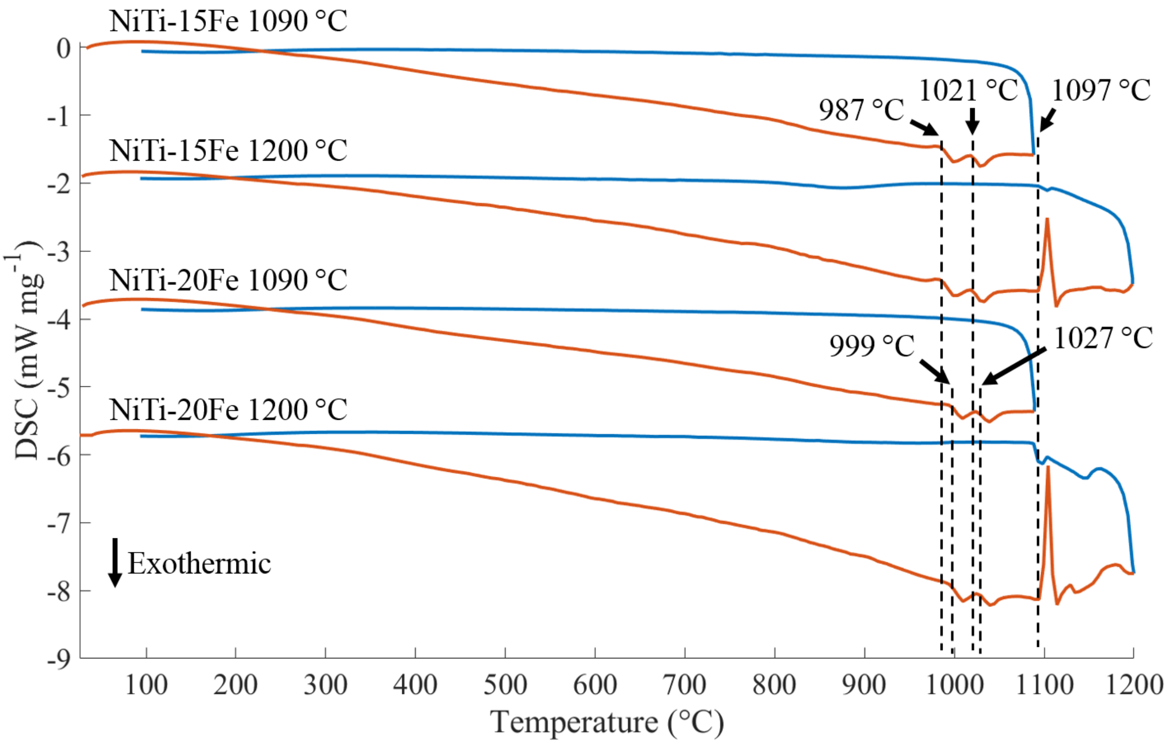

Appendix I - 8. DSC curves for NiTi-15Fe and NiTi-20Fe, both heated to 1090 °C and to 1200 °C. Heating curves in red (bottom) and cooling curves in blue (top).

Appendix II – EDS

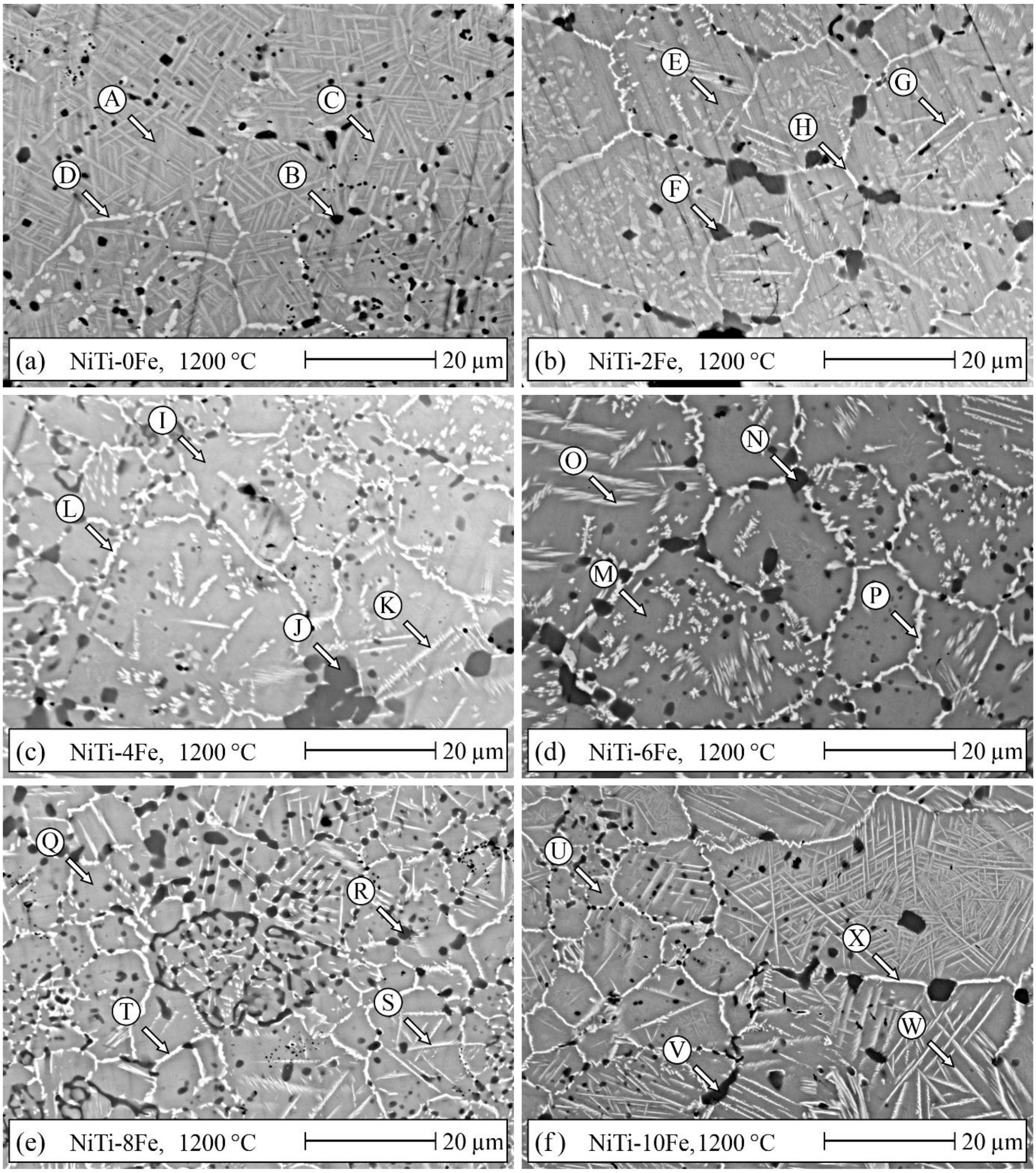

Appendix II - 1. BSE images of samples containing 0-10 at.% Fe, heated to 1200 °C. Estimated compositions of the marked regions are found in Appendix II - 2.

Appendix II - 2. Chemical composition of the regions marked in Appendix II - 1, estimated by EDS.

Sample	Regions in micrograph	Composition			Phase/Region
		Ti	Fe	Ni	
NiTi-0Fe	A	47.5 ± 1.3	-	52.5 ± 1.3	NiTi
	B	53.0 ± 4.0	-	47.0 ± 4.0	Grey spot
	C	44.9 ± 0.7	-	55.1 ± 0.7	Needle
	D	41.5 ± 0.4	-	58.5 ± 0.4	Grain boundary
NiTi-2Fe	E	45.7 ± 2.4	2.1 ± 0.2	52.2 ± 2.6	NiTi
	F	56.5 ± 3.1	2.1 ± 0.2	41.4 ± 2.9	Grey spot
	G	41.8 ± 0.9	1.8 ± 0.1	56.4 ± 1.0	Needle
	H	38.3 ± 3.6	1.8 ± 0.2	59.9 ± 3.8	Grain boundary
NiTi-4Fe	I	45.4 ± 1.7	3.7 ± 0.1	50.9 ± 1.8	NiTi
	J	57.9 ± 2.6	3.9 ± 0.2	38.2 ± 2.6	Grey spot
	K	39.5 ± 1.5	3.0 ± 0.4	57.5 ± 1.8	Needle
	L	36.3 ± 1.7	2.7 ± 0.2	61.0 ± 1.9	Grain boundary
NiTi-6Fe	M	45.7 ± 0.5	5.8 ± 0.2	48.6 ± 0.6	NiTi
	N	53.5 ± 2.5	6.2 ± 0.5	40.3 ± 2.8	Grey spot
	O	38.7 ± 1.4	5.0 ± 0.5	56.4 ± 2.0	Needle
	P	40.5 ± 3.8	5.2 ± 0.7	54.4 ± 4.4	Grain boundary
NiTi-8Fe	Q	45.6 ± 1.1	7.1 ± 0.3	47.3 ± 1.0	NiTi
	R	53.6 ± 2.5	7.5 ± 0.8	38.9 ± 2.7	Grey spot
	S	41.5 ± 1.8	6.3 ± 0.6	52.2 ± 2.2	Needle
	T	39.8 ± 1.2	5.7 ± 0.4	54.5 ± 1.5	Grain boundary
NiTi-10Fe	U	44.9 ± 1.0	9.6 ± 0.2	45.6 ± 1.1	NiTi
	V	52.1 ± 2.0	10.9 ± 0.5	37.0 ± 2.4	Grey spot
	W	41.2 ± 1.2	8.7 ± 0.4	50.2 ± 1.5	Needle
	X	38.3 ± 2.1	7.7 ± 0.7	54.0 ± 2.8	Grain boundary

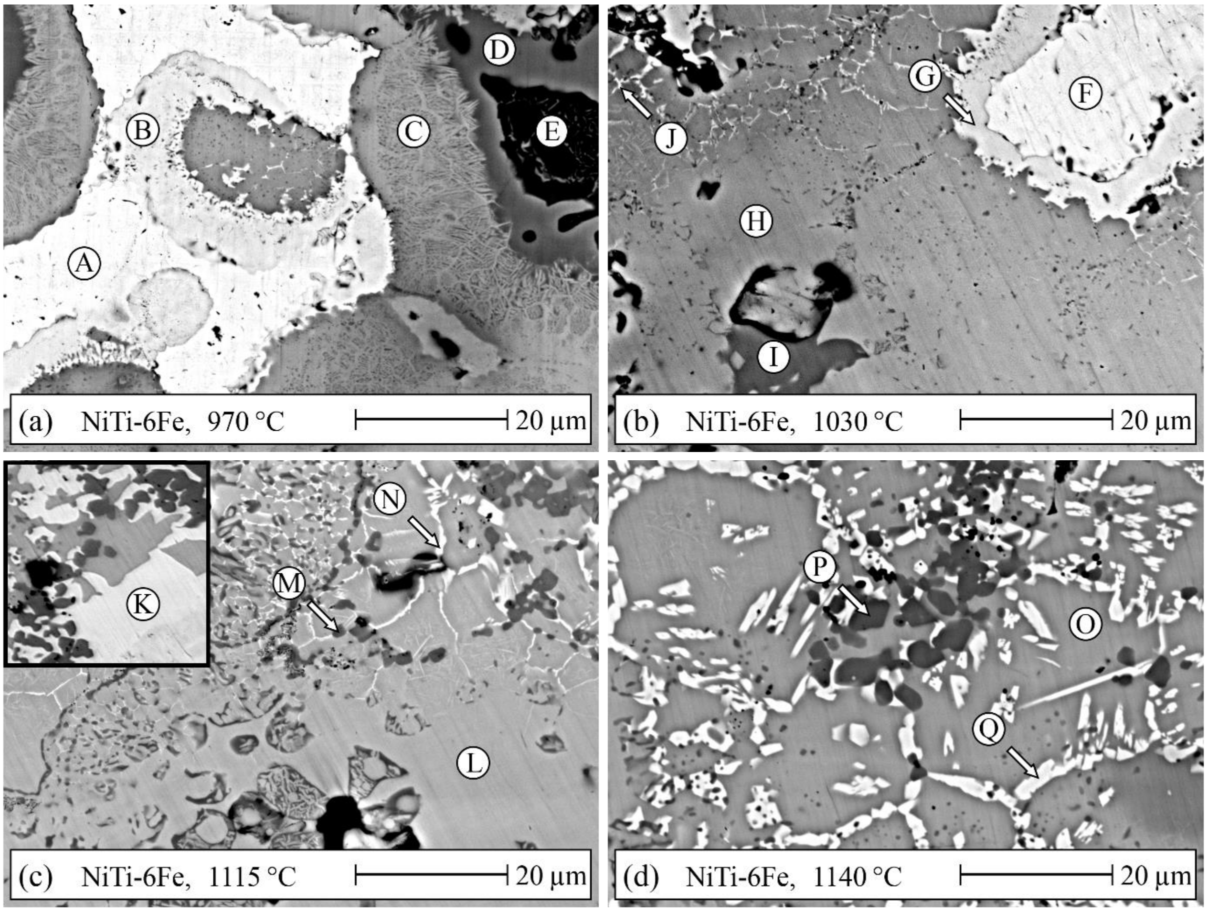

Appendix II - 3. BSE images of sample NiTi-6Fe heated to 970-1140 °C. The inlaid image in (c) is from another part of the same sample. Estimated compositions of the marked regions are found in Appendix II - 4.

Appendix II - 4. Chemical composition of the regions marked in Appendix II - 3 estimated by EDS.

Sample	Regions in micrograph	Composition			Phase/Region
		Ti	Fe	Ni	
970 °C	A	3.2 ± 1.9	2.3 ± 1.8	94.5 ± 3.3	Ni
	B	23.4 ± 1.6	2.9 ± 1.9	73.7 ± 1.1	Ni_3Ti
	C	50.1 ± 1.7	4.8 ± 2.1	45.1 ± 2.5	NiTi
	D	66.5 ± 0.9	4.5 ± 0.6	29.1 ± 1.2	$NiTi_2$
	E	92.4 ± 2.9	2.0 ± 0.4	5.6 ± 2.6	Ti
1030 °C	F	2.5 ± 0.9	2.5 ± 1.5	95.0 ± 1.4	Ni
	G	24.7 ± 0.7	2.3 ± 0.9	73.0 ± 1.2	Ni_3Ti
	H	47.7 ± 1.7	5.5 ± 1.1	46.9 ± 2.3	NiTi
	I	64.5 ± 1.0	4.5 ± 0.3	31.0 ± 1.0	$NiTi_2$
	J	42.2 ± 0.9	4.5 ± 0.5	53.4 ± 1.3	Grain boundary
1115 °C	K	24.9 ± 0.6	5.0 ± 0.6	70.0 ± 0.7	Ni_3Ti
	L	47.0 ± 0.6	6.7 ± 0.7	46.3 ± 1.0	NiTi
	M	54.5 ± 2.1	7.4 ± 1.8	38.2 ± 3.1	Grey spot
	N	35.4 ± 2.0	4.5 ± 0.9	60.1 ± 2.3	Grain boundary
1140 °C	O	46.4 ± 0.2	6.5 ± 0.4	47.1 ± 0.5	NiTi
	P	53.7 ± 2.4	8.5 ± 0.9	37.9 ± 3.2	Grey spot
	Q	30.2 ± 1.1	3.3 ± 0.1	66.5 ± 1.2	Grain boundary

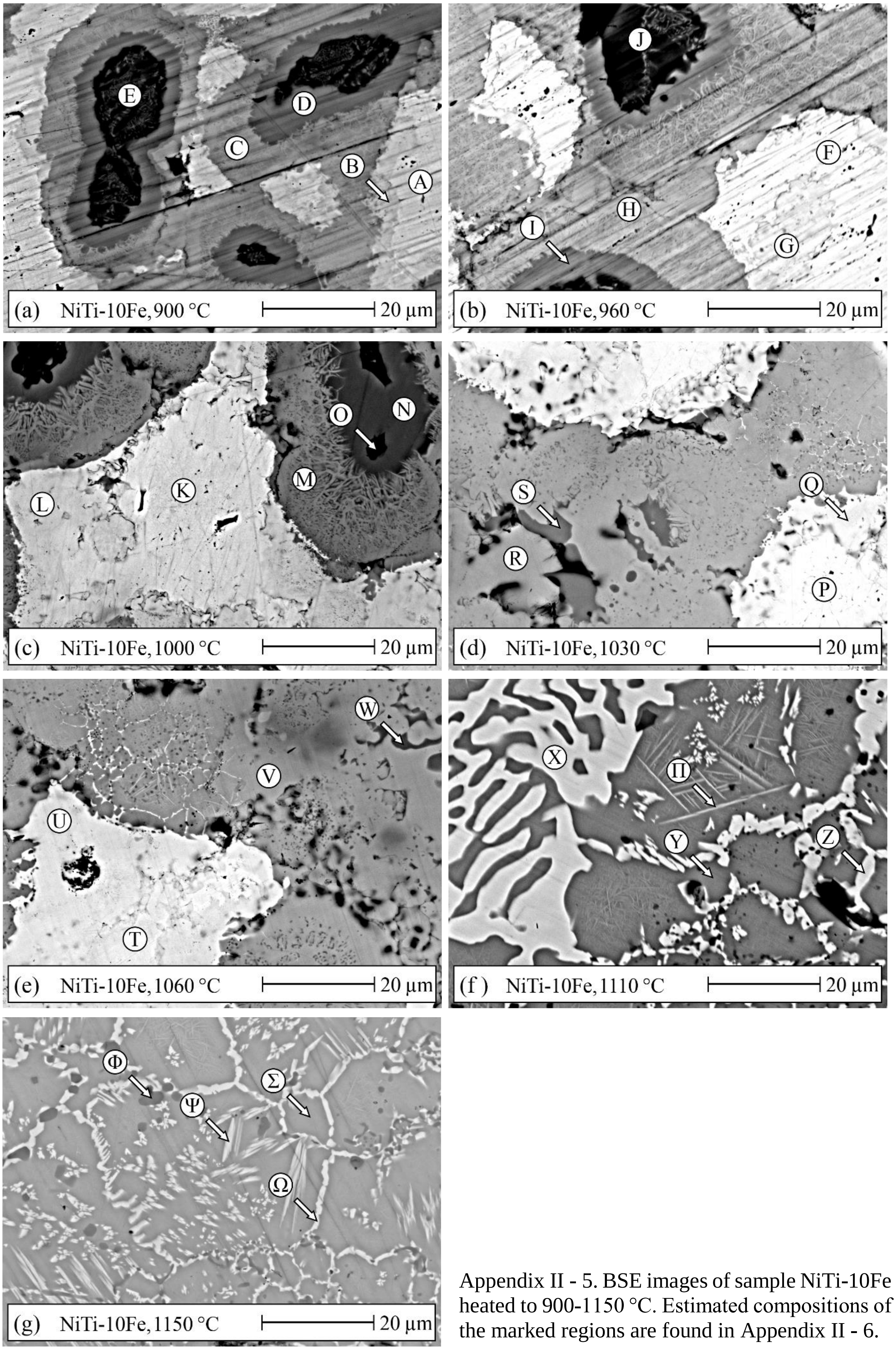

Appendix II - 5. BSE images of sample NiTi-10Fe heated to 900-1150 °C. Estimated compositions of the marked regions are found in Appendix II - 6.

Appendix II - 6. Chemical composition of the regions marked in Appendix II - 5 estimated by EDS.

Sample	Regions in micrograph	Composition			Phase/Region
		Ti	Fe	Ni	
900 °C	A	1.8 ± 0.9	2.6 ± 2.0	95.7 ± 2.5	Ni
	B	26.3 ± 1.5	3.7 ± 1.5	70.1 ± 1.6	Ni_3Ti
	C	51.0 ± 0.9	4.5 ± 1.4	44.5 ± 1.3	NiTi
	D	66.9 ± 1.2	6.5 ± 1.7	26.5 ± 2.4	$NiTi_2$
	E	91.8 ± 2.7	3.4 ± 1.2	4.9 ± 2.2	Ti
960 °C	F	2.5 ± 2.0	2.6 ± 1.4	95.0 ± 2.5	Ni
	G	23.6 ± 0.9	3.6 ± 1.8	72.8 ± 1.5	Ni_3Ti
	H	49.7 ± 2.0	5.9 ± 2.3	44.5 ± 2.9	NiTi
	I	65.6 ± 0.7	6.6 ± 2.2	27.9 ± 2.3	$NiTi_2$
	J	93.6 ± 3.2	2.3 ± 1.3	4.1 ± 2.0	Ti
1000 °C	K	1.7 ± 1.0	4.9 ± 3.8	93.5 ± 4.2	Ni
	L	23.7 ± 1.3	4.5 ± 1.3	71.8 ± 2.1	Ni_3Ti
	M	48.8 ± 1.8	7.1 ± 1.4	44.2 ± 2.5	NiTi
	N	65.5 ± 0.6	8.0 ± 1.2	26.5 ± 1.2	$NiTi_2$
	O	90.8 ± 3.7	4.2 ± 1.2	5.0 ± 3.4	Ti
1030 °C	P	3.3 ± 1.8	3.0 ± 2.0	93.8 ± 3.7	Ni
	Q	23.6 ± 1.0	5.2 ± 2.3	71.2 ± 2.5	Ni_3Ti
	R	46.8 ± 2.2	9.8 ± 2.0	43.3 ± 2.5	NiTi
	S	64.2 ± 1.1	7.4 ± 0.4	28.5 ± 1.2	$NiTi_2$
1060 °C	T	6.8 ± 0.6	5.6 ± 0.8	87.7 ± 1.0	Ni
	U	23.7 ± 1.0	3.8 ± 1.8	72.5 ± 2.5	Ni_3Ti
	V	48.6 ± 2.6	9.3 ± 2.2	42.1 ± 3.4	NiTi
	W	64.7 ± 1.3	7.1 ± 0.5	28.3 ± 1.3	$NiTi_2$
1110 °C	X	25.7 ± 1.2	6.2 ± 0.3	68.1 ± 1.4	Ni_3Ti
	Y	45.4 ± 0.9	10.8 ± 0.8	43.8 ± 0.7	NiTi
	Z	32.8 ± 3.6	6.5 ± 1.3	60.7 ± 4.7	Grain boundary
	Π	43.2 ± 2.4	9.9 ± 1.2	47.0 ± 3.6	Needle
1150 °C	Σ	44.4 ± 1.9	9.2 ± 0.3	46.4 ± 1.9	NiTi
	Φ	50.1 ± 1.4	11.0 ± 0.3	38.9 ± 1.5	Grey spot
	Ψ	39.7	8.1	52.2	Needle
	Ω	31.5 ± 1.3	5.4 ± 0.4	63.1 ± 1.6	Grain boundary

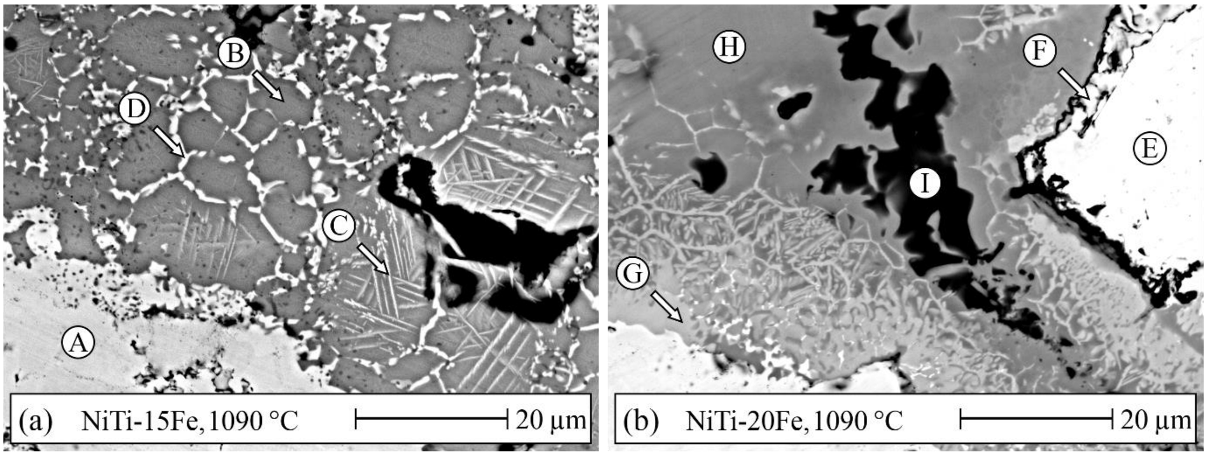

Appendix II - 7. BSE images of samples NiTi-15Fe and NiTi-20Fe heated to 1090 °C. Estimated compositions of the marked regions are found in Appendix II - 8.

Appendix II - 8. Chemical composition of the regions marked in Appendix II - 7 estimated by EDS.

Sample	Regions in micrograph	Composition			Phase/Region
		Ti	Fe	Ni	
NiTi-15Fe	A	24.1 ± 1.2	8.1 ± 3.1	67.8 ± 3.0	Ni_3Ti
	B	43.6 ± 3.3	15.1 ± 2.0	41.3 ± 2.7	NiTi
	C	41.7 ± 0.8	13.3 ± 0.3	45.1 ± 1.1	Needle
	D	36.2 ± 2.0	10.1 ± 1.4	53.7 ± 3.1	Grain boundary
NiTi-20Fe	E	3.4 ± 2.3	7.0 ± 3.1	89.6 ± 4.6	Ni
	F	24.0 ± 2.2	8.3 ± 4.2	67.8 ± 4.5	Ni_3Ti
	G	46.6 ± 2.3	15.9 ± 2.1	37.5 ± 2.2	NiTi
	H	62.8 ± 5.4	14.9 ± 5.1	22.4 ± 4.0	$NiTi_2$
	I	92.3 ± 4.0	2.9 ± 1.4	4.8 ± 2.6	Ti

Appendix III – XRD

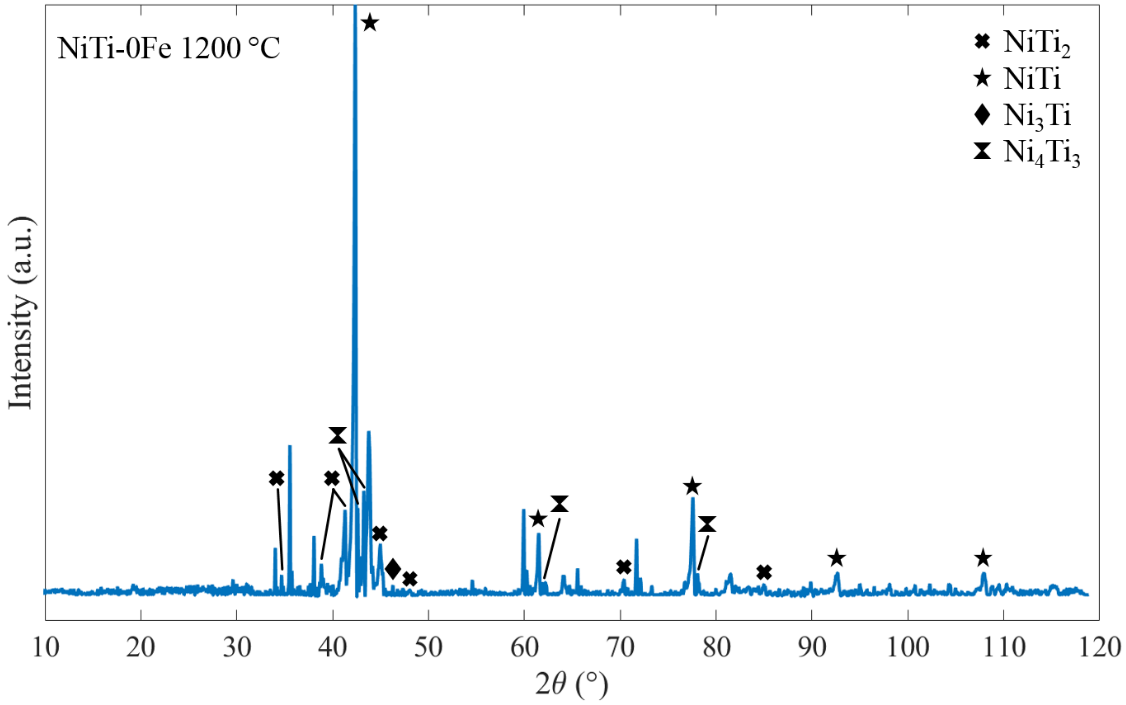

Appendix III - 1. XRD pattern for NiTi-0Fe, heated to 1200 °C.

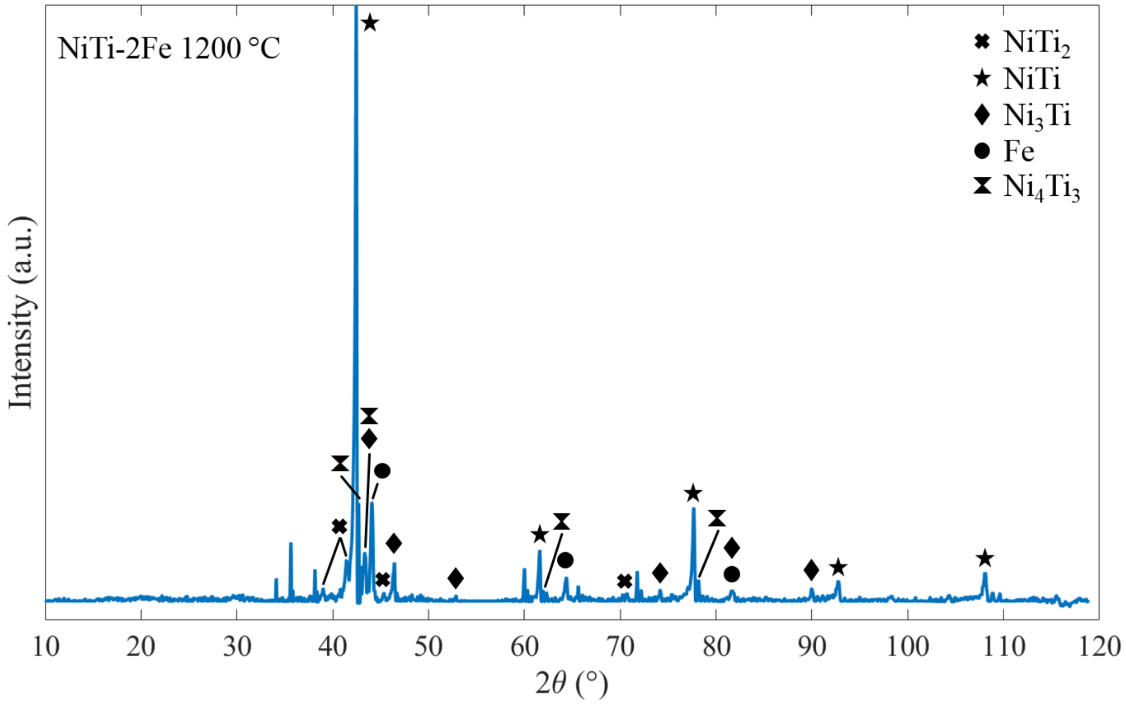

Appendix III - 2. XRD pattern for NiTi-2Fe, heated to 1200 °C.

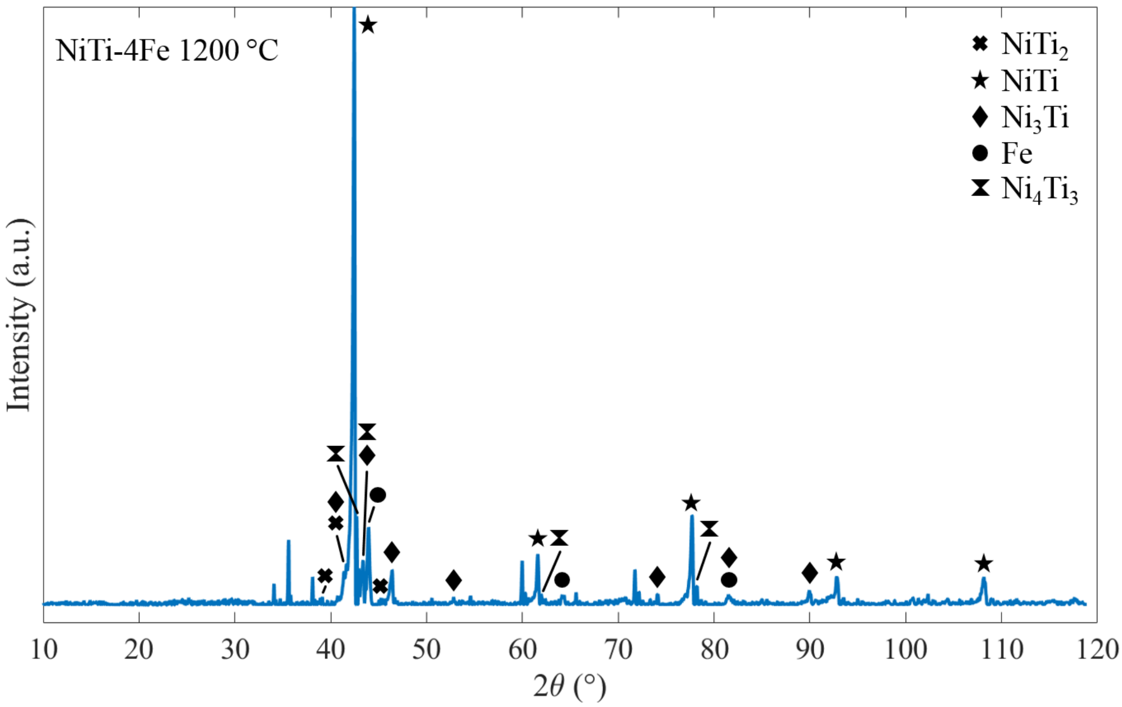

Appendix III - 3. XRD pattern for NiTi-4Fe, heated to 1200 °C.

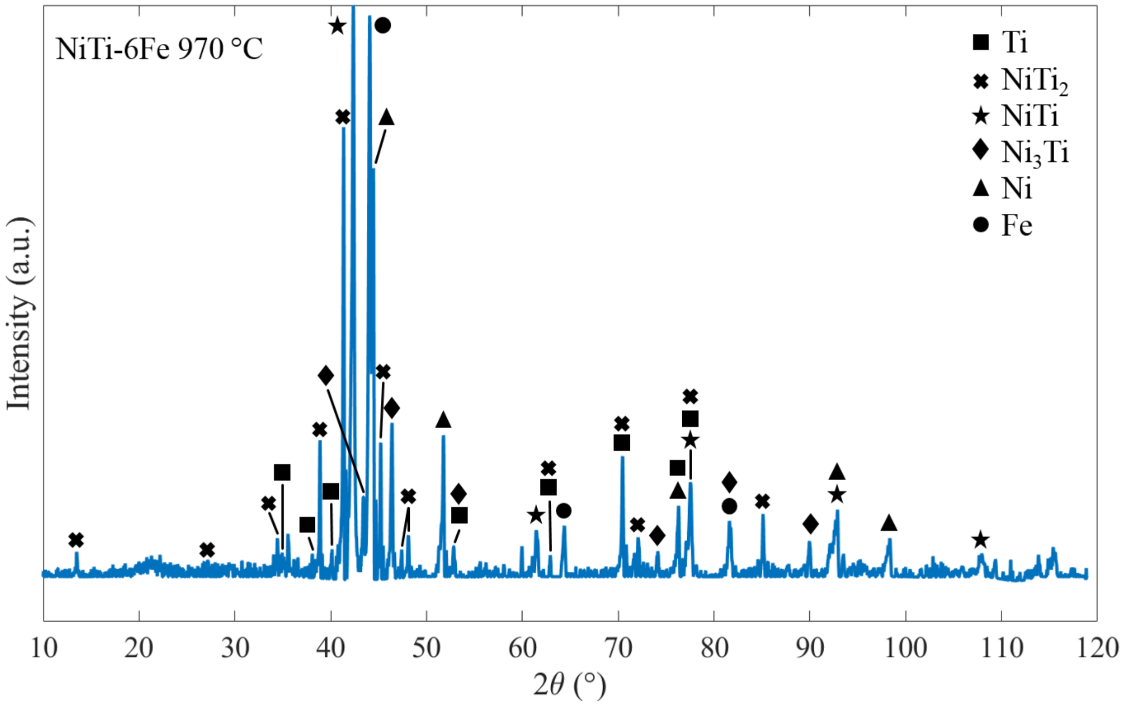

Appendix III - 4. XRD pattern for NiTi-6Fe, heated to 970 °C.

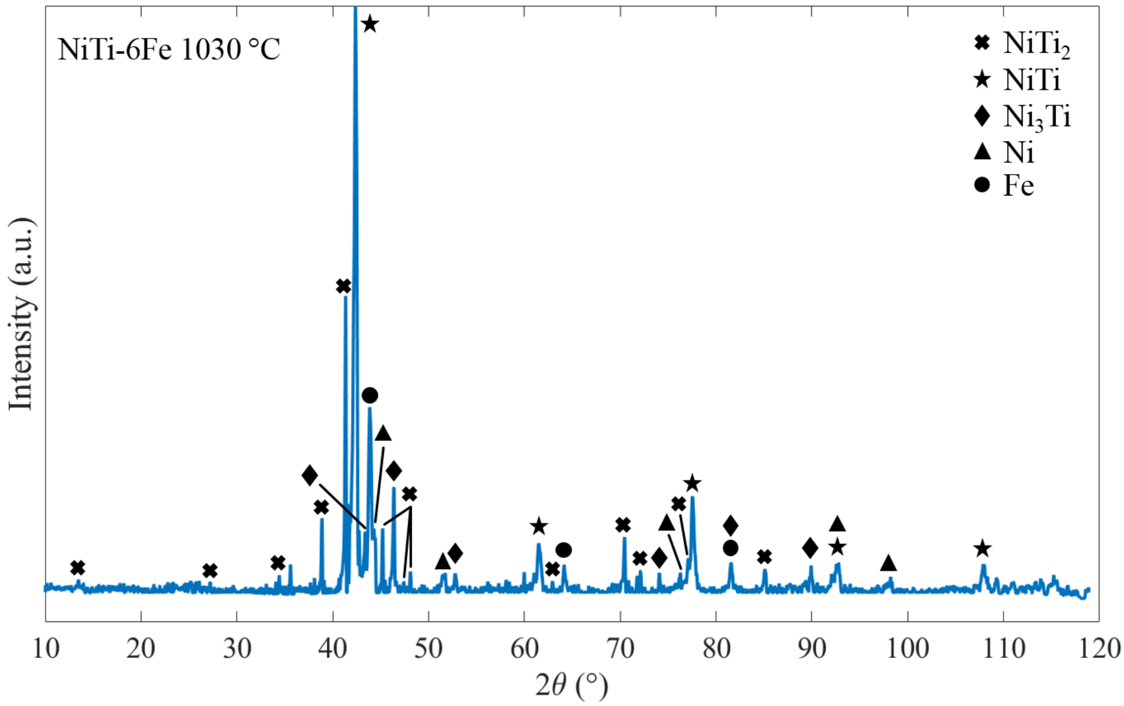

Appendix III - 5. XRD pattern for NiTi-6Fe, heated to 1030 °C.

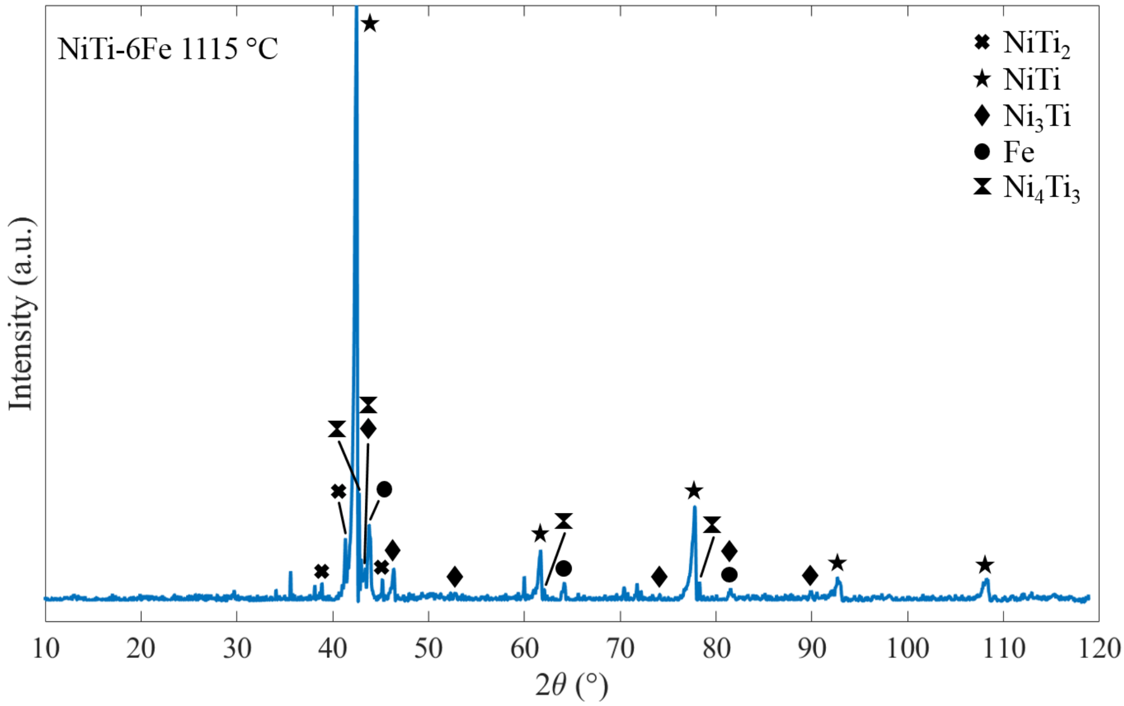

Appendix III - 6. XRD pattern for NiTi-6Fe, heated to 1115 °C.

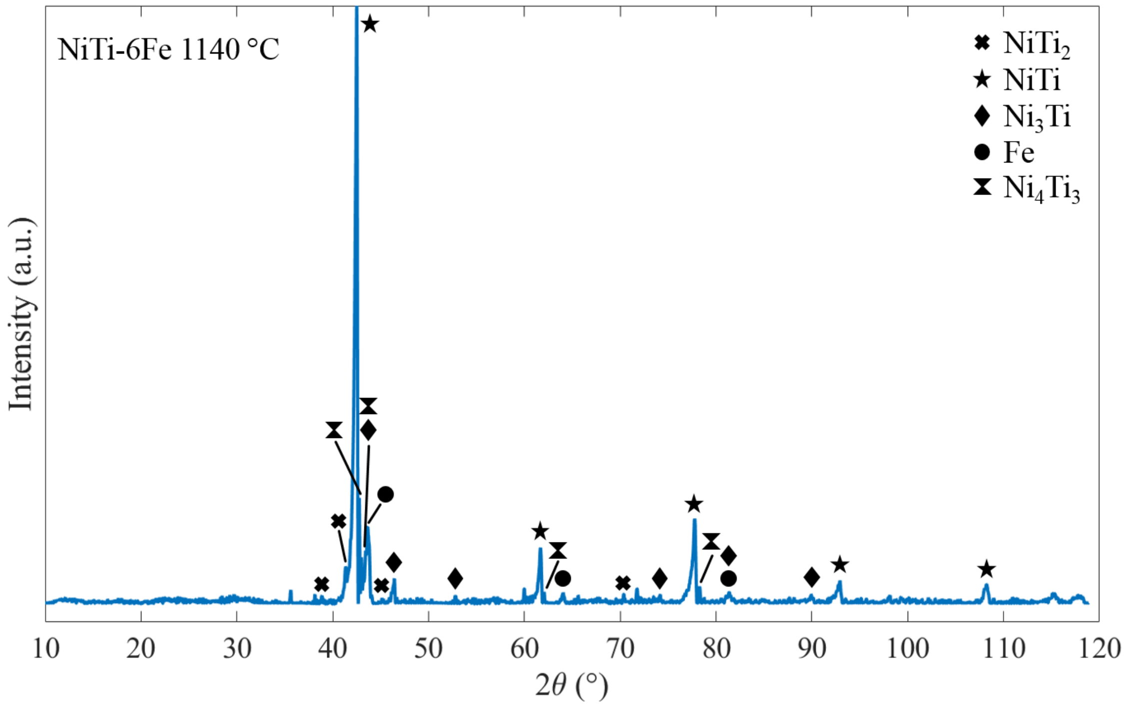

Appendix III - 7. XRD pattern for NiTi-6Fe, heated to 1140 °C.

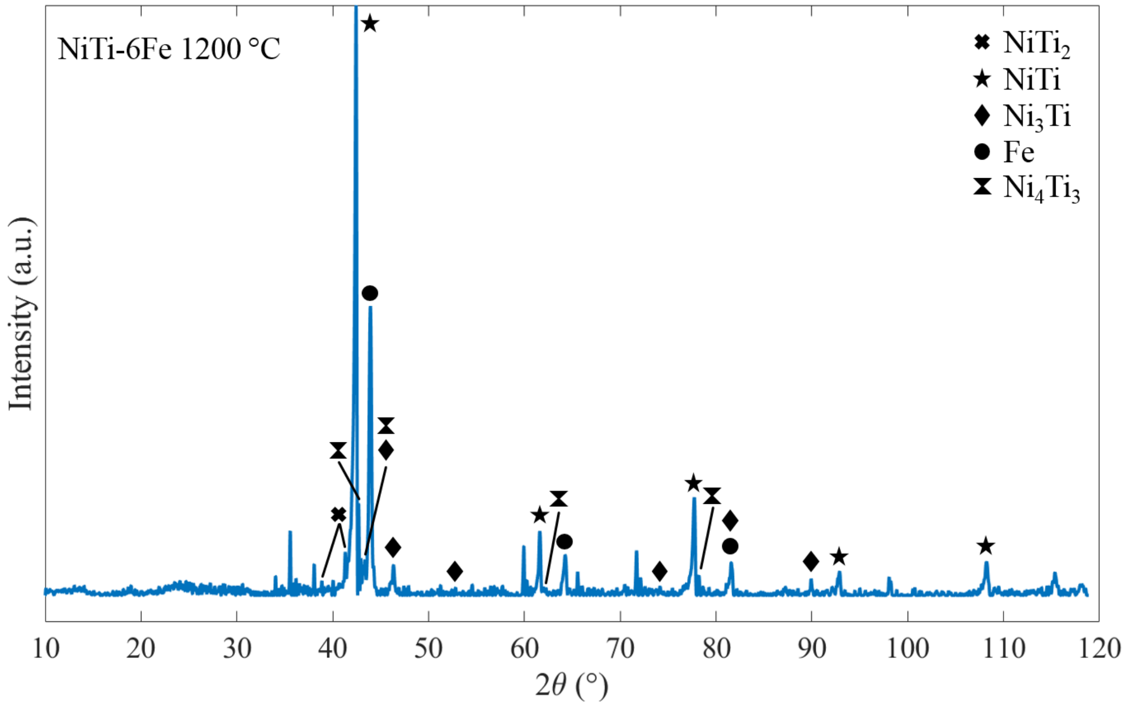

Appendix III - 8. XRD pattern for NiTi-6Fe, heated to 1200 °C.

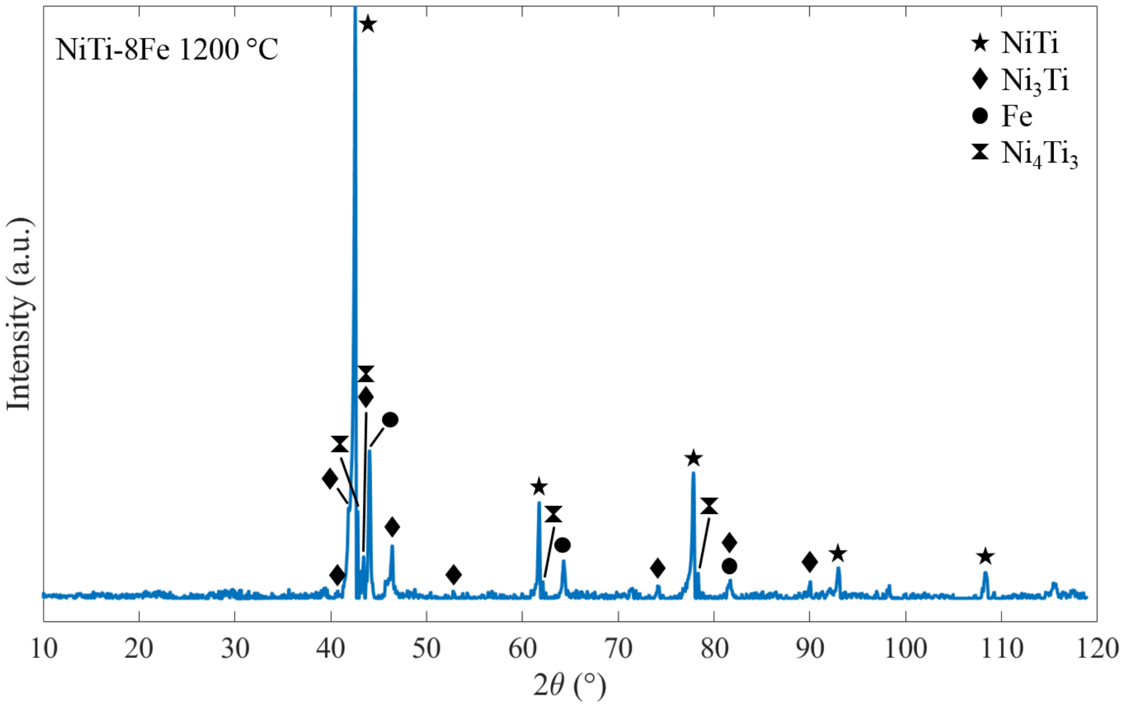

Appendix III - 9. XRD pattern for NiTi-8Fe, heated to 1200 °C.

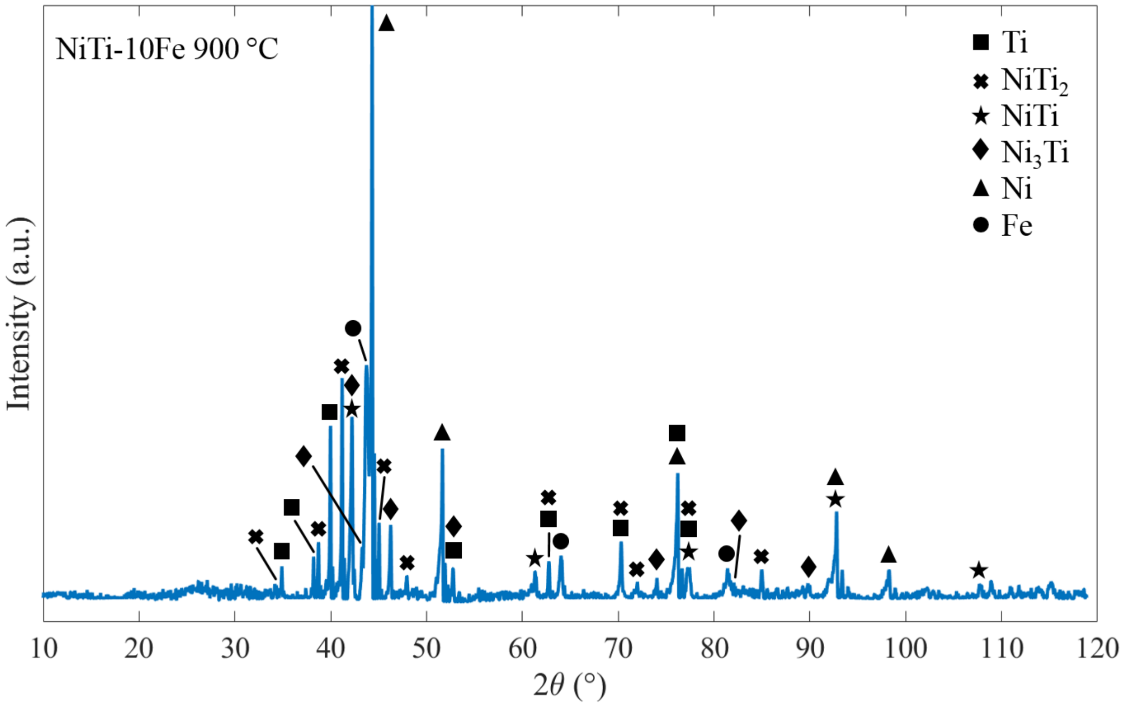

Appendix III - 10. XRD pattern for NiTi-10Fe, heated to 900 °C.

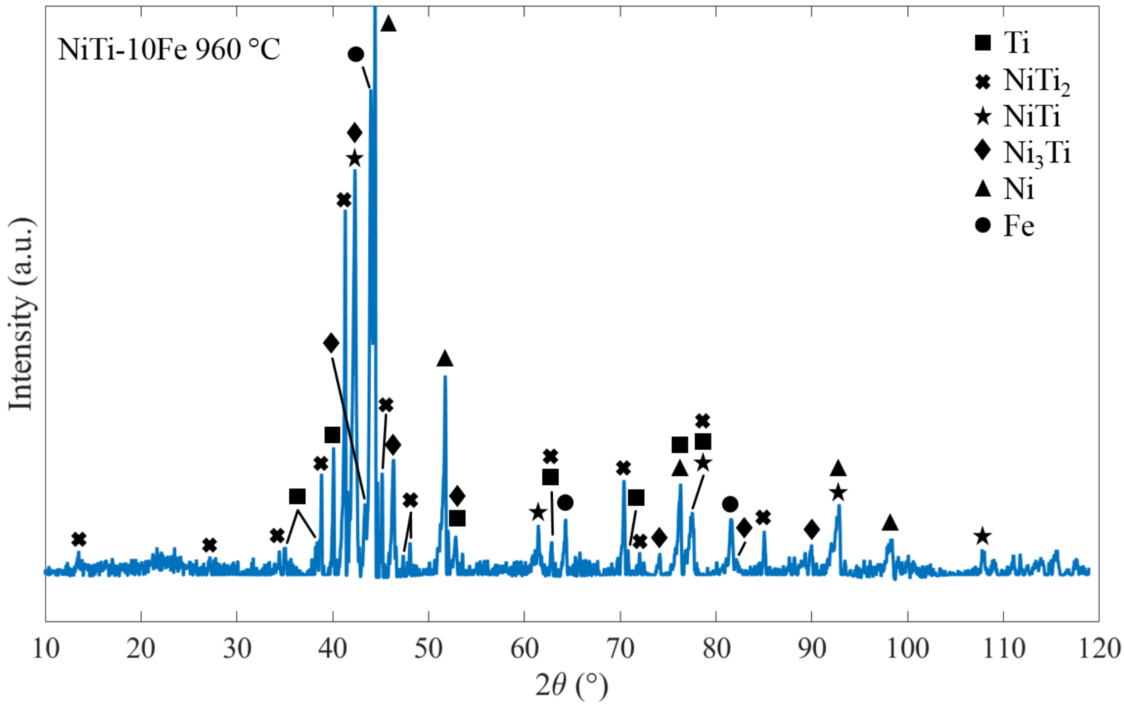

Appendix III - 11. XRD pattern for NiTi-10Fe, heated to 960 °C.

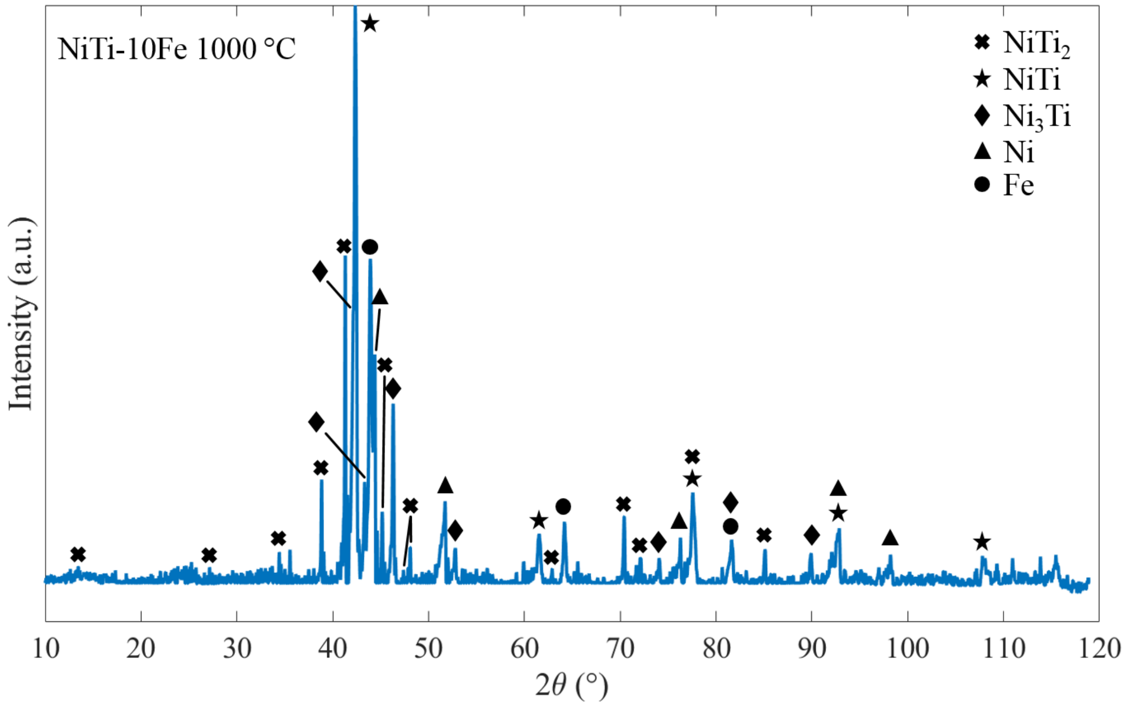

Appendix III - 12. XRD pattern for NiTi-10Fe, heated to 1000 °C.

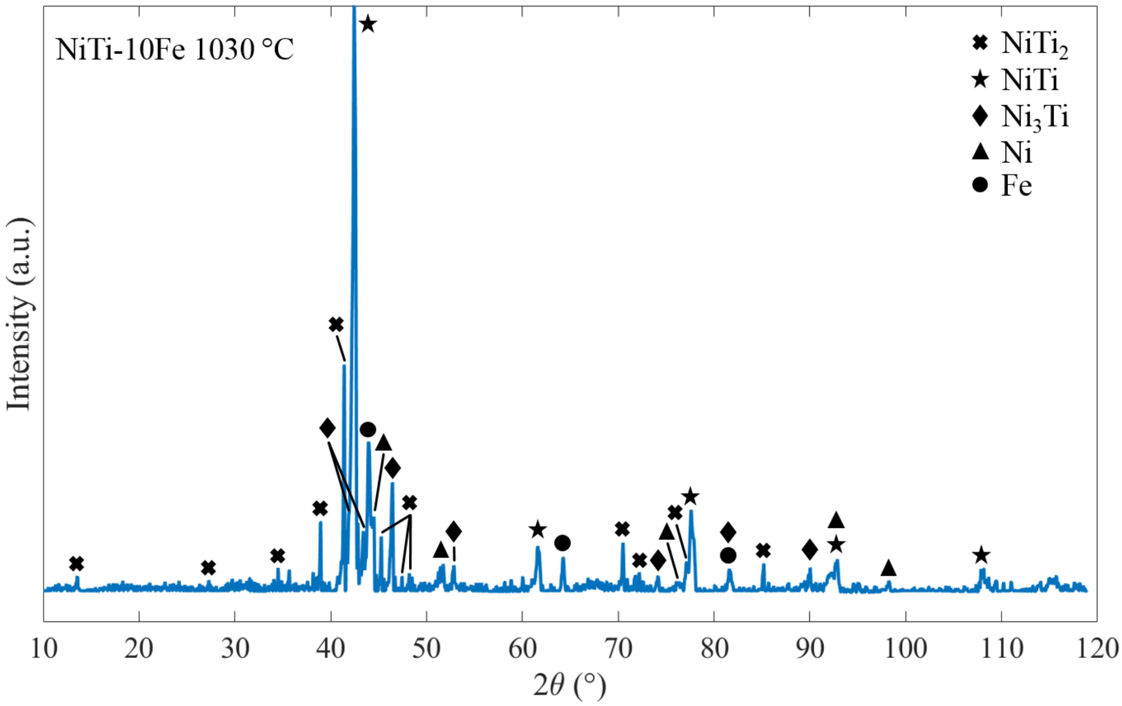

Appendix III - 13. XRD pattern for NiTi-10Fe, heated to 1030 °C.

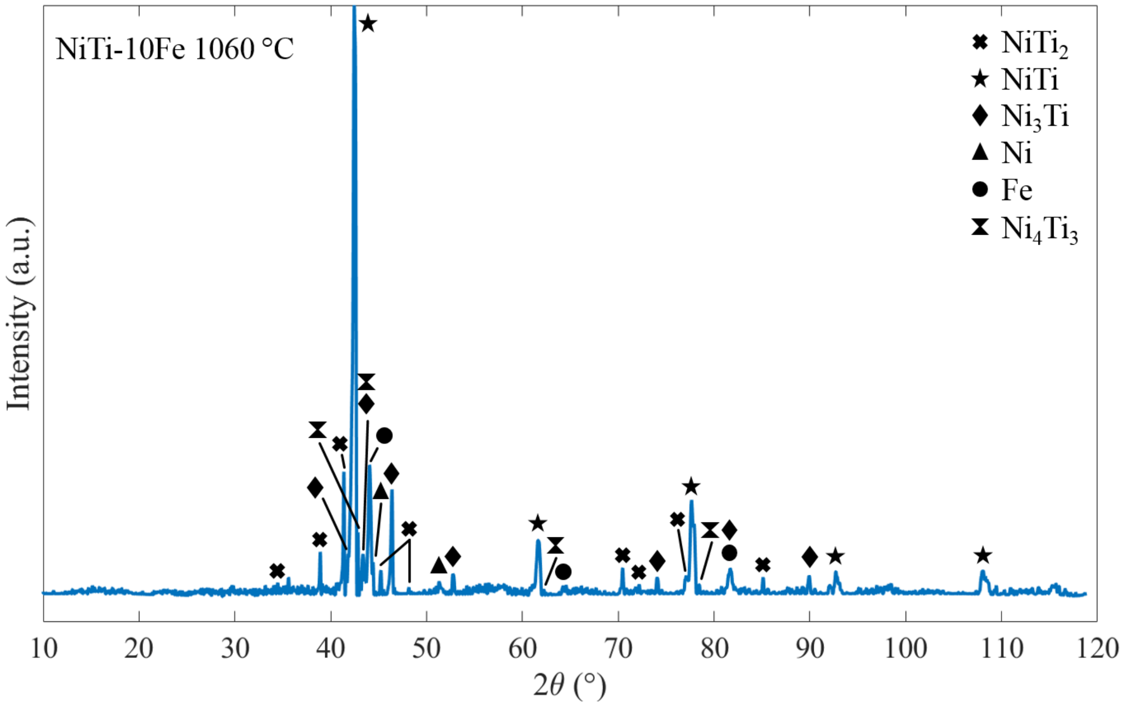

Appendix III - 14. XRD pattern for NiTi-10Fe, heated to 1060 °C.

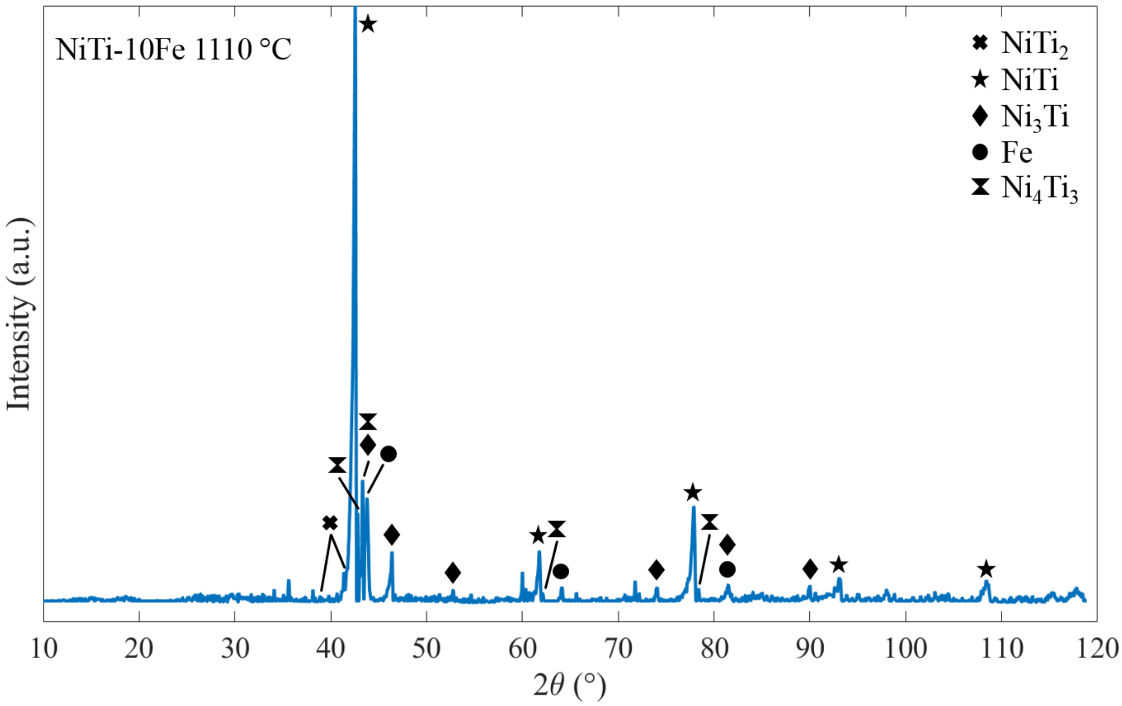

Appendix III - 15. XRD pattern for NiTi-10Fe, heated to 1110 °C.

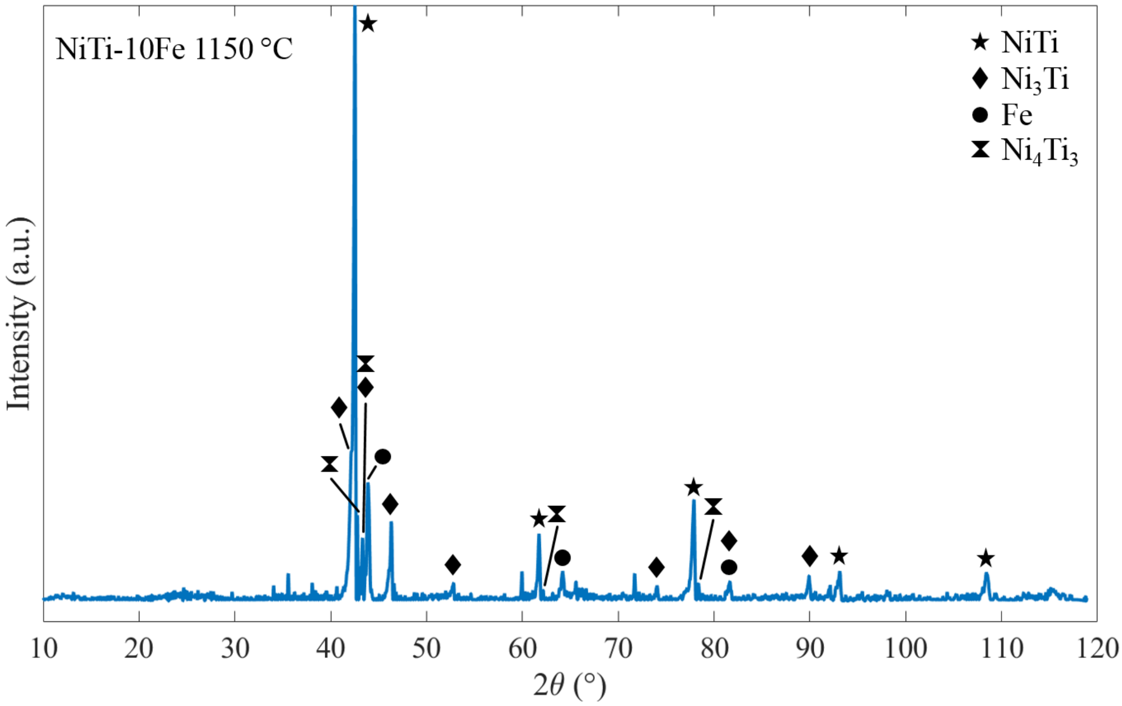

Appendix III - 16. XRD pattern for NiTi-10Fe, heated to 1150 °C.

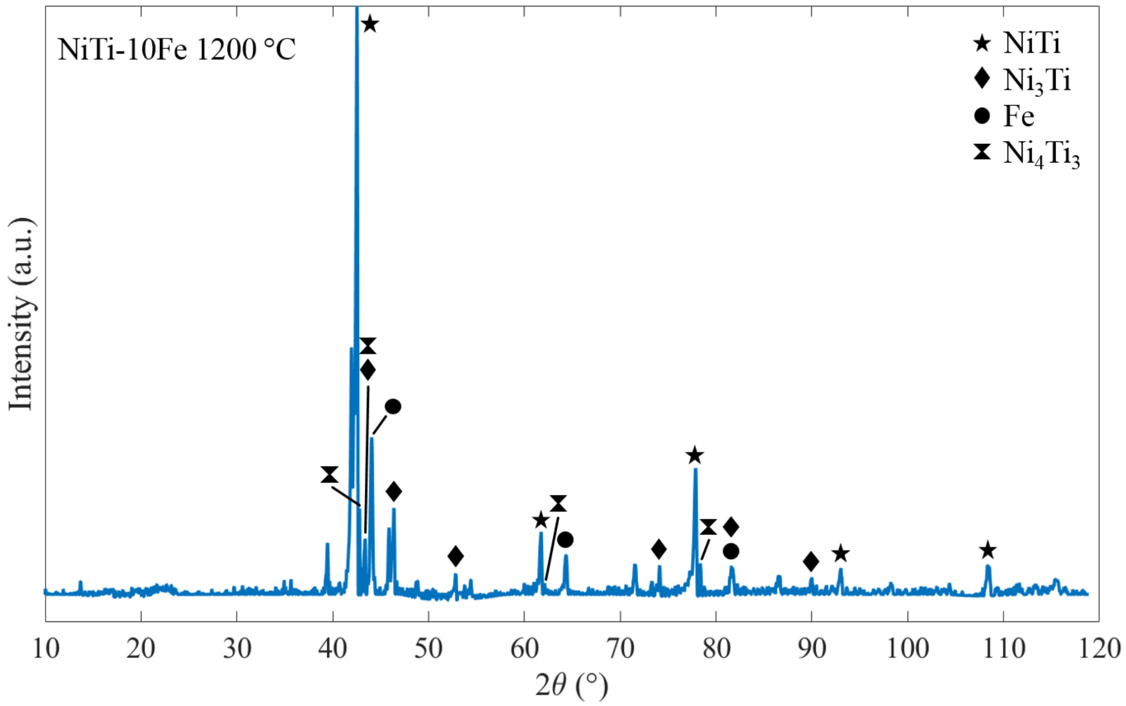

Appendix III - 17. XRD pattern for NiTi-10Fe, heated to 1200 °C.

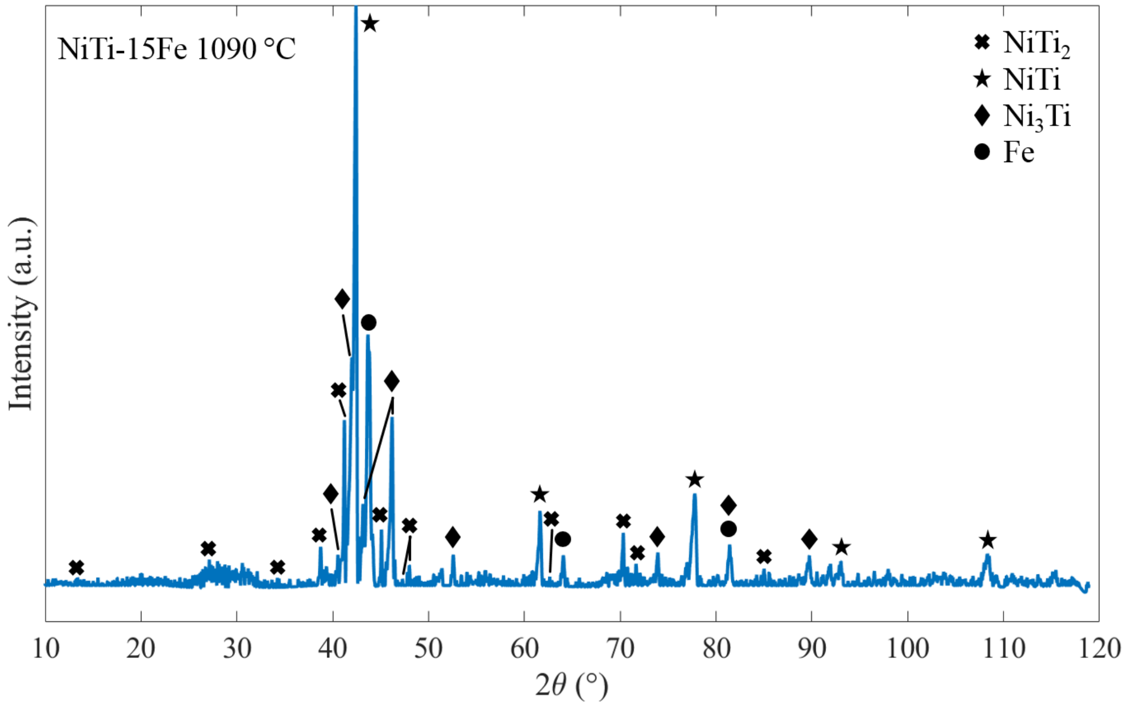

Appendix III - 18. XRD pattern for NiTi-15Fe, heated to 1090 °C.

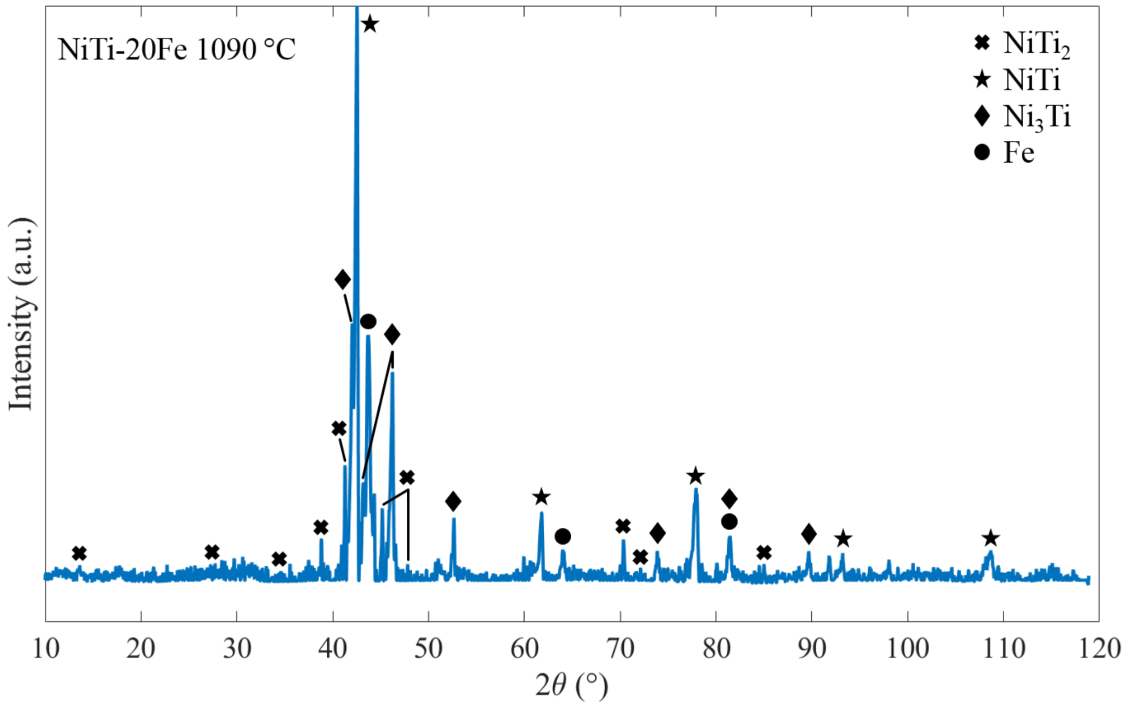

Appendix III - 19. XRD pattern for NiTi-20Fe, heated to 1090 °C.

Printed by Media-Tryck, Lund 2018 NORDIC SWAN ECOLABEL 3041 0903

Lund University
Department of Mechanical Engineering
Division of Materials Engineering

ISRN LUTFD2/TFMT--18/5058--SE